Advances in piezoelectric thin films for acoustic biosensors, acoustofluidics and lab-on-chip applications

Progress in Materials Science 89 (2017) 31–91

Contents lists available at ScienceDirect

Progress in Materials Science

journal homepage: www.elsevier.com/locate/pmatsci

Advances in piezoelectric thin films for acoustic biosensors, acoustofluidics and lab-on-chip applications

Y.Q. Fu [a,b,*], J.K. Luo [c,*], N.T. Nguyen [d,*], A.J. Walton [e], A.J. Flewitt [f], X.T Zu [a,*], Y. Li [b], G. McHale [b], A. Matthews [g], E. Iborra [h], H. Du [i], W.I. Milne [f,j]

[a] Institute of Fundamental and Frontier Sciences, University of Electronic Science and Technology of China, Chengdu 610054, China
[b] Faculty of Engineering and Environment, Northumbria University, Newcastle upon Tyne NE1 8ST, UK
[c] Institute of Renewable Energy and Environment Technology, University of Bolton, Deane Road, Bolton BL3 5AB, UK
[d] Queensland Micro- and Nanotechnology Centre, Griffith University, West Creek Road, Nathan, Queensland 4111, Australia
[e] Scottish Microelectronics Centre, Institute for Integrated Micro and Nano Systems, School of Engineering, University of Edinburgh, EH9 3FF Edinburgh, UK
[f] Electrical Division, Engineering Department, University of Cambridge, J.J. Thomson Avenue, CB3 0FA, UK
[g] School of Materials, The University of Manchester, Manchester M1 3BB, UK
[h] GMME-CEMDATIC, E.T.S.I. de Telecomunicación, Universidad Politécnica de Madrid, 28040 Madrid, Spain
[i] School of Mechanical and Aerospace Engineering, Nanyang Technological University, Nanyang Avenue, Singapore 639798, Singapore
[j] Quantum Nanoelectronic Research Centre, Tokyo Institute of Technology, O-Okayama, Tokyo, Japan[1]

Abbreviations: AC, alternating current; AE, acoustoelastic; AIDT, annular interdigitated transducer; ALD, atomic layer deposition; APM, acoustic-plate-mode; APTUDT, active passive track unidirectional transducer; ASAW, apodised surface acoustic wave; AW, acoustic wave; AZO, aluminium doped ZnO; BAW, bulk acoustic wave; BCC, body centred cubic; BDT, bi-directional transducer; BSA, bovine serum albumin; BST, $Ba_{0.8}Sr_{0.2}TiO_3$; CEA, carcinoembryonic antigen; C-FBAR, contour mode film bulk acoustic resonator; CMOS, complementary metal oxide semiconductor; CMR, contour mode resonator; CNT, carbon nanotubes; CVD, chemical vapour deposition; DART, distributed acoustic reflection transducers; DC, direct current; DDL, dispersive delay line; DFT, density functional theory; DRIE, deep reactive ion etch; DEP, dielectrophoresis; DIDT, dispersive interdigitated transducer; DLC, diamond like carbon; DNA, deoxyribonucleic acid; DNP, dinitrophenyyl aminohexanoic acid; DRIE, deep reactive ion etch; ECR, electron cyclotron resonance; EO, electro-osmotic; EP, electrophoresis; EWC-SPUDT, electrode width controlled single phase unidirectional transducer; EWOD, electro-wetting-on-dielectric; FBAR, film bulk acoustic resonator; FCC, face centred cubic; FCVA, filtered cathode vacuum arc; FEA, finite element analysis; FET, field effect transistor; FEUDT, floating electrode unidirectional transducer; FIB, focused ion beam; F-IDT, focused interdigitated transducer; FPW, flexural plate wave; FSAW, focused surface acoustic wave; GLAD, glancing angle deposition; HCP, hexagonal close packed; HiPIMS, high power impulse magnetron sputtering; HiTUS, high target utilisation sputtering; IC, integrated circuit; IDT, interdigitated transducer; Ig-E, immunoglobulin-E; Ig-G, immunoglobulin-G; IL, interleukin; IR, infrared; ITO, indium tin oxide; LBW, leaky bulk wave; LFE, lateral field excitation; LOC, lab-on-chip; LOD, limit of detection; LSAW, leaky surface acoustic wave; LSM, lanthanum strontium manganite; LWR, lamb wave resonators; MBE, molecular beam epitaxy; MEMS, microelectromechanical system; MOCVD, metalorganic chemical vapour deposition; MPECVD, microwave plasma enhanced vapour deposition; MSAW, magneto surface acoustic wave; MW, microwave; OAD, oblique angle deposition; ODS, octadecylesilane; ODT, octadecyle thiol; OTS, octadecyltrichlorosilane; PBAW, pseudo bulk acoustic wave; PCR, polymerase chain reaction; PDMS, polydimethylsiloxane; PECVD, plasma enhanced chemical vapour deposition; PET, polyethylene terephthalate; PI, polyimide; PLD, pulsed laser deposition; PMMA, poly(methyl methacrylate); PMUDT, proximity multi-track unidirectional transducer; PSA, prostate specific antigen; PSAW, pseudo surface acoustic wave; PTFE, polytetrafluoroethylene; PVD, physical vapour deposition; PVDF, polyvinylidene fluoride; PZT, lead zirconate titanate; QCM, quartz crystal microbalance; RAC, reflective array compressor; RF, radio frequency; RFID, radio frequency identification; SAM, self-assembled monolayer; SAW, surface acoustic wave; SBAW, shear bulk acoustic wave; SGAW, surface generated acoustic wave; SH-SAW, shear horizontal surface acoustic wave; SMR, solidly mounted resonator; SNR, signal-to-noise ratio; SPR, surface plasmon resonance; SPUDT, single phase unidirectional transducers; SSBW, surface skimming bulk wave; STW, surface transverse wave; TCD, temperature coefficient of delay; TCE, temperature coefficient of expansion; TCF, temperature coefficient of frequency; TCV, temperature coefficient of velocity; TEM, thickness extensional mode; TFBAR, thin film bulk acoustic resonator; TFE, thickness field excitation; TMAH, tetramethyl ammonium hydroxide; TSM, thickness shear mode; TSW, thickness shear wave; TTE, triple transit echo; UDT, unidirectional transducer; UV, ultraviolet; μTAS, micro-total analysis system; VOC, volatile organic compound; XRD, X-ray diffraction.

* Corresponding authors at: Faculty of Engineering and Environment, Ellison Building, Northumbria University, Newcastle upon Tyne NE1 8ST, UK (Y.Q. Fu).

E-mail addresses: Richard.fu@northumbria.ac.uk (Y.Q. Fu), J.Luo@bolton.ac.uk (J.K. Luo), nam-trung.nguyen@griffith.edu.au (N.T. Nguyen), xtzu@uestc.edu.cn (X.T Zu).

[1] Present address.

http://dx.doi.org/10.1016/j.pmatsci.2017.04.006

ARTICLE INFO

Article history:
Received 30 November 2015
Accepted 6 April 2017
Available online 24 April 2017

Keywords:
Piezoelectric
Thin film
Acoustic wave
Biosensor
Microfluidics
Acoustofluidics
Lab-on-chip
ZnO
AlN

ABSTRACT

Recently, piezoelectric thin films including zinc oxide (ZnO) and aluminium nitride (AlN) have found a broad range of lab-on-chip applications such as biosensing, particle/cell concentrating, sorting/patterning, pumping, mixing, nebulisation and jetting. Integrated acoustic wave sensing/microfluidic devices have been fabricated by depositing these piezoelectric films onto a number of substrates such as silicon, ceramics, diamond, quartz, glass, and more recently also polymer, metallic foils and bendable glass/silicon for making flexible devices. Such thin film acoustic wave devices have great potential for implementing integrated, disposable, or bendable/flexible lab-on-a-chip devices into various sensing and actuating applications. This paper discusses the recent development in engineering high performance piezoelectric thin films, and highlights the critical issues such as film deposition, MEMS processing techniques, control of deposition/processing parametres, film texture, doping, dispersion effects, film stress, multilayer design, electrode materials/designs and substrate selections. Finally, advances in using thin film devices for lab-on-chip applications are summarised and future development trends are identified.

Contents

1. Introduction . . . 33
1.1. Acoustic wave modes . . . 34
1.1.1. Bulk acoustic waves . . . 34
1.1.2. Lamb waves . . . 37
1.1.3. Surface acoustic waves . . . 37
1.2. Acoustic waves for sensing . . . 37
1.3. Acoustic waves for liquid actuation – acoustofluidics . . . 40
1.3.1. Wave-liquid interaction . . . 40
1.3.2. Digital acoustofluidics . . . 42
1.3.3. Continuous-flow acoustofluidics . . . 42
2. Bulk or thin film acoustic wave technologies? . . . 44
2.1. Why thin film acoustic waves? . . . 45
2.2. Why (and why not) ZnO? . . . 46
2.3. Why (and why not) AlN? . . . 47
2.4. Acoustic wave devices using ZnO and AlN films . . . 47
2.5. Multi-layer thin film acoustic wave structures . . . 47
3. Deposition and MEMS processing of ZnO and AlN films . . . 49
3.1. Thin film deposition techniques . . . 49
3.2. Film deposition parametres . . . 52
3.3. MEMS processing of ZnO and AlN films . . . 53
4. Engineering thin film technologies for acoustic wave applications . . . 53
4.1. Engineering film texture and wave modes . . . 53
4.1.1. Texture of films . . . 53
4.1.2. Film texture control and inclined angle growth . . . 55
4.2. Doping of ZnO and AlN films for device performance enhancement . . . 58
4.2.1. Doping of ZnO films . . . 58
4.2.2. Doping of AlN films . . . 59
4.3. Film thickness/dispersion effects . . . 59
4.3.1. SAW dispersive effects . . . 59
4.3.2. FBAR dispersive effects . . . 60
4.3.3. Lamb wave and Love wave dispersive effects . . . 61
4.4. Engineering film stress . . . 61
4.4.1. Film stress effect and its dominant factors . . . 61
4.4.2. Film stress measurement . . . 62
5. Engineering electrode materials and patterns . . . 62
5.1. Electrode materials . . . 63
5.2. Engineering electrode designs . . . 64
6. Recent development in thin film acoustic wave biosensors . . . 68
6.1. SAW biosensors . . . 68

6.1.1. SAW biosensors made of ZnO/Si and ZnO/glass . . . 68
6.1.2. SAW biosensors made of AlN/Si . . . 69
6.2. Lamb wave and flexible acoustic wave biosensors . . . 69
6.2.1. Lamb wave biosensors . . . 69
6.2.2. Flexible acoustic wave devices . . . 70
6.3. FBAR biosensors . . . 71
6.3.1. FBAR biosensor on silicon . . . 71
6.3.2. FBAR on flexible and arbitrary substrates . . . 72
6.4. Dual wave mode or multiple wave modes . . . 73
7. Thin film SAW based acoustofluidics . . . 73
7.1. Acoustofluidics with thin film SAW devices . . . 73
7.1.1. SAW streaming and particle concentration . . . 73
7.1.2. Liquid transport and mixing . . . 74
7.1.3. Liquid jetting . . . 74
7.1.4. Liquid nebulisation . . . 75
7.1.5. Particle and cell manipulation . . . 77
7.2. Lamb wave and flexible microfluidics . . . 77
7.3. Acoustic heating . . . 78
8. Summary and future trends . . . 79
8.1. Summary . . . 79
8.2. Future trends . . . 80
8.2.1. Integration . . . 80
8.2.2. Portable, wireless, flexible and remotely controlled devices . . . 81
8.2.3. Theoretical analysis and new theory? . . . 81
Acknowledgement . . . 81
References . . . 81

1. Introduction

Lab-on-a-chip (LOC) devices integrate several laboratory functions in a single chip to enable automation and high-throughput analysis. The key functions of a LOC system are [1,2]:

(i) Transportation of liquid samples containing bio-particles such as DNA, proteins and cells into an area with pre-deposited probe molecules.
(ii) Mixing and binding reactions of the extracted bio-particles with the probe, and remove non-specific and lossy binding.
(iii) Detection of an associated change in physical, chemical, mechanical, magnetic or electrical signals.

In the following, we first provide a brief introduction of acoustic waves as tools for sensing and actuation in LOC devices.

A typical LOC device consists of microfluidic components for sample preparations such as cell separation and concentration, filtering, cell lyses, and optical and electronic components for detection, control and signal processing [1,3]. Except for the electronics that can be borrowed directly from conventional technologies such as microelectronics and microelectromechanical systems (MEMS), all the other components are currently under extensive study and development.

Sample preparation is an important step for LOC-based analysis, and it includes multiple steps such as sample-intake, cell separation/sorting and cell lyses to extract DNA or proteins for subsequent detection. Before the sensing step, DNA has to be amplified through processes such as polymerase chain reaction (PCR). Various techniques have been developed for sample preparation. However, most of them are based on stand-alone devices, and the integration of all sample preparation steps into a single LOC is still a challenging task.

The key technology behind LOC devices is microfluidics, the science and technology of handling tiny volumes of liquids typically from a few picolitres (pL) to a few tens of microlitres (μL) in a single chip. Liquid samples are manipulated through processes such as pumping (or transportation), mixing, droplet generation, jetting and nebulisation (or atomisation) [4,5]. On the micro- and nanoscale, surface related phenomena such as capillary forces, surface tension, roughness and chemical interactions are dominant, making the fabrication of these systems complex and challenging. Typical microfluidic manipulation schemes are [6]: electro-osmosis (EO) [7], electrophoresis (EP) [8], dielectrophoresis (DEP) [9,10], electrowetting-on-dielectric (EWOD) [11,12], and electrostatic actuation [13]. Acoustofluidics is one of the sub-fields of microfluidics that utilises acoustic waves as the main tool, and has recently attracted significant attention from the research community owing to its simple implementation of multiple microfluidic functions such as micromixing, pumping, droplet generation and particle manipulations [14].

One of the major challenges in developing LOC devices is that sensing and actuating functions are realised through different mechanisms and are often fabricated using different processes and diverse materials. Acoustic waves have unique advantages for LOC devices because they can be used for both sensing and actuation. Acoustic wave sensors provide a high level of sensitivity. Acoustofluidics can handle liquid volumes from picolitres to a few tens of microlitres for mixing, pump-

ing, jetting and nebulisation. Acoustic waves can also be utilized for sample preparations such as cell sorting/separation, cell lyses, heating and PCR [15,16]. Therefore, major sample preparation tasks can be completed solely based on acoustic waves [17–20], significantly reducing the complexity of the system and operation cost.

Acoustic waves have been commercially exploited for more than 60 years in industrial applications ranging from communications to automotive and environmental sensing [21,20]. Applying an alternating current (AC) or radio frequency (RF) excitation to electrodes patterned on a piezoelectric material generates an acoustic wave that propagates in the direction perpendicular to the surface of the material into the bulk medium (bulk acoustic wave, BAW) or along the surface of the material (surface acoustic wave, SAW). Fig. 1 shows the different modes of BAWs and SAWs [22–30], such as thickness shear wave (TSW), leaky bulk waves (LBW), pseudo-bulk acoustic waves (PBAW), shear bulk acoustic waves (SBAW) often called surface skimming bulk wave (SSBW), Rayleigh SAWs (R-SAWs), shear-horizontal SAWs (SH-SAWs), Love mode waves, Lamb waves, and higher mode waves such as Sezawa or harmonic modes of the fundamental waves. A generic term of surface generated acoustic wave (SGAW) has also been proposed to include most of the acoustic waves generated and propagated on or near the device surface, including R-SAWs, SH-SAWs, Love mode SAWs, Lamb waves, flexural plate wave (FPW) and acoustic plate wave (APM) [31]. These SGAWs have been widely explored for sensing and acoustofluidic applications. Table 1 summarizes the working principles, advantages and shortcomings of the key acoustic wave types.

As this paper is focused on recent development of piezoelectric thin film technologies for acoustic-wave-based LOC applications, the following sections briefly introduce the fundamentals of different modes of acoustic waves and their applications for sensing and actuation.

1.1. Acoustic wave modes

1.1.1. Bulk acoustic waves

Quartz crystal microbalances (QCM) are the most-commonly used BAW devices, and are made of a bulk piezoelectric material, mostly using a quartz crystal, sandwiched between two metallic electrodes, typically gold. The wave mode in a QCM is a bulk thickness shear mode (TSM), which is suitable for both dry and liquid conditions. The QCM devices generally have a good temperature stability and low spurious bulk wave generation.

Shear BAWs (SBAWs) or more commonly called surface skimming bulk waves (SSBWs) are shear horizontal BAWs propagating just beneath the substrate surface such as in the rotated Y-cut quartz. Leaky surface acoustic wave or pseudo-surface acoustic waves (PSAWs) with high phase velocities of more than 10,000 m/s are fast leaky wave modes with a predominantly longitudinal wave that leaks energy into the substrate as the wave propagates. Although the LSAWs have a larger coupling coefficient and a better temperature stability or higher frequency than those of standard SAWs, they are less sensitive to the surface perturbations due to the wave propagation in the bulk and beneath the surface.

Film bulk acoustic resonators (FBARs). FBARs have recently been extensively studied for sensing applications, and have a structure similar to that of QCM devices but with the advantage of being several orders of magnitude smaller as detailed in Table 1 [38,39]. As the thickness of the piezoelectric thin film determines the wavelength of the bulk resonators, the operating frequency of the FBARs ranges from sub-GHz to tens of GHz. There are three types of FBAR structures: a back trench type, a Bragg acoustic mirror type, and an air-bag type as identified in Table 1.

The back-trench FBAR is the most common FBAR device, which has a thin film membrane formed by etching away the bulk substrate underneath. The air bag type of FBAR is similar to the back trench ones, where the large back trench is replaced by small gaps formed through a surface micromachining process which removes the supporting/sacrificial materials underneath the FBAR structure. This type of device has two typical structures produced by: (i) removing a thin film sacrificial layer above the substrate surface to form a trench; (ii) laterally removing the bulk material beneath the top structure layer to form a trench (see Table 1).

The Bragg acoustic mirror type FBARs are generally called solidly mounted resonators (SMRs), where the Bragg reflector or the acoustic mirror is composed of multiple quarter-wavelength layers with alternating low and high acoustic impe-

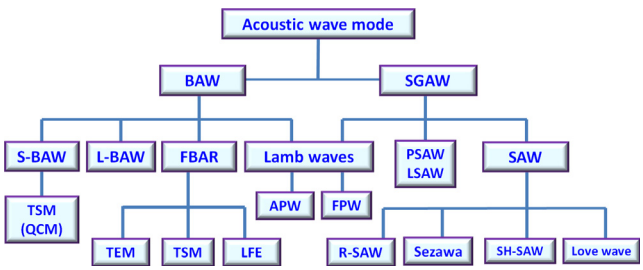

Fig. 1. Classification of different wave modes in two categories: bulk acoustic wave (BAW) and surface generated acoustic waves (SGAW). The key types of BAWs include: longitudinal BAW (L-BAW); shear BAW (S-BAW), thickness shear mode (TSM)-Quartz crystal microbalance (QCM), film bulk acoustic wave (FBAR); thickness extensional mode (TEM); lateral field excitation (LFE) mode; Lamb waves, acoustic plate wave (APW). The key types of SGAW include: Rayleigh SAW (R-SAW), Sezawa mode waves; shear-horizontal SAWs (SH-SAWs); Love mode wave; pseudo-surface acoustic waves (PSAW) or Leaky SAWs (LSAW), Lamb wave mode; flexural plate wave (FPW).

Table 1
Key parametres for different acoustic wave modes.

Wave mode	Illustration	Resonant frequency	Sensitivity	Advantages	Problems	Components
QCM (Thickness shear mode)	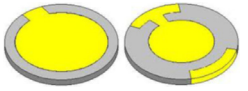	kHz to a few MHz $f_o = \frac{v}{2h_o}$ h_0, quartz crystal thickness; v, the sound velocity	Relative sensitivity to mass loading: $S_r = \frac{-2f_o}{\rho_p v} = -\frac{1}{\rho_p h_o}$ ρ_p, the piezoelectric material density. Sensitivity to liquid viscosity Δf [32]: $\Delta f = -f_o^{3/2}\sqrt{\frac{\eta_l \rho_l}{\pi \mu_c \rho_c}}$ μ_c and $\boldsymbol{\rho_c}$ are the stiffness and density of the crystal, and μ_l and ρ_l are the density and viscosity of the liquid	• Capable of detection in humid and liquid environment • Relatively easy to use • Equipment is inexpensive and cost is low • High Q factor • Mature technology	• Low detection resolution due to low operating frequency • A thick substrate (0.5–1 mm) and large surface area (>1 cm^2) which are difficult to scale down	• Quartz plates • Au electrodes
Rayleigh SAW (Rayleigh mode)	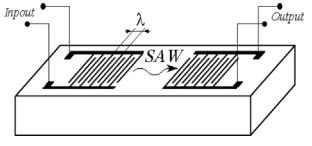	A few MHz-GHz $f_0 = \frac{v}{\lambda} = \frac{v}{4d}$ λ is the wavelength; d is the width of finger for IDT	Mass sensitivity [33] $\Delta f = k\frac{\Delta m f_o^2}{A}$ k is a constant of the sensing system; Δm is the mass loading; A is the area	• Low power consumption • Relatively low cost • Wireless control • Easy processing	• High attenuation in humid conditions • Significant wave damping in a liquid environment	• 41°YX cut $LiNbO_3$, • ST-cut Quartz, • 128° Y-cut LiNbO3 etc. • ZnO, AlN and PZT thin film devices.
Lamb waves	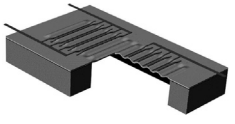	kHz to lower MHz (thin film based higher Lamb wave modes can be a few hundreds MHz to 1 GHz) Velocities of A_0 and S_0 modes are [34]: $V_{Ao} = \frac{2\pi h}{\lambda}\sqrt{\frac{E}{12(1-\nu^2)\rho}}\frac{1}{\sqrt{\frac{\pi^2 h^2}{3\lambda^2}+1}}$; $V_{so} = \sqrt{\frac{E}{(1-\nu^2)\rho}}$	Mass sensitivity of FPW devices [35] $S_m \propto 1/(2\rho d)$	• Can support two different propagation modes, one symmetric and one antisymmetric • Wireless control • Able to operate in liquid condition	• Radiation loss could occur in liquid • Fragile structure as the thickness of film is thin • Temperature sensitivity	• ZnO, AlN and PZT multilayer membranes
SH-SAW	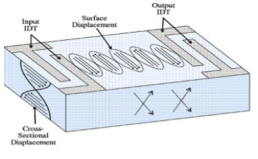	A few to hundreds of MHz $f_0 = \frac{v}{\lambda} = \frac{v}{4d}$ d is the width of IDT finger	Mass sensitivity $\Delta f = k\frac{\Delta m f_o^2}{A}$	• Low power consumption • Low cost • Wireless control • Able to operate in liquid environment	• Often not a pure shear wave when excited • Part of the energy is lost to a bulk acoustic wave • Depending on crystal orientations	• Quartz • 36° YX-cut $LiNbO_3$ • 64° YX-cut $LiNbO_3$

(*continued on next page*)

Table 1 (*continued*)

Wave mode	Illustration	Resonant frequency	Sensitivity	Advantages	Problems	Components
Love mode wave	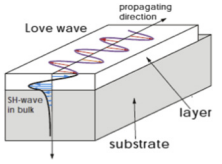	A few to hundreds of MHz $f_0 = \frac{v}{\lambda} = \frac{v}{4d}$ d is the width of finger		• Highest sensitivity among SAW sensors due to the wave guiding effect • Able to propagate in liquid environment	• With increasing thickness of film, insertion loss decreases quickly • Guiding layer effect is significant	• Substrates: 36° YX-cut $LiTaO_3$, Quartz, 64° YX-cut $LiNbO_3$ • Guiding layer: SiO_2, ZnO, TiO_2, PMMA, SU-8, Photoresist
Back trench FBAR	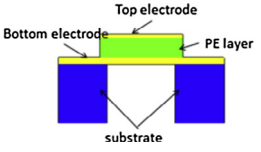	Sub- or a few GHz; $f_n = \frac{n(n+1)V}{2d}$ where n corresponds to different resonant modes. For multilayer FBAR $f_{(m_n Z_{sb}+1)} = \frac{m_n Z_{sb}+1}{2\left\{\frac{Z_{el1}l_{el1}}{v_{el1}}+\frac{Z_{sb}l_{sb}}{v_{sb}}+\frac{Z_{el2}l_{el2}}{v_{el2}}+\frac{l}{v}\right\}}$ Z acoustic impedance; l: thickness; sb: substrates	Mass sensitivity [36]: $\Delta f = \frac{-2h_f f_u^2}{\sqrt{\rho_c \mu_c}}\left(\Delta\rho_f - \frac{\Delta\mu_f}{v_s^2}\right)$ The subscript "μ" indicates the unperturbed field condition, the subscript "f" is related to the films, v_s is the velocity of the shear acoustic wave, and h_f is the height of the immobilized film	• Small dimensions • Small base mass • Very high sensitivity • Ability to fabricate using standard CMOS processing, materials and circuitry • Significantly reduced size and volume	• Large noise/signal ratio • Difficulty in signal control and measurement • Sensitive to many different parametres • Fragile membrane	• Si, Si_3N_4, or SiO_2 membrane • ZnO and AlN membrane etc.
Solidly mounted reflector (SMR)	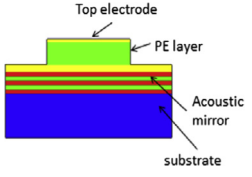	Sub- or a few GHz; $f_n = \frac{n(n+1)V}{2d}$	Mass sensitivity: $\Delta f = \frac{-2h_f f_u^2}{\sqrt{\rho_c \mu_c}}\left(\Delta\rho_f - \frac{\Delta\mu_f}{v_s^2}\right)$	• Small dimensions • Small base mass • More robust structure • Glass and plastic can be used • Very high sensitivity • Ability to fabricate using standard CMOS processing materials and circuitry • Significantly reduced size and volume	• Large noise/signal ratio • Difficulty in signal control and measurement • Sensitive to many different parametres • More film deposition processes, thus time consuming	• Pair of high impedance and low impedance layers as acoustic mirror • Reflectors: $LiNbO_3/SiO_2$, W/SiO_2, Ta_2O_3/SiO_2, and all metal reflectors of Mo/Ti and W/Ti, AlN/Mo, [37] Pt, W, TiN, AlN, HfO_2, Al/Ti, SiO_2/Ir. SiOC, Al, Au/Al
Air-bag FBAR	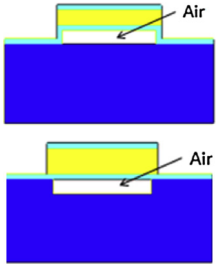	Sub- or a few GHz; $f_n = \frac{n(n+1)V}{2d}$	Mass sensitivity: $\Delta f = \frac{-2h_f f_u^2}{\sqrt{\rho_c \mu_c}}\left(\Delta\rho_f - \frac{\Delta\mu_f}{v_s^2}\right)$	• Small dimensions • Small base mass • Very high sensitivity • Ability to fabricate using standard CMOS processing, materials and circuitry • Significantly reduced size and volume	• Large noise/signal ratio • Difficulty in signal control and measurement • Sensitive to many different parametres • Sacrifical process is required	• ZnO and AlN membrane with a gap to substrate

dances. An excellent resonance with a limited acoustic damping into the substrate can be achieved because the acoustic energy is reflected and confined inside the top piezoelectric layer, due to the high acoustic impedance ratio of the acoustic mirror. The SMR design has a good mechanical robustness and a simpler fabrication process compared to the membrane-based structures. Hence, inexpensive substrates such as glass or plastics could be used for SMR fabrication. The disadvantage of the SMRs is that the multiple deposition processes for the acoustic mirrors need to be precisely controlled, and thus the fabrication of SMRs can be time-consuming and costly.

FBARs also have disadvantages including high fabrication cost, the requirement for complex read-out circuitry/electronics, increased noises, reduced Q factors, and the absence of good microfluidic functions.

1.1.2. Lamb waves

Lamb waves are generated when the substrate thickness is smaller than or comparable to the wavelength of the wave. They can either be (i) passive Lamb waves without the use of a piezoelectric substrate which are normally generated from a remote acoustic wave source; (ii) positive Lamb waves generated by a thin piezoelectric layer itself. This paper will focus only on the latter case.

Typically, Lamb waves propagating in thin plates or membranes have two modes at low frequencies [40]. The first ones are the zero-order antisymmetric mode, A_0, which are highly dispersive in the low frequency regime, often called flexural plate waves (FPWs) [41,42]. At higher frequencies, the wave velocity converges towards the Rayleigh wave velocity. With increasing layer thickness, the A_0 wave gradually changes into the Rayleigh wave or a higher order A-mode wave. The phase velocity of the A_0 mode is generally smaller in a liquid medium for microfluidic applications. Therefore, acoustic energy can be confined in the plate, rather than dissipating significantly into the liquid in contact. Thus this wave mode can be used for sensing in a liquid environment. In the liquid medium, the FPW mode or A_0 mode can also form a tightly coupled interface wave, called a Scholte mode wave [24,25,29]. Once the thickness of the FPW device increases or the acoustic wave power increases, the A_0 mode can radiate wave energy into the surrounding medium, causing acoustic streaming parallel to the device surface [43]. Therefore, the FPW modes have been proposed for mixing and pumping applications [44].

For the zero-order symmetrical Lamb wave mode or extensional mode, S_0, the thin plate expands in the direction of wave propagation and contracts in the thickness direction. When the layer thickness approaches zero, the S_0 mode becomes a longitudinal wave. At higher frequencies, the extensional mode converges towards the Rayleigh mode. The dissipation of the S_0 wave energy into the liquid is generally small, and thus the S_0 mode is often used for sensing in the liquid environment.

There are a number of higher Lamb wave modes which are significantly influenced by the substrate plate/membrane thickness (this will be discussed in details in Section 4.3). These modes converge to the shear-mode BAWs of the plate or membrane with increasing frequency or plate thickness.

1.1.3. Surface acoustic waves

Many SAW devices are based on the Rayleigh mode, which has both longitudinal and vertical shear components, resulting in an elliptical trajectory of surface particles and a rapid decay of particle oscillation with depth into the substrate. The higher modes of Rayleigh waves in the layered SAWs are generally called Sezawa modes. In principle, the Sezawa mode is a guided wave, in which the acoustic velocity of the top piezoelectric layer is lower than that of the substrate or sub-layer beneath. Thus, the wave can propagate through the interface or interlayers with a higher velocity than that of the top layer [45].

For sensing applications in liquid, the Rayleigh mode SAW device has a substantial surface-normal displacement and rapidly dissipates its energy into the liquid on the surface, leading to excessive damping. Therefore, Rayleigh mode based SAW devices are not well suited for sensing in liquid or humid conditions. Waves in a thickness shear horizontal SAW (SH-SAW) device or surface transverse wave (STW) device propagate along the surface, and do not significantly couple acoustic energy into the liquid [46,47]. These modes maintain a high sensitivity in liquids and are suitable for "real-time" sensing/detection in a liquid medium.

Love mode SAWs occur in a SH-SAW device, whose surface is covered with a thin wave-guide layer (such as SiO_2, ZnO or polymers), typically with microns or sub-micron thickness. The acoustic velocity of the wave-guide layer in a Love wave is much lower. Therefore, the acoustic waves generated are mostly trapped within this thin wave-guide leading to a high sensitivity [48]. The Love-mode devices are well suited for performing precision biosensing in liquid conditions [49–54]. Both SH-SAW and Love modes are mainly used for biosensing, but are rarely used for microfluidic applications due to their inefficiency [55,56].

1.2. Acoustic waves for sensing

Sensors are transducers that convert physical or chemical stimulations such as temperature, pressure or biochemical concentrations into electronic, optical, magnetic or acoustic signals for quantitative measurement and analysis. In particular, biosensors convert biological information into measurable signals (typically optical or electronic ones) with the assistance of biomarkers or biochemical reactions [57]. Most acoustic wave devices (especially QCM, SAW and FBAR) can be used as sensors because they are sensitive to mechanical, chemical, optical or electrical perturbations on their surfaces [58–60]. Acoustic wave sensors are reliable, sensitive and versatile, and able to monitor not only mass/density changes, but also changes in elastic modulus, viscosity, dielectric and conductivity properties [61,62], wirelessly and in real-time. Therefore, acoustic waves have been used for sensing temperature, moisture, strain, pressure, shock, acceleration, flow, viscosity, ionic

contaminants, pH levels, electric, magnetic and radiation fields, gas and explosives [63]. These sensors can be used to detect tiny traces of biomolecules through affinity binding with biomarkers for the detection of pathogens, viruses and early stage diagnosis of diseases such as cancers [64,65]. Compared to other common biosensing technologies, such as optical fibres, surface Plasmon resonance (SPR), and sensors based on field effect transistors or micro-cantilevers, acoustic wave based bio-sensing technologies have the combined advantages of high sensitivity, small size and low cost, simple operation without the need of bulky optical detection systems [66].

The fundamental biosensing technique using acoustic waves is the measurement of changes in the propagation velocity of the waves through the changes in the resonant frequency, phase angle or occasionally amplitude of reflection or transmission signals. Variations in phase velocity of the acoustic wave can be attributed to:

(i) Intrinsic factors such as material properties: density, elasticity, phase transformation, viscosity, conductivity, permittivity, changes in carrier concentration and mobility.
(ii) Extrinsic factors such as mass loading, temperature, deformation, pressure, strain, stress, humidity, pH values, ultraviolet (UV) and infra-red (IR) sources, externally applied electric/magnetic fields and charge injection.

Acoustic phase velocity, v, is related to the resonant frequency by $f_r = v/\lambda$, where λ is the wavelength. A change in acoustic velocity leads to a change in resonant frequency. The following relationship identifies the different sources that may contribute to the change of acoustic phase velocity, Δv:

$$\frac{\Delta f}{f_o} = \frac{\Delta v}{v_{\text{acoustic}}} = \frac{1}{v}\left(\frac{\partial v}{\partial m}\Delta m + \frac{\partial v}{\partial \sigma}\Delta\sigma + \frac{\partial v}{\partial c}\Delta c + \frac{\partial v}{\partial \varepsilon}\Delta\varepsilon + \frac{\partial v}{\partial T}\Delta T + \frac{\partial v}{\partial P}\Delta P + \frac{\partial v}{\partial}\Delta\eta + \frac{\partial v}{\partial \rho}\Delta\rho\cdots\right) \tag{1}$$

The above equation assumes that any external perturbations listed below are small; Δm is the change in mass load, $\Delta\sigma$ the change in conductivity, Δc the change in mechanical constant, $\Delta\varepsilon$ the change in dielectric constant, ΔT the change in temperature, ΔP the change in pressure, $\Delta\eta$ the change in viscosity and $\Delta\rho$ the change in density. Calculation methods for the resonant frequencies of a few key acoustic wave devices are summarised in Table 1.

The critical parametres of an acoustic wave sensor are sensitivity, response time, stability, reproducibility, reversibility, reusability, dynamic testing range, sensing limit, reliability and flexibility, as well as cost and environmental issues such as temperature and humidity.

The **sensitivity** of an acoustic wave sensor, S_r, to any external perturbation x is defined as:

$$S_r = \lim_{\Delta x \to 0}\frac{\Delta f}{f\Delta x} = \frac{df}{fdx} \tag{2}$$

where Δf is the frequency shift induced by Δx or the variation or perturbation of factors such as temperature, pressure, mass, density, viscosity or conductivity. When a piezoelectric material is used as a gravimetric or mass sensor, the frequency change can be expressed as [67]:

$$\Delta f = \frac{2\Delta m f_r^2}{A\sqrt{\rho\mu}} \tag{3}$$

where μ is the mass/area ratio, ρ is the density of the materials, and A is the surface area. Most acoustic wave devices show a mass sensitivity proportional to mass per unit area and square of the operating frequency [68,69] as listed in Table 1. Eq. (3) indicates that increasing the resonant frequency and reducing the base mass and surface areas of the device will increase the sensitivity of acoustic wave gravimetric sensors. The QCM as a gravimetric sensor has a limited sensitivity due to the thickness of the substrate, its large footprint, and the low frequency of operation. In contrast, SAW and FBARs have been developed for sensing as they exhibit a better sensitivity due to the higher operating frequency and the much reduced base mass. Fig. 2 schematically illustrates the performance in sensitivity of the different resonators versus their normal operational frequency ranges [70,71].

The electromechanical coupling coefficient (k^2) is a function of the piezoelectric coefficient of an acoustic wave device and is given by:

$$k^2 = \frac{e_{31}^2}{c_{11}\varepsilon_{33}} \tag{4}$$

where e_{31}^2 is electric field, C_{11} is the elastic constant of the material, and ε_{33} is the permittivity at a constant strain. Theoretically, k^2 is determined by:

$$k^2 = 2\frac{v_{free} - v_{metal}}{v_{free}} \tag{5}$$

where v_{free} and v_{metal} are the free surface and metalised (or short-circuited) surface phase velocities. The value of k^2 depends on the piezoelectric material, wavelength, substrate, the guiding layer materials and their thickness. The value of k^2 can also be determined by:

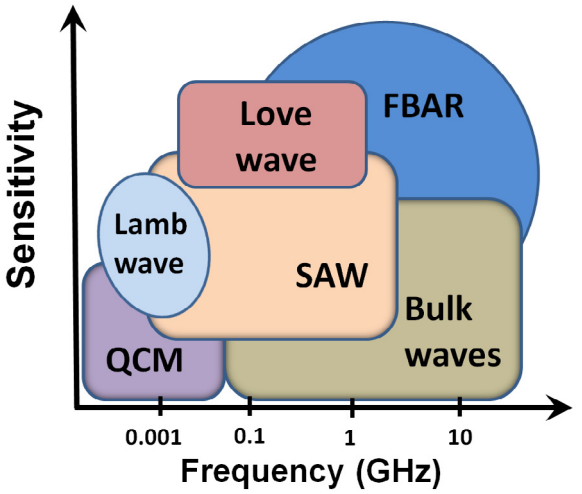

Fig. 2. Comparison of frequency range and sensitivity of common acoustic wave devices. The QCM has a limited sensitivity due to the thickness of the substrate, its large footprint, and the low frequency of operation; Lamb waves have improved sensitivity due to their increased frequency and surface related vibrations; SAWs have a better sensitivity due to the higher operating frequency and the much reduced base mass. Love mode SAWs show better sensitivity due to wave-guiding effects. FBARs show the highest sensitivity due to higher frequency and reduced mass.

$$k^2 = \frac{\pi}{2}\frac{f_s}{f_p}\left[\tan\left(\frac{\pi}{2}\frac{f_s}{f_p}\right)\right]^{-1} \tag{6}$$

where f_s and f_p are the series and parallel resonance frequencies (i.e., polarization is either in phase with the applied electric potential; or 180° out of phase with the applied potential, respectively).

Experimentally, k^2 of a SAW device can be determined by:

$$k^2 = \frac{\pi}{4N}\left(\frac{G}{B}\right)_{f=f_o} \tag{7}$$

where N is the number of SAW device finger pairs; G is the conductance (real part) and B is the susceptance (imaginary part) of the electrical admittance $Y = G + jB$, at the central frequency, respectively. The values of G and B can be obtained from the Smith Charts of the reflection/transmission coefficients at the central resonant frequency of the acoustic wave signals from a network analyser.

If the effects of electrodes and loss in the piezoelectric thin film are considered, the effective electromechanical coupling coefficient of the acoustic device, k_{eff}^2, is introduced to include material properties and the structure and the geometry of the resonator. For the FBAR device, the expression for the k_{eff}^2 is given by [72]:

$$k_{eff}^2 = \frac{\pi^2}{4}\left(\frac{f_p - f_s}{f_p}\right);\ \text{or}\ k_{eff}^2 = \frac{f_p^2 - f_s^2}{f_p^2} \tag{8}$$

where f_s and f_p are the series and parallel resonance frequencies as defined above.

The quality factor *Q* is frequently used to describe the performance of acoustic wave resonators, especially for the QCM and FBARs. The quality factor is influenced by dielectric losses of the piezoelectric materials/films, ohmic losses in contacts and electrodes, finite lateral size of the resonator (which might generate lateral modes), acoustic leakage to the substrate, surface and interface roughness, and internal friction in the piezoelectric thin film materials at defects and grain boundaries, columnar structures, cracks and voids.

Theoretically, the Q factor of an acoustic wave device is defined as:

$$Q = \frac{f}{2G}\frac{\partial B}{\partial f} \tag{9}$$

The Q factor can be obtained using the S parameter measurement [73]:

$$Q = \frac{f_s/f_p}{1-(f_s/f_p)^2}\sqrt{\frac{(1-|S_{12max}|)}{|S_{12max}|}\frac{(1-|S_{11min}|)}{|S_{11min}|}} \tag{10}$$

here S_{11} is the reflection signal, and S_{12} is transmission signal of the device.

Experimentally, the Q factor is often determined using the well-known −3 dB method where

$$Q = f_o/\Delta f_{-3\mathrm{dB}} \tag{11}$$

and $\Delta f_{-3\mathrm{dB}}$ is the bandwidth at −3 dB of the resonant peak of the admittance at f_o.

The signal-to-noise ratio (SNR) is a measure of the ratio between wave outputs required from acoustic waves and other background reflections or unwanted signals (*i.e.*, "noise"). The SNR depends on a number of elements: resonant frequency, bandwidth, efficiency, interface properties such as surface curvature and roughness, as well as the inherent defects of the device microstructure.

Temperature effects are critical in acoustic wave based sensing. Temperature dependency is caused by various parametres such as temperature coefficient of frequency (*TCF*), temperature coefficient of delay (*TCD*), temperature coefficient of velocity (*TCV*), which are related to the temperature coefficient of expansion (*TCE*, α) of device materials. These relationships can be expressed as:

$$TCF = -TCD = \frac{1}{f_o}\frac{df}{dT} = \frac{1}{v}\frac{dv}{dT} - \frac{1}{L}\frac{dL}{dT} = \frac{1}{v}\frac{dv}{dT} - \alpha \tag{12}$$

Values of the *TCFs* are determined by substrate materials, top layer material and wavelength of the device. Values of the *TCDs* can be determined using:

$$TCD = \frac{1}{\tau_o}\frac{\tau - \tau_o}{T - T_o} \tag{13}$$

where τ and τ_0 are time delays at temperatures of T and T_o. The *TCF* values are normally measured experimentally by recording changes of the frequency values as a function of temperature.

1.3. Acoustic waves for liquid actuation – acoustofluidics

Acoustofluidics is the research and application area at the interface of acoustics and microfluidics. As explained in the previous section, acoustics is traditionally used in sensing applications, but recent research work extends the application area of acoustics to fluidic actuation. Mixing, pumping, jetting and nebulisation are the enabling processes of microscale acoustofluidics for applications such as biochemical analysis, disease diagnosis, DNA sequencing and drug delivery. Mixing and pumping are challenging for microfluidics and nanofluidics due to the inherent low Reynolds number in small scales, the dimensionless ratio of inertial and friction forces [74,75]. The small device size prevents flow velocities reaching a high Reynolds number. Acoustic waves can overcome this limitation by inducing additional energy through high-frequency and higher-order nonlinear phenomena. Acoustic streaming is a non-linear effect of the absorption of high frequency and high-amplitude acoustic oscillations in a fluid, and can be used for pumping and mixing in both continuous-flow and digital microfluidics [76,77]. Acoustic streaming also facilitates internal mixing and accelerates hybridization reactions in protein and DNA analysis, minimizes non-specific affinity binding, speeds up biochemical reactions, and provides PCR functions [78–81].

1.3.1. Wave-liquid interaction

Acoustic waves utilized in microfluidics are mainly Rayleigh waves, bulk acoustic waves, and occasionally Lamb waves. Here we will focus on Rayleigh waves as an example. Driven by a body force, F_j, induced by acoustic waves, the fundamental hydrodynamics of a steady viscous fluid is governed by the Navier-Stokes equation [41,82]:

$$(v_i \cdot \nabla) v_j = F_j - \frac{1}{\rho}\nabla p + \eta \nabla^2 v_j \tag{14}$$

where v is the acoustic streaming velocity (or the particle velocity), p the pressure, ρ and η are the fluid density and shear viscosity coefficient, respectively. The subscripts i and j = 1, 2, 3 represent the x, y and z coordinates, respectively. The nonlinear body force is correlated to the Reynolds' stress induced by the acoustic wave in the fluid with spatial variations in all three coordinates. The acoustic wave induces a surface displacement normal to or within the surface in the range of a few angstroms to a few nanometres, depending on the applied powers and the frequency of the waves. When acoustic energy and momentum are coupled into the fluid, a net pressure, p, forms in the direction of propagation of the acoustic wave and efficiently drives the liquid [83]:

$$p = \rho_0 v_s^2 \left(\frac{\Delta\rho}{\rho_0}\right)^2 \tag{15}$$

where ρ_0 is the density of the liquid and v_s is the wave propagation velocity. This acoustically induced pressure causes the steady acoustic streaming that can be used for mixing and pumping.

SAW-based pumps and mixers have recently been extensively investigated for microfluidic applications [84–88]. The SAWs generated from the interdigitated transducer (IDT) electrodes travel along the surface of the piezoelectric substrate with sub-nanometre surface displacements. The SAW changes its vibration mode into a leaky SAW once it interacts with the liquid, and this leaky longitudinal SAW continuously travels in the liquid based on a streaming angle determined by the Rayleigh angle θ_R [89,90], as shown in Fig. 3a:

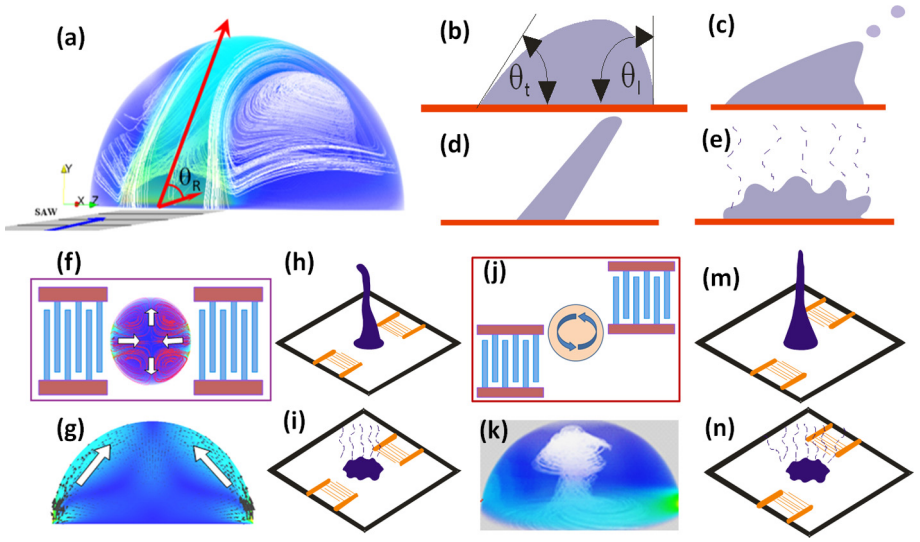

Fig. 3. Digital acoustofluidics: (a) Leaky longitudinal SAW continuously travels within the liquid medium; left: the streaming angle determined by the Rayleigh angle θ_R; (b) exciting a liquid droplet with acoustic waves deforms the original shape following the Rayleigh angle, resulting in the different contacting angles at trailing and leading edged of the droplet; (c) acoustic streaming in a droplet with a single IDT from the left causes the ejection of small droplets on a hydrophilic surface; (d) by increasing the SAW power, jetting on a hydrophobic surface can be obtained; (e) nebulisation on a hydrophilic surface at a higher RF power level; (f and g) acoustic streaming in a droplet with two opposite IDTs from both sides, resulting in quadruple streaming patterns, and droplets being pushed up from two sides; (h) jetting on a hydrophobic surface and (i) nebulisation on a hydrophilic surface at higher powers induced by two opposite IDTs; (j and k) acoustic streaming in a droplet with offset IDTs from both sides; resulting in twisting and concentration effects; (m) jetting on a hydrophobic surface; and (n) nebulisation on a hydrophilic surface induced by offset IDTs from both sides.

$$\theta_R = \sin^{-1}\frac{v_L}{v_S} \tag{16}$$

where v_S is the Rayleigh SAW velocity on the piezoelectric substrate and v_L is the acoustic velocity in the liquid. SAW-induced acoustic streaming patterns in the liquid can be changed significantly according to the size, shape and position of the confined liquid (e.g. droplet or liquid in a microchannel), the wave incident position, and the operating frequency of the SAWs. The induced streaming in the liquid droplet is governed by the incompressible Navier-Stokes equation (14). The displacements (Δx, Δy) in the x and y directions are generally expressed as [91];

$$\Delta x = A\exp(j\omega t)\exp(-jk_L x)\exp(-\vartheta k_L y) \tag{17}$$

$$\Delta y = -j\vartheta A\exp(j\omega t)\exp(-jk_L x)\exp(-\vartheta k_L y) \tag{18}$$

where $k_r = 2\pi/\lambda$ is a real number; the leaky SAW wave number ($k_L = k_r + jk_i$) is a complex number with the imaginary part; jk_L represents the SAW energy dissipation within the liquid fluid. The symbol of ϑ represents the attenuation constant;

$$\vartheta = 1 - \left(\frac{v_L}{v_S}\right)^2, \tag{19}$$

where v_S and v_L are the SAW velocity and the wave velocity in the liquid, respectively. If the wave displacements (Δx, Δy) are replaced by the wave velocities, the two components of streaming force can be obtained for an incompressible fluid as follows [68,82];

$$F_x = -(1+\vartheta_1^2)A^2\omega^2 k_i \exp 2(k_i x + \vartheta_1 k_i y) \tag{20}$$

$$F_y = -(1+\vartheta_1^2)A^2\omega^2\vartheta_1 k_i \exp 2(k_i x + \vartheta_1 k_i y) \tag{21}$$

where $\vartheta = j\vartheta_1$. The total SAW streaming force F can be calculated using $F = \sqrt{F_x^2 + F_y^2}$, which is given by;

$$F = -(1+\vartheta_1^2)^{\frac{2}{3}}A^2\omega^2 k_i \exp 2(k_i x + \vartheta_1 k_i y) \tag{22}$$

The SAW force F acts on the liquid as a body force. The exponential decay of the leaky SAW limits the influence of this force in the fluid volume, and leads to a completely diminished acoustic force within tens or a few hundreds of microns from the interface between the SAW and the liquid. Corresponding to the two basic microfluidic platforms, the use of acoustic actuation in microfluidics leads to two major areas of acoustofluidics: the digital one (dealing with sessile droplets) and the continuous-flow one (dealing with liquid in a microchannel).

1.3.2. Digital acoustofluidics

Generally, the attenuation length, L_{SAW}, of the SAW into a liquid can be estimated from [92,93]:

$$L_{SAW} = \frac{1}{\alpha_L} = \frac{\rho v}{\rho_f v_f} = \frac{\rho v^2}{\rho_f v_f f} \tag{23}$$

where ρ_f and ρ are the densities of the liquid and substrate material, respectively, v_f is the velocity of longitudinal wave in the fluid, v is the SAW velocity in the substrate, and α_L is the attenuation coefficient per unit length scale of the Rayleigh wave. From Eq. (23), L_{SAW} is inversely proportional to the resonant frequency, or α_L is proportional to the frequency, indicating that the attenuation increases with SAW frequency.

In the case of acoustic streaming inside a sessile droplet, the dimensionless ratio of droplet radius R_d to the SAW attenuation length L_{SAW}, *i.e.*, R_d/L_{SAW}, can be used to describe the efficiency of the streaming. A mean value of $R_d/L_{SAW} \approx 1$ implies fast and efficient mixing. For a ratio of R_d/L_{SAW} much larger than unity, streaming velocity decreases significantly, resulting in a transition from regular (strong) to irregular (weak) mixing [16]. Acoustically induced mixing in a droplet can enhance biochemical reaction and antibody-antigen binding in droplet-based immunoassays [94,95].

Exciting a liquid droplet with acoustic waves deforms the original shape following the Rayleigh angle. The contact angle of the leading edge increases, whereas the contact angle of the trailing edge decreases. The acoustic force confined in the droplet can be experimentally calculated from the asymmetry in the contact angles and the droplet size using:

$$F_{SAW} = 2R_{LG} \sin\left(\frac{\theta_t + \theta_l}{2}\right)(\cos\theta_t - \cos\theta_l) \tag{24}$$

where R is the radius of the droplet and γ_{LG} is the liquid-gas surface energy; θ_t and θ_l correspond to the contacting angles at trailing and leading edge of the droplet on the substrate, see Fig. 3b.

Increasing the RF power leads to a large SAW pressure that excites and stirs the droplet, causing it to vibrate and move along with the SAW. The movement of the droplet is a combination of sliding and rolling, and the ratio of these two is dependent upon the power applied, the droplet size and hydrophobicity of the surface. The transient injection of RF power could cause jetting of small satellite droplets as shown in Fig. 3c, and a large enough RF power and a hydrophobic device surface may lead to jetting of the whole droplet into a thin liquid beam. The ejected droplet induced by the SAW follows the Rayleigh angle as shown in Fig. 3d [96].

Atomization or nebulisation of a liquid has been widely applied in drug delivery to transport drug formulations directly in the form of inhaled particles. The most common atomization methods are jet atomization and ultrasonic atomization. However, there are challenges in generating droplets with diameters ranging from sub-microns to a few microns as required for drug delivery e.g., to the targeted lung area. Nebulisation or atomization using the SAW devices (see Fig. 3e) is able to produce aerosol droplets with a broad size distribution in the sub-micron range, which have been widely reported in literature [97–107].

If a droplet is placed between a pair of IDTs, the SAW energy is dissipated into the liquid droplet, forming a double butterfly-shaped streaming pattern as shown in Fig. 3f. This is mainly due to the two waves propagating into the droplets following the Rayleigh angles induced by the two SAWs from both sides as shown in Fig. 3g. If the device surface is hydrophobic, the waves from the two opposite IDTs can induce vertical jetting of droplets (Fig. 3h) [108] similar to what inkjet technology can achieve with thermal and piezoelectric actuators. The SAW ejector with two opposite IDTs does not require a nozzle head and offers a potentially more cost-effective solution than conventional inkjet technologies. If the device surface is hydrophilic, efficient nebulisation can be achieved as shown in Fig. 3i. To generate an efficient and continuous on-demand nebulisation, various methods have been applied [97–107], including (i) concentrated SAW devices, such as curved or focused IDTs; (ii) super-hydrophilic surface treatment; (iii) using a trench structure to retain the liquid; (iv) using a porous structure such as filter paper which is linked to a large liquid reservoir. Of course, suitable designs of IDT positions can also be used to generate two opposite waves for breaking-up a large droplet.

When the droplet is put on one side of the IDTs of a SAW device, the acoustic force causes a circulation flow, resulting in the concentration of the particles inside the droplet. If the pair of IDTs are placed with an offset, opposite acoustic streaming in the same droplet can be generated. The twisting flow pattern allows particles to move from their high-shear area at the droplet periphery to the low-shear area at the bottom of the droplet centre as shown in Fig. 3j and k. This phenomenon makes the implementation of particle concentration within a droplet possible. If the power is large enough and the device surface is hydrophobic, vertical twisting jetting of droplets can also be achieved with the offset arrangement of the two opposite IDTs as shown in Fig. 3m. If the device surface is hydrophilic, the applied high RF power will enable a broad volume of nebulisation as shown in Fig. 3n.

1.3.3. Continuous-flow acoustofluidics

SAW allows for the implementation of continuous-flow acoustofluidics. Common tasks such as liquid mixing, pumping and droplet generation in microchannels can be controlled with the help of SAWs. Launching a SAW across a microchannel induces secondary acoustic streaming and enhances mass transport perpendicular to the flow direction. A conventional IDT electrode (Fig. 4a) and a curved or focused IDT electrode (Fig. 4b) can be used to enhance mixing in a microchannel.

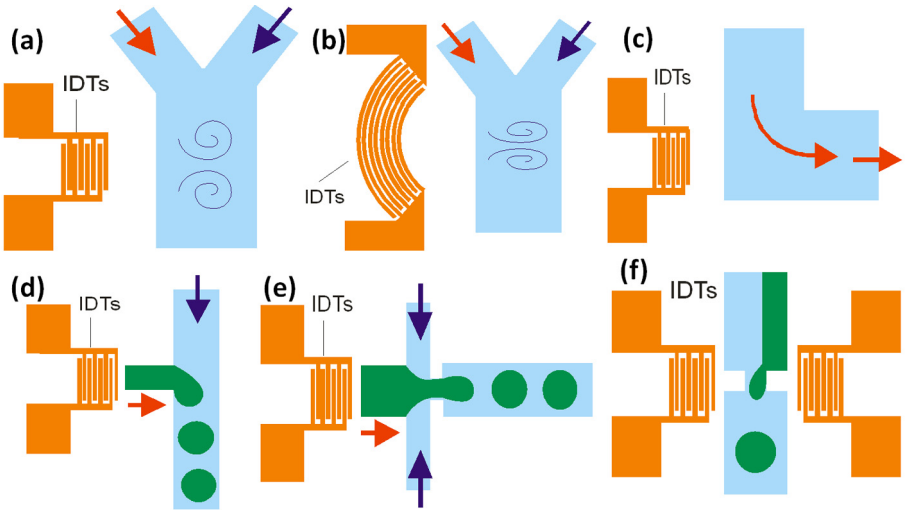

Fig. 4. Continuous-flow acoustofluidics for multiple fluid phases: (a) In-channel mixing can be realised from the streaming effect when the microchannel is positioned to be perpendicular to the SAW propagation direction; (b) SAW mixing can be enhanced using curved IDT structures; (c) pumping of liquid in channel can be realised by appropriately arranging the IDT direction with the microchannels; (d) Droplets generated within the microchannels through a T-junction; (e) droplet generated within the microchannels through a flow-focusing configuration; (f) droplet generation by using two IDTs to squeeze the dispersed phase from two sides of the microchannel.

Compared to the conventional IDT, the focusing IDT structure can achieve the same mixing efficiency with a much lower SAW power.

Pumping of liquid in channel can be realised by appropriately arranging the IDT direction relative to the microchannels. Fig. 4c shows an example of the possible arrangements. Attention has to be paid to maintain the size of the induced vortex to be larger than the channel width, so that pumping can occur. A smaller vortex only induces a recirculation due to the back flow of liquid within the channel. A larger vortex restricts the back flow with the channel wall, leading to continuous pumping of liquid forward in the microchannel.

SAW actuation is one of the several actuation methods for the control of droplet formation in droplet-based microfluidics [2]. Conventionally, droplets are formed in a T-junction configuration (Fig. 4d) or flow-focusing configuration (Fig. 4e). Droplets are formed during the competition of the interfacial tension and the hydrodynamic pressure as well as the hydrodynamic shear between two immiscible liquid phases. Positioning the IDT to launch the SAW in the same direction of the flow of the dispersed phase would allow the control of the droplet size and the formation frequency, as additional acoustic energy is induced to overcome the interfacial tension between the two phases. Launching SAW perpendicular to the dispersed phase would also increase the shear at the interface, allowing the breakup of droplets on demand (see Fig. 4f). These types of on-chip microfluidic plug steering or on-demand droplet generation devices have been reported using SAWs [109–111].

Recently, continuous-flow acoustofluidics have been extensively explored for particle counting, alignment, sorting and separation, as well as droplet generation. The standing acoustic waves can be utilized for this purpose, based on the fact that the nodes and antinodes formed by the standing SAW/ultrasound waves can be incorporated within a microchannel or chamber [112,113]. Fig. 5a and b illustrate the schematic principle of a SAW-based particle sorting device. Standing waves between two identical IDT electrodes can be quickly formed upon applying an RF signal. The pressure node in the channel confines particles suspended in the flow, generating a focused particle stream. If the two IDTs are placed in parallel (Fig. 5c), the pressure nodes form lines in the microchannels. Particles are focused to these lines similar to hydrodynamic or electrokinetic focusing. Proper alignment of the focusing line with the outlet channels can achieve particle sorting. If the two IDTs are placed perpendicularly, the pressure nodes form an array of trapped particles (Fig. 5d). This array could present a platform for particle manipulation, patterning, sorting and detection.

The shift between different resonant frequencies of the devices can be used to manipulate a relatively large range displacement of particles, whereas controlling the phase shift of a given frequency could further precisely control minor displacement of particles. Manipulation of particle position x using SAW phase shifting is described as [114,115]

$$\Delta x = \frac{1}{2k}\Delta\varphi \tag{25}$$

where Δx, $\Delta\varphi$, *and* k, are the displacement of particles, the phase shift and the wave number, respectively.

Dispersive IDTs (or chirp transducers, i.e., a single multi-frequency IDT with varying electrode widths, and more on IDT designs will be introduced in Section 5.2) and slanted IDTs have been used to generate different frequencies in one device by locally changing the electrode periodicity. This type of transducer can be used to control wave modes and reflectivity, and to

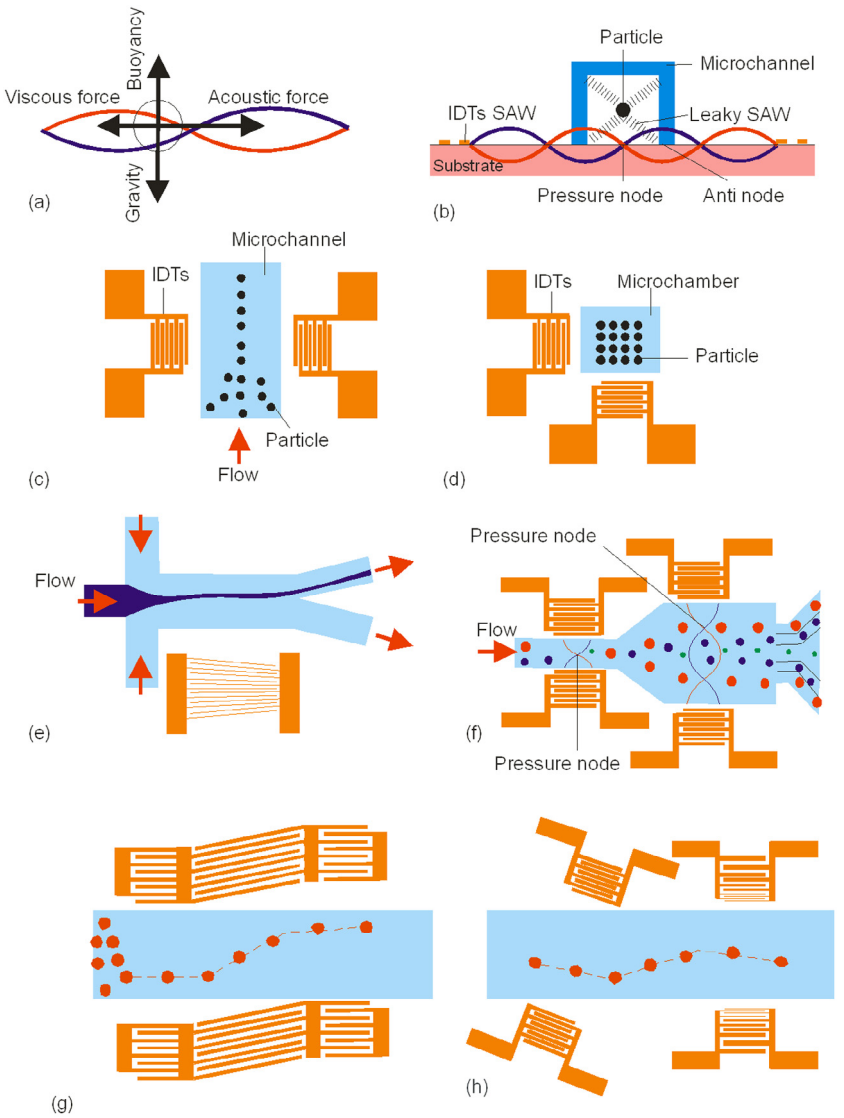

Fig. 5. Continuous-flow single-phase acoustofluidics: (a) Schematic illustration of different forces applied onto the particle in the liquid, including gravity, buoyancy force, viscous force and acoustic forces; (b) schematic principle of a standing wave interacting with particles for alignment; (c) illustration of alignment of particles based on a standing wave in a microchannel; (d) matrix formation of trapped particles due to interaction of SAWs from two IDTs placed perpendicularly forming standing waves; (e) changing the flow direction of particles by modifying the operating frequency of a slanted IDTs; (f) separation of particles of different sizes using successive pairs of IDTs; (g) continuously changing IDT patterns/directions resulting in continuous movement of particles; or (h) particle manipulation by changing the alignment direction of the microchannels vs. those of the IDTs, and using a dispersive IDT with varying frequencies to manipulate the particles.

linearly modulate the wave pitch or frequency. The slanted IDTs are able to change the direction of movement of particles by modifying the operating frequency continuously, as illustrated in Fig. 5e. By changing positions/distance of a successive pairs of IDTs (see Fig 5f); or continuously changing IDT patterns/directions (see Fig. 5g); or changing alignment direction of the microchannels vs. those of the IDTs, or using a pair of dispersive IDTs to manipulate the particles (see Fig. 5h), the particle alignment patterns can be modified or the particle can be effectively separated. More information about microfluidics using acoustic wave technologies, as well as particle manipulations has been reported in many recent review papers [116–119].

2. Bulk or thin film acoustic wave technologies?

Piezoelectricity occurs in many anisotropic materials whose internal structures lack a centre of symmetry. These materials include quartz (SiO_2), lithium tantalite ($LiTaO_3$), lithium niobate ($LiNbO_3$), sapphire (Al_2O_3), lead zirconate titanate (Pb(Zr,Ti)O_3, PZT), barium strontium titanate ($Ba_xSr_{1-x}TiO_3$, BST), AlN, ZnO, GaN, SiC and InN [120]. Table 2 lists the key

Table 2
Comparison of common piezoelectric materials.

Materials	ZnO	AlN	PZT	ST-cut Quartz	Sapphire	GaN	128°Cut $LiNbO_3$	36° YX cut $LiTaO_3$	PVDF
Density (10^3 kg/m^3)	5.61–5.72	3.25–3.3	7.57	2.65	3.98	6.095–6.15	4.64	7.45	1.78
Moulus (GPa)	110–140	300–350	61	71.7	350	320	130–170	205	2.5
Poisson's ratio	0.36	0.22–0.29	0.27–0.3	0.17–0.2	0.23–0.30	0.183	0.24–0.28	0.17–0.2	0.33–0.4
Refractive index	1.9–2.0	1.96	2.40	1.46	1.76	2.3–2.5	2.29	2.18	1.42
Piezo-constant d33 (pC/N)	12	4.5, 6.4	289–380, 117	2.3 (d11)	6.4	4.5	12	12	−35
Effective coupling coefficient, k^2 (%)	1.5–1.7	3.1–8	20–35	0.1–0.2		0.13	5–11.3	5–6.6	2.9
Acoustic velocity of longitudinal (transverse) waves (m/s)	6336 (2720)	10,150–11,050 (5800)	4500 (3900)	5000–5960 (3159)	11,300 (5703)	8050 (4130)	3680–3980	4160–4220	2600
Dielectric constant	8.66	8.5–10	380	4.3			85 (29)	54 (43)	6–8
TCF (ppm/°C)	−40 to −60	−19 to −25		0		28.3	75	−30	
Coefficient of thermal expansion (CTE, $\times 10^{-6}$)	4–6.5	5.2	1.75–2	1.5	5.8	3.17	15	−16.5	42–75

properties of these piezoelectric materials. Among them, AlN has the largest wave velocity and PZT has the largest electromechanical coupling coefficient. Quartz is widely used because of its very low temperature coefficient of frequency, leading to a good thermal stability for precision sensing applications. Rayleigh SAWs can be generated on 128° Y-X-cut $LiNbO_3$ and X-112° Y-cut $LiTaO_3$ substrates. SH-SAW can be generated on 36° Y-X-cut $LiTaO_3$ and 64° Y-X-cut $LiNbO_3$ substrates. Thus these devices are generally used for sensing in liquid media or high humidity conditions as the polarization of the acoustic wave is shear horizontal, limiting acoustic radiation into the liquid. Together with the widely used ST-cut quartz, these substrate materials are popular substrates for making Love-mode SAW devices. Langasite, langanite and langatate have relatively large electromechanical coupling coefficient, with operating temperatures up to 850 °C and thus are promising for making high-temperature acoustic wave devices [121].

Most acoustic devices have been made from these bulk piezoelectric materials, but are often expensive and cannot be easily integrated with electronics for control and signal processing. In addition, they are also generally brittle and fragile when polished into very thin structures for high-frequency applications.

2.1. Why thin film acoustic waves?

Acoustic wave technologies based on piezoelectric thin film materials such as ZnO, AlN and PZT [98,122] have been considered as one of the major technologies for future acoustofluidics and LOC devices [123]. As these applications use thin films, rather than expensive and brittle bulk materials or substrates, microelectronics, sensors and microfluidics can be conveniently integrated into a single LOC device at a low cost.

The piezoelectric thin film also enables the integration of multiple functions onto different substrates such as silicon, glass, metal, or polymer. Polymers are particularly important for development of flexible and wearable sensing devices, tactile transducers and energy harvesting devices based on these piezoelectric films [124–127].

Another key advantage of piezoelectric thin films is that the film can be deposited only onto the areas where the acoustic wave is required [128]. The piezoelectric film does not need to be deposited onto other areas, because once generated the wave can propagate along the substrate without the need of the piezoelectric top layer. In this way, other components such as the microchannels, chambers and sensors can be directly fabricated on the substrate without requiring the existence of piezoelectric films. Selective deposition of the piezoelectric film significantly simplifies SAW devices and microsystems, and can avoid direct contact between the active layer and the liquid.

Table 3 details the general film characteristics required for the successful integration of piezoelectric films for acoustic wave bio-sensing and microfluidic applications.

Among the piezoelectric film materials, PZT has the largest piezoelectric constant and electromechanical coupling coefficient. However, PZT films have disadvantages for biosensing applications such as high acoustic attenuation, low quality factor, high energy loss, low sound wave velocity, poor biocompatibility (high toxicity of Pb). Worst of all, PZT films are difficult to fabricate. This is especially important for films thicker than a few microns and generally much thicker piezoelectric films (>20% of wavelength) are necessary for SAW generation. The requirement for high temperature annealing and high electric field polarization also make PZT films unsuitable for integration with microelectronics, particularly the complementary metal-oxide semiconductor (CMOS), as well as other MEMS devices. Therefore, the present review will not cover the work on the PZT films for acoustic wave applications. The readers may refer to other review papers for more information on these if required [129–132].

Currently, ZnO and AlN are the most popular thin film materials in SAW-based microfluidics and LOC devices [133]. Gallium nitride (GaN), gallium arsenide (GaAs), and polyvinylidene fluoride (PVDF) are also alternative materials being inves-

Table 3
Basic requirements for thin film structures for acoustic wave bio-sensing and microfluidic applications.

Microstructure considerations	• Dense structure with low porosity • High crystalline quality and low defect density • Strong texture • Smooth surface and low roughness • Good stoichiometry (Zn/O or Al/N ratio) • Uniformity in film microstructure and thickness
Piezoelectric properties	• High electromechanical coupling coefficient, k^2 • High frequency and large acoustic wave velocity • Good thermal or temperature stability (low thermal coefficient of frequency or velocity) • High quality factor Q • Low acoustic loss and low damping
Fabrication requirements	• Low film stress/good adhesion to substrates • Easy deposition on different substrates and substrates with complex shapes • Cost effectiveness and mass production • Compatibility with MEMS or CMOS technology • High deposition rate • Easy etching/patterning/processing • Reproducibility/high yield
Biosensing:	• High sensitivity, resolution, and selectivity, with low noise level. • High thermal stability and low TCF value • High Q factor • Easy functionalization of surfaces for immobilization of antibodies, etc. • Biocompatibility • Chemically inert • Less environment dependent • Low power required • Robust or flexible • Remotely accessed. • Fast response and low hysteresis.
Microfluidics	• Chemically inert • Robust or flexible • Handling of high power without fracture • Easy surface modification • Mass fabrication • Optically accessible for observation • Control surface hydrophobicity • Compatible with sensing technology

tigated for piezoelectric applications, though they possess low electro-mechanical coupling coefficients. GaN films have frequently been applied for fabricating SAW [134–136] and Lamb wave devices [137–139] due to its high acoustic velocities (for both Rayleigh and Sezawa modes), high frequency (GHz range) and compatibility with microelectronics and CMOS. Thin films of $LiNbO_3$, $LiTaO_3$, $KNbO_3$, $SrTiO_3$, $BiFeO_3$ and $BaTiO_3$ have also been investigated for Lamb waves, SAW, BAW, or FBAR devices because of their large electromechanical coupling coefficients, but often suffer from poor control of film stoichiometry, orientation, texture and process parametres [140–146].

2.2. Why (and why not) ZnO?

ZnO is an attractive proposition for electronics, optoelectronics, photonics, piezoelectrics, acoustics as well as sensing applications [147,148], especially with its higher piezoelectric coupling coefficient compared to that of AlN. In addition, the film stoichiometry, texture and other film properties are more easily controlled than those of AlN films. Furthermore, good film crystallinity can be easily obtained without substrate heating during deposition [149]. Zinc oxide normally has a low film stress and a relatively good adhesion with most substrates, including glass and polymers, enabling films of tens of microns thick to be deposited. Hence, ZnO is suitable for thick film SAWs or ultrasonic devices operating in the lower frequency range as compared to AlN films [150]. This material is considered as biosafe and therefore is suitable for biomedical applications.

Although the acoustic wave velocity of ZnO is not as high as that of AlN (see Table 2), SAW devices with a higher operating frequency can be realised by depositing ZnO films onto AlN, sapphire (Al_2O_3) and diamond layers which have much higher acoustic velocities [151]. Other advantages for ZnO are that nanostructured ZnO and ZnO nanowires can be easily prepared on bulk wave devices, thin film SAW devices or FBARs. These nanostructures and nanowire decorated acoustic wave devices have been intensively explored for sensing applications [152–155]. The fabrication of ZnO nanowires/nanorods on top of the ZnO film can be easily prepared using a one-step procedure [156].

However, the strong reactivity of ZnO films is a major concern for biomedical applications. This material is unstable if it is exposed to moisture or water over a long period of time. Therefore, stability and reliability of ZnO-based devices are

potential problems, although these can be solved by surface protection or packaging. In addition, ZnO has a high dielectric loss and is not stable at temperatures above 500 °C, making it unsuitable for high temperature applications. Finally, it should be noted that Zn is considered as a contaminant in the CMOS or integrated circuit (IC) processes, and is also incompatible with process equipment such as cryo-pumps.

2.3. Why (and why not) AlN?

AlN has good mechanical properties and can withstand high temperatures. For example, AlN can maintain good piezoelectric properties in air up to 700 °C or inert atmospheres up to 1000 °C [157–159]. The material has a large propagating wave velocity, good dielectric properties, high thermal conductivity and high breakdown voltage [160–162]. Therefore, AlN potentially enables the development of acoustic devices operated at higher frequencies and higher powers, with improved sensitivity and performance at high temperatures and in harsh environments [163–165]. AlN films are suitable for SAW devices with high frequencies above hundreds of MHz or GHz and FBAR devices with better power handling capabilities than ZnO [166–171]. In contrast to ZnO, AlN deposition and processing are fully compatible with CMOS and MEMS processes [172,173].

However, the deposition of AlN films and their texture control are more difficult than in the case with ZnO films [174]. AlN films are normally sputter-deposited at elevated temperatures (typically 200–400 °C) to achieve an optimal performance, although room temperature deposition is often used. Also deposition conditions, especially oxygen or moisture in vacuum chambers, have significant effects on AlN film growth and microstructure. Growing AlN films thicker than a few microns is particularly challenging because of the large film stress and the tendency to form microcracks. Therefore, it is generally agreed that AlN film is suitable for devices operating at high frequency with much thinner thickness requirement, whereas ZnO film is suitable for acoustic wave devices operating at a lower frequency range using much thicker films. Finally, AlN nanowires are not as frequently reported as ZnO nanowires and to date have not been widely used in biosensing applications [175].

2.4. Acoustic wave devices using ZnO and AlN films

Commonly used acoustic wave devices based on piezoelectric ZnO and AlN thin films include Rayleigh, SH wave and Love wave SAWs, FBARs and Lamb wave/FPW devices. Thin film ultrasonic transducers consisting of a top electrode, a piezoelectric film and a back electrode can be fabricated and operated over a large frequency range from 20 kHz to tens of MHz. They are typically used for non-destructive testing, low frequency sensing, and biomedical imaging based on the microcantilevers [176,177] and membranes [178–180]. The present review does not discuss these applications.

Low frequency Lamb waves or FPW for liquid biosensing have been discussed in Section 1. However, this wave type has not been extensively studied in the past decade due to the low operation frequency and the fragile nature of the device structure. Recently, thin film devices, which generate higher Lamb wave modes with high frequencies up to hundreds of MHz, have been developed and used for both sensing applications and microfluidics. These applications are discussed in detail in Sections 6 and 7.

SAWs based on ZnO and AlN films have been extensively studied for both biosensing and microfluidic applications. A potential problem of thin film based SAWs is the inconsistency of acoustic wave properties from devices produced using different deposition techniques and facilities. The frequency and velocity of the acoustic waves, as well as the transmission properties, are dependent not only on the piezoelectric film properties, but also on the ratio between the film thickness and wavelength. Therefore, controlling device properties for thin film acoustic wave devices is perhaps the most important and challenging task, especially for electronic applications where devices with fixed frequencies are required. Similarly, multilayer structural designs combining various thin film layers are often required to improve device performance, mechanical strength, temperature stabilities and to increase resonant frequency [181].

FBARs are the latest development thin film acoustic wave devices. The mechanical resonance is generated from the electric field applied to the piezoelectric films between the two electrodes. In order to enhance the resonant signals, the working piezoelectric unit of the FBARs is often isolated acoustically from the supporting substrates, either using a multilayer Bragg mirror structure, or FBAR-on-air cavity structures, or on a polymer support layer on a substrate with very different acoustic impedances from that of the FBAR layer (as discussed in Section 1.1.1). The design of FBARs has less freedom than that of SAW devices because the frequency is mostly determined by the piezoelectric layer thickness and acoustic velocity rather than by lithographic patterning. FBAR devices are also extremely sensitive to environmental changes or external vibrations, thus a good isolation from the atmospheric environment is required. Applications of ZnO/AlN SAW and FBARs for biosensing and microfluidics will be discussed in detail in Sections 6 and 7.

2.5. Multi-layer thin film acoustic wave structures

In this paper, thin film acoustic wave devices are defined such that the main piezoelectric component is the thin film itself and the bulk substrates are non-piezoelectric materials. The physical/chemical and piezoelectric properties of the piezoelectric films contribute significantly to the device performance. A number of acoustic wave devices use thin piezoelectric layers on a bulk piezoelectric substrate, but these belong to a class of layered acoustic wave devices [182–184]. Such layered

devices generally show improved sensitivity and functionality compared with those that use non-piezoelectric layers on the same piezoelectric substrates [185–191].

Different layers have been used in thin film acoustic wave devices to improve temperature stability, phase velocity and electromechanical coupling coefficient [192]. The performance of these multilayer devices depends not only on acoustic velocities, the coupling coefficient, and the mechanical/electrical/chemical/physical properties of the films, but also on the film thickness of each single layer. Therefore, dispersion effects need to be considered, *i.e.*, the phase velocity and electromechanical coupling coefficient change significantly with the film thicknesses, which will be discussed in Section 4.3.

Generally, there are two different design strategies to consider for the integration of two successive layers into the acoustic wave devices [193]:

(1) Slow-on-fast structure (for example, ZnO on diamond, or ZnO on AlN, which is generally used to generate guided Rayleigh modes, Love mode, or Sezawa modes).
(2) Fast-on-slow structure (for example, AlN on ZnO, or thin film on a polymer, which are generally used to generate higher velocities of SAWs or bulk waves compared to that of the bottom layer [194]).

Fig. 6 shows six types of two-layer designs on a substrate, which will be used as a simple example. The substrate materials can be either piezoelectric or non-piezoelectric (such as Si, glass and polymers). The six designs include:

(i) Type 1: the IDTs can be on top of substrate, and either the substrate or the intermediate layer must be piezoelectric.
(ii) Type 2: the IDTs can be on top of intermediate layer, and either the intermediate or the top layer must be piezoelectric.
(iii) Type 3: the IDTs can be on the top layer, and in this case the top layer must be piezoelectric to excite the acoustic waves.
(iv) Type 4: two same types of IDTs on both intermediate and top layers to enhance the acoustic wave generation.
(v) Type 5: the IDTs can be located on top of the piezoelectric film with a short-circuiting plane underneath.
(vi) Type 6: the IDTs can be located under the piezoelectric layer with a short-circuiting plane on top.

Based on Fig. 6, the functions of different layers in thin film acoustic wave devices can be summarised as follow:

- A piezoelectric film can be deposited onto a non-piezoelectric substrate for wave generation and propagation. This allows the SAW device to be fabricated on the same substrate as other components in a MEMS or CMOS system, thus increasing the design flexibility. The IDTs can be either on the piezoelectric layer or beneath the piezoelectric layer, in order to generate the acoustic waves. In the latter case, the substrate (such as Si) below the piezoelectric layer should have a high resistance or otherwise, an insulator layer is needed to separate them.
- Adding a piezoelectric layer with a high permittivity above the IDTs increases the electromechanical coupling, allowing fabrication of devices with reduced insertion loss or smaller size [195].

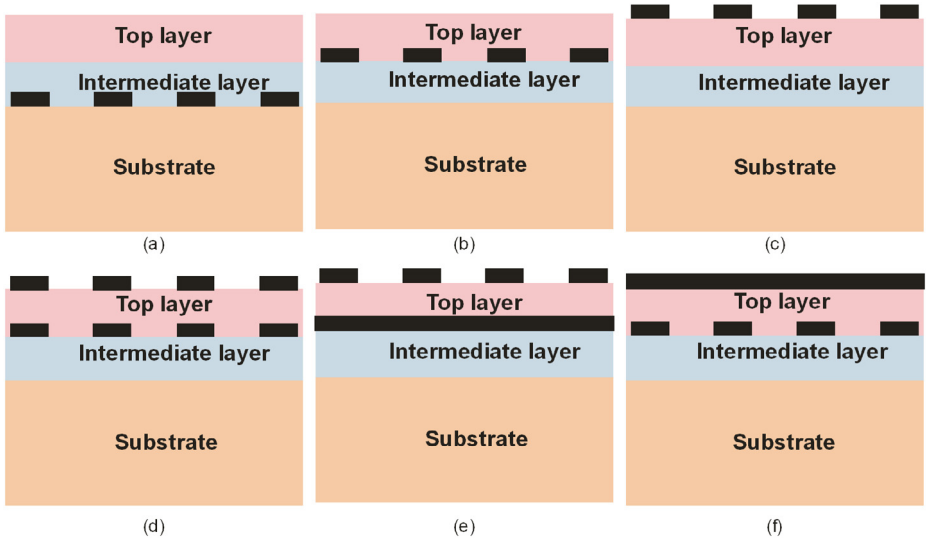

Fig. 6. Examples of two different designs of layered SAW structures: (i) Type 1: the IDTs can be on top of substrate, and either the substrate or the intermediate layer must be piezoelectric to excite acoustic waves; (ii) Type 2: the IDTs can be on top of intermediate layer, and either the intermediate or the top layer must be piezoelectric; (iii) Type 3: the IDTs can be on the top layer, and in this case the top layer must be piezoelectric; (iv) Type 4: two same type IDTs on both intermediate or top layers to enhance the acoustic wave generations; (v) Type 5:the IDTs can be located on top of the piezoelectric film with a short-circuiting plane underneath; (vi) Type 6: the IDTs can be located under the piezoelectric layer with a short-circuiting plane on top.

- By selecting a suitable material, the multi-layer structures can potentially increase the acoustic wave velocity and electromechanical coupling coefficient of the device, resulting in a lower insertion loss and allowing the device design to be physically smaller [196–198].
- A layered structure can significantly increase the confinement of acoustic energy within the surface layer, and improve the sensitivity and electro-mechanical coupling coefficient. This is the key idea for the Love wave/layered guided wave designs [199].
- Combining multilayers such as doped ZnO and GaN on a substrate with a high acoustic wave velocity such as Al_2O_3 could result in excitation of higher order SAW modes with a higher velocity, and enable the modulation of the SAW velocity, thus forming tuneable SAW acoustoelectric devices [200].
- Adding a piezoelectric or dielectric layer above the IDTs increases the electromechanical coupling, thus allowing fabrication of devices with reduced insertion loss or smaller size.
- Adding a dielectric film with a larger velocity than the substrate (for example, using an AlN layer) can significantly reduce the attenuation of the longitudinal type leaky surface acoustic waves.
- A sensitive layer or nanostructured layer is frequently used as the top layer for improving the sensing performance, or modifying the device surface for microfluidic functions.
- A combination of AlN/SiO_2 or ZnO/SiO_2 is commonly used to improve the temperature stability [201–210] and to obtain a zero order TCF. Of course, it is necessary to optimise the film thicknesses of different layers to achieve this zero order TCF.
- ZnO/SiO_2/Si or AlN/SiO_2/Si structures have also been proposed for use as Love-mode types of SAW sensors [211–213], although the dominant shear-mode waves have not been clearly identified in these devices.
- Lattice mismatch and differences in TCFs between the top piezoelectric layer and substrates are important issues which can be improved by using an intermediate layer or multi-layer structure, for example, AlN/3C-SiC/Si [214]. Stresses in the sensing or piezoelectric layers could also be reduced by adding intermediate layers.
- A hard insulating top layer can be used to shield the electrode of the piezoelectric film or shield ZnO or sub-layers and the substrate from harsh environments or liquids, thus enhancing the long term stability of the devices [215].
- Superlattice structures such as a periodic AlN/ZnO multilayer design can be formed with two or more layers of materials of different properties. The layers are stacked periodically, thus yielding an enhanced performance with a higher coupling coefficient or a better temperature stability than that of a single layer [216].
- Adding a metal buffer layer can significantly improve the electromechanical coupling coefficient of the acoustic wave devices (see Fig. 4d and e) [217].
- The acoustic velocity of a piezoelectric film significantly depends on the sub-layer which has a large acoustic velocity. Using a substrate or sub-layer with a higher acoustic velocity can increase the wave velocity in the ZnO or AlN-based SAW devices. For example, the shear acoustic velocity of ZnO film is 2724 m/s, but it can be increased to 4522 m/s for ZnO/AlN films, and then reach 12,200 m/s for a ZnO/AlN/diamond layer system. AlN, diamond like carbon (DLC), nanodiamond films and diamond have been regarded as the best substrates to provide a dramatic increase in acoustic wave velocities associated with ZnO films [218–221].

However, multi-layered acoustic wave devices could have a number of issues such as increased film stress, significant dispersion effects, increased surface roughness, decrease in wave amplitude and large insertion losses. Theoretical analysis or finite element analysis (FEA) is needed for optimisation of each layer thickness in the multilayer acoustic devices and identification of the various generated wave modes and vibration patterns [222]. A common problem with the multilayer designs is linked with the generation of various wave modes or hybrid modes (*i.e.,* a combination of different types of bulk, leaky, Rayleigh or Sezawa wave modes) [223], as well as spurious modes and pseudo-acoustic waves (bulk waves) with a large attenuation in the substrates [224,225]. Spurious modes are unintentionally excited modes, which can interfere with the main mode, causing ripples in the transmission spectra. These could be acoustic leakage waves into the substrate, laterally escaping waves, scattered waves, and/or vibrations due to the electrodes. Spurious modes can be reduced by using apodization (using modified IDT patterns, or non-parallel resonator shapes as will be discussed in Section 5) or by changing electrode geometry (for example, by adding extra mass loading to the edge of electrode), which can reduce the constructive interference between the incident and reflected waves [226].

3. Deposition and MEMS processing of ZnO and AlN films

3.1. Thin film deposition techniques

Many deposition methods have been developed to prepare ZnO [227] and AlN films including physical vapour deposition (PVD) methods, such as sputtering [228–231], evaporation [232], pulsed laser deposition (PLD) [233–242], filtered cathode vacuum arc (FCVA) [243–247], sol-gel processing [248–250], ion beam deposition [251], molecular beam epitaxy (MBE) [252–256], chemical vapour deposition (CVD) [257–260], plasma enhanced CVD (PECVD) [261–264], metalorganic chemical vapour deposition (MOCVD) [265–268], and atomic layer deposition (ALD) [269].

Table 4 summarizes the main features of different deposition methods in relation to ZnO and AlN thin films. The selection of a deposition approach depends on the desired crystalline quality of films, deposition throughput, process temperatures

Table 4
Summary of different thin film deposition methods and features for ZnO and AlN films.

Deposition technique	Key features and technology variants	Compatibility with MEMS processing
Sputtering	• Most used method • DC and RF magnetron sputtering, HiPIMS, HiTUS, Microwave-sputtering, UV sputtering • Best deposition temperature: ZnO film room temperature to 300 °C; AlN film 300–500 °C	• Compatible with MEMS process • Reasonably high deposition rate • Can be large scale
MBE	• Precise control over the deposition parametres • Control of interface chemistry • Extremely high purity and highly crystalline thin films • Very slow deposition rate • Very high deposition temperatures: 600–1000 °C • Small deposition area	• Atomic layer by layer growth attributed to the crystallographic relation between film and substrate • Not compatible with MEMS processing
PLD	• Using high-power laser pulses to remove target material • Relatively good crystalline structure and quality, able to create high-energy source particles, high-quality film growth at potentially low substrate temperatures • Not favourable for industrial application, although widely used in research • Typically deposition temperatures are from room temperature to 600 °C	• Expensive, • Deposition only over small areas
CVD	• High-quality films and applicable to large-scale production • Including PECVD and MOCVD • Typically deposition temperatures from 300 to 800 °C	• Good quality of films, • Low deposition rate • high temperature is a potential issue
Sol gel	• Simple, low cost, solution based method, no vacuum • Crystal quality of the thin films is typically poor with random crystal orientations, small grain sizes, rough surface, etc. • Easily prepared at low temperature, but need high temperature annealing	• Suitable for porous nanostructure growth • Deposition is compatible with MEMS processing • Poor film quality • Less used for acoustic wave device fabrications
FCVA	• High ionization ratio • High ion drift energy • Good adhesion and good coating quality • Deposition temperature can be from room temperature to 500 °C	• Small scale • Not compatible with MEMS processing • Deposition rate is not high

and cost, as well as the availability of equipment. Among these deposition methods, magnetron sputtering is preferred due to its simplicity, good reproducibility, low cost, low operating temperature, and compatibility with microelectronics and MEMS processing. Furthermore this technique is already in production for fabrication of SAW and FBAR filters and frequency duplexers. Therefore, this section will focus on the sputtering technique.

Films of ZnO and AlN can be deposited at room or elevated temperatures, either by DC/RF sputtering from high-purity metallic Zn or Al targets [270], or by RF sputtering ceramic ZnO or AlN targets, all in an Ar and O_2 (or N_2) gas mixture (with an illustration shown in Fig. 7a) [271]. At the same target power, the sputtering rate of the RF process is lower than that of DC sputtering, although RF deposition may produce films with a smoother surface.

During DC sputtering using a metallic target of Zn or Al, the process parametres need to be optimised to prevent charge build-up on the metallic target. These phenomena are often called target-poisoning and target arcing, which can significantly affect deposition rate, surface roughness and crystal quality of the films. These problems can be solved to some extent by using plasma emission monitoring control systems [272], or using a balanced magnetron with high strength magnets (see Fig. 7b), or using a pulsed power source, or using extra ion beam/plasma sources to enhance the reactive sputtering process.

Ultra-violet (UV) assisted sputtering deposition has also been proposed [273] to prepare AlN or ZnO films. The UV radiation can directly raise the substrate temperature and increase the kinetic energy of gas radicals/ions, which increase the sputtering rates, ionization rate of species in the plasma, and thus the energy of adatoms to the substrate.

Another key problem for a standard DC magnetron sputtering is the low ion energy of a few eV and low ion flux. These problems can be solved by using a pulsed DC system. During pulsed sputtering, the target potential is periodically switched between ground and a positive potential, at a frequency in the range from 20 to 350 kHz [274,275]. If the pulse is on, ions are attracted to the target via standard sputtering. If the pulse is off, an electron current is drawn to the target, which can discharge any poisoned regions [276,277]. Using an unbalanced magnetic field is another common method to increase collision/ionization and ion bombardment and thus improve the deposition process, film texture and microstructure, especially for AlN films. In this method, the magnetic field at the target edge is commonly modified to concentrate the plasma onto substrates as shown in Fig. 7c [278–281]. In order to increase the plasma density/sputtering rate, increase plasma density and shorten the deposition time, a dual magnetron sputtering system with two unbalanced magnetrons has also been used as shown in Fig. 7d.

Pulsed magnetron sputtering still shows a low degree of ionization and low ion current density. High power microwave plasma sources can be applied for the oxidation or nitriding of thin metal (i.e., Zn or Al) layers in a dynamic deposition process, *i.e.,* applying a microwave assisted pulsed sputtering process. A very thin metallic or sub-stoichiometric film (a few nm thick) is firstly deposited using pulsed magnetron sputtering and then oxidized (or nitrided) afterwards using a microwave

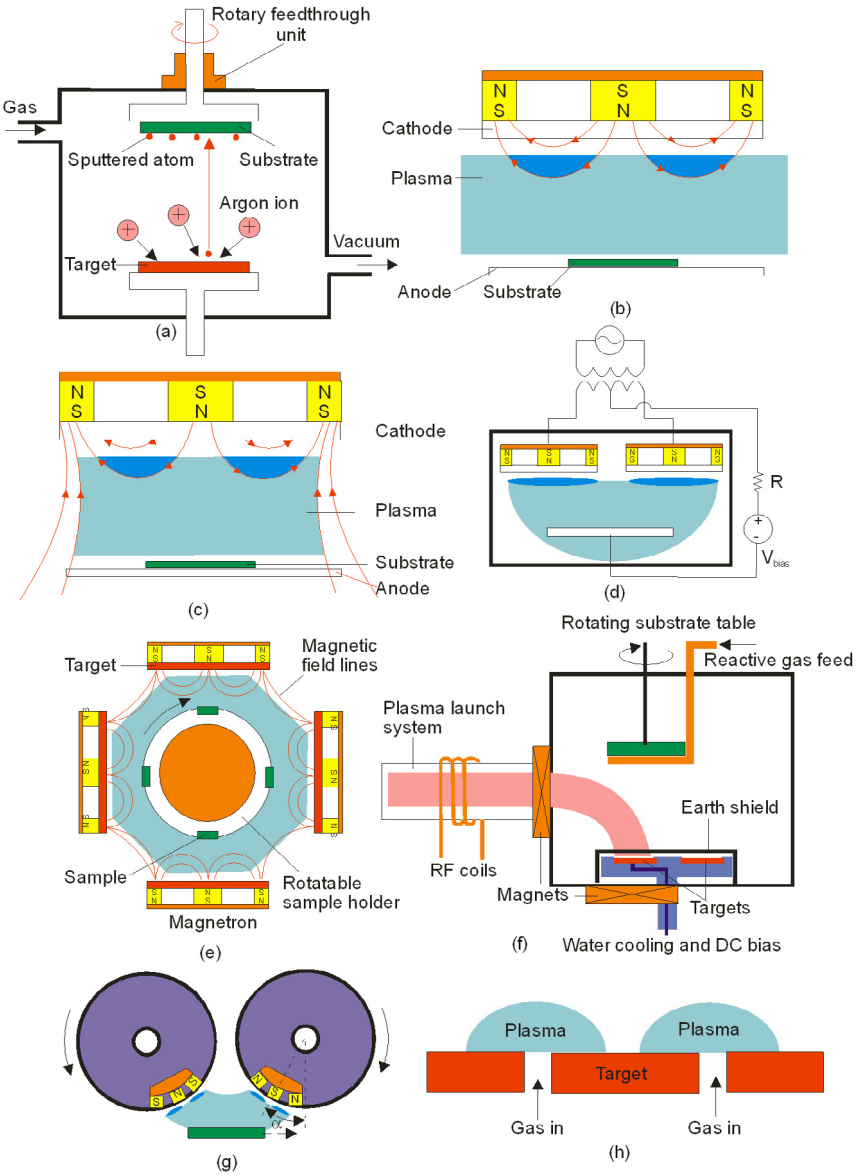

Fig. 7. Illustration of the operation principles of common sputtering systems: (a) Standard DC/RF sputtering; plasma confinement in: (b) a balanced magnetron sputtering; (c) an unbalanced magnetron sputtering; (d) dual magnetron sputtering system with two unbalanced magnetrons; (e) closed field unbalanced magnetron sputtering system with HiPIMS sources to increase plasma density and trap electrons ejected from the magnetron targets; (f) working principle of high target utilisation sputtering (HiTUS); (g) plasma confinement in a dual rotatable tube magnetron sputtering; (h) working principle of a hollow cathode magnetron sputtering system.

source based on a rotating drum holder. Compared with RF discharges, at an equal power density, the average microwave power density is higher, resulting in enhanced molecular dissociation rates. Consequently, higher thin film deposition rates can be obtained with microwave discharges [282]. The microwave plasma (2.45 GHz) leads to a high ionization efficiency, and activates the reactive species in the plasma so that the reaction between the metal species and the reactive gas takes place more effectively. Another advantage of microwave enhanced sputtering is that the microwave system can be separated from the main deposition chamber. However, the deposited films generally have large stresses and high roughness, due to microwave plasma bombardment effects. In order to further increase microwave coupling and electronic density, a supplementary device such as an electron cyclotron resonance (ECR) can be used in microwave discharges. This is based on the generation of a magnetic field which is added to the microwave field, and confines the plasma at resonant conditions [283,284].

High power impulse magnetron sputtering (HiPIMS) can also be applied to permit a decrease in substrate temperature by increasing the target power density. In the HiPIMS process, extremely high power densities in the order of kW cm^{-2} in short

pulses of tens of microseconds and a low duty cycle (<10%) are used at the target to avoid overheating of the target/system components [285,286]. Therefore, it can produce a high degree of ionization of the sputtered species and a high molecular dissociation rate, all of which are claimed to result in the formation of high density and smooth films on complex-shaped substrates [287]. The HiPIMS ZnO and AlN films also have very good adhesion to the substrates [288,289]. A sputter design based on the combination of closed field unbalanced magnetron sputtering and HiPIMS sources is illustrated in Fig. 7e. Potential drawbacks of the HiPIMS include the directional nature of the sputtered metal flux and the reduced sputtering rate compared with conventional sputter deposition.

Although magnetron sputtering is the most scalable method, plasma or ion bombardment on the surface of the growing film is unavoidable during typical sputtering deposition. These phenomena may result in changes in the orientation, stoichiometry and grain size of ZnO and AlN crystals, defects, electrical and optical properties, intrinsic stress, as well as the surface and cross-sectional morphologies. To resolve these effects, high target utilisation sputtering (HiTUS) has been proposed to include a side chamber to generate a high density plasma which can be launched into the main deposition chamber, and further steered onto the substrate using an electromagnet, as shown in Fig. 7f [290]. Since the high energy Ar^+ bombardment on the target is decoupled from the deposition of low energy ion species on the growing film, high energy ion-bombardment induced damage can be effectively suppressed, leading to thin films with an extremely low stress and excellent surface smoothness [291], yet with high deposition rates. It also has the advantages of better utilisation and uniform erosion area of the sputtering targets. Piezoelectric films prepared in this manner also have much lower stress than those commonly found in films deposited using RF magnetron sputtering [292–294]. The problems of the HiTUS systems are complex design, limited number of targets, restrictions on the deposition area and possible reduction in the sputtering rate compared to magnetron sputtering.

Another method for high rate deposition of ZnO and AlN film is to use dual rotatable tube magnetron targets (see Fig. 7g), which can effectively enhance the utilisation of target materials, increase continuous operation time and also improve the uniformity of the optical and electrical properties of the deposited films [295]. Balanced and high strength magnet bars are generally used in these rotatables. Roll-to-roll mass deposition using polymer or metallic foil substrates can be easily realised using this technique. A problem with dual rotating magnetrons can be the high target costs.

Hollow cathode magnetrons can sputter material from the inner surfaces of a cylindrical target. Based on a hollow cathode effect (shown in Fig. 7h), sputtering can be realised by letting the gas flow through an opening in metallic targets under a negative electrical potential, thus creating a high flux of ions and enabling large deposition rates as well as uniform deposition onto three-dimensional parts. Due to the confined plasma and increased ionization, magnetron sputtering can be operated at considerably lower pressures than a conventional magnetron sputtering system, which reduces the risk of contaminants in the growing film, and the current dependence on the cathode bias voltage. However, plasma instability and high ignition voltages create challenges for the technology.

3.2. Film deposition parametres

Both ZnO and AlN have a polar wurtzite structure with a preferred crystal orientation (i.e., along the c-axis), which shows the highest piezoelectric constant (d_{33}). Thus, when polycrystalline thin films are deposited, the best piezoelectric activity will be obtained when all the microcrystals are aligned with the c-axis perpendicular to the film surface.

Several process parametres influence the formation of this c-axis structure, as energy is needed to form the preferred c-axis orientation. Most of the sputtering parametres affect the way this energy is provided. Therefore, the microstructure, texture and piezoelectric properties of sputtered ZnO or AlN films are affected by sputtering conditions such as target power, gas pressure, gas flow rates, bias voltage, substrate materials, deposition temperature and annealing temperature [296–299]. Table 5 summarizes the key parametres that influence the film microstructures and properties.

The growth dynamic of ZnO or AlN films by sputtering has been thoroughly studied [314]. In the initial stage of growth, the growth dynamic could be unstable and have high sticking probabilities of the impinging particles, and thus the films normally showed a mixture of textured and randomly oriented crystals. In the second growth regime, the films become more homogeneous and well textured, and the growth is dominated by the shadowing effect induced by the bombardment of impinging particles. Based on this behaviour, a two-step deposition technique has been proposed to increase film texture and reduce film stress by changing either gas pressure or target power during deposition [315–317]. For example, the first stage can be a low–power, high–temperature deposition which provides high migration rate to the surface atom with improved mobility. The second stage might be a high–power deposition at lower temperatures characterized by high deposition rates and low residual stress. Film stress and its measurement/control will be discussed in Section 4.4.

Generally, the film growth conditions are more critical for the AlN films than those for ZnO films. Growing a thick AlN film is a challenging task because of its tendency to form microcracks and high film stress. Residual oxygen or water contamination in the sputtering gas or in the chamber can significantly affect AlN film growth during sputtering [318]. The growth rate of the AlN films decreases with increasing oxygen concentration in the sputtering gas. The predominant polarity of the AlN film also changes from Al polarity to N polarity with increase in the oxygen concentration. Increasing oxygen concentration in the sputtering gas also increases the Al—O bonding, as the bonding energy of Al—O is higher than that of Al—N [319]. This is an important aspect as the oxygen concentration significantly influences the piezoelectric response of AlN films. Therefore, it is essential to minimise the O_2 concentration during the AlN film deposition.

Table 5
Key parametres which influence the film microstructures and properties [300].

Parametres	Attributes
Substrate temperature	• ZnO and AlN thin films can be deposited at room or low temperature (<200 °C) which is compatible with a CMOS back-end process [301] • But the film quality would be better if the films are deposited at higher temperature up to 500 °C • High temperature deposition will enhance the atomic mobility, improves film texture and quality, increases grain size, decreases the defect density, promotes film adhesion to the substrate, and thus could result in a compact and dense film structure[302,303] • The optimal substrate temperature for AlN is between 250 °C and 600 °C [304–308]
Plasma power	• Higher plasma powers will result in a higher deposition rate because the sputter yields are higher and the deposited particles have higher kinetic energies • High plasma power could cause increase in film surface roughness due to excessive atom flux and ion bombardment to the substrate • Film stress becomes large at higher plasma power
Gas pressure	• Deposition at a low gas pressure generally produces a dense and small-grain size film, with a large compressive film stress • Decreasing sputtering pressure improves preferred (002) orientation and to higher crystallinity • Deposition at a higher gas pressure results in porous and columnar films with rough surfaces, with a low compressive stress or large tensile stress [309] • By increasing the sputtering pressure, energy loss of the accelerated ions occurs due to the collision rate increase in denser plasma
Bias voltage	• Increasing bias voltage can accelerate the deposited adatoms, produce a dense film • Too high a bias voltage or an acceleration potential deteriorates the crystal quality because of the bombardment by accelerated ions • Stress becomes larger at higher bias voltages
Ar/O_2 or Ar/N_2 ratio	• The gas ratio is a critical parameter and a sufficient oxygen or nitrogen partial pressure is needed to maintain the stoichiometry of the ZnO or AlN films [310] • The gas ratio could influence the film texture, density/porosity, deposition rate and film stress
Substrate	• Limits the maximum temperature which can be used • Affects film texture and crystal orientation
Post-annealing and post-poling	• For both AlN and ZnO films, as-sputtered film normally exhibits a good piezoelectric effect, therefore, post-deposition poling is unnecessary [311] • Annealing of films could increase film resistivity, reduces film stress and defects, and improve functional properties, such as optical and electrical properties • Higher annealing temperature could result in increased film thermal stress and roughness
Target aging	• Target aging (erosion of target) has a significant effect and will modify bombardment levels from negatively charged oxygen ions generated at the target surface, thus causing significant changes in the ZnO film structure [312] • Usage of target configuration with conical protrusion of the erosion zone has been proposed to solve the target erosion problems, although this will introduce new problems such as complexity and cost of the targets [313]

3.3. MEMS processing of ZnO and AlN films

Various MEMS processes are required to fabricate thin film based acoustic wave devices. ZnO films are relatively reactive [320], thus etching and patterning these films using the methods listed in Table 6 are relatively straightforward. Whereas AlN films are more stable and chemically resistant and consequently etching and patterning of AlN is more of a challenge as detailed in Table 6.

For microfluidics and sensing applications, the device surface is often required to be hydrophobic or hydrophilic, or a pattern combining these two. As-deposited ZnO and AlN films typically have contact angles of water droplet ranging from 40 to 80°, and these are also dependent on surface conditions and UV light exposure [321]. The contact angle of water droplets increases with ZnO film thickness because of the increased film surface roughness. Table 6 lists a few typical methods used to modify device surfaces to become superhydrophilic, hydrophobic or superhydrophobic.

Another critical issue for a good biosensor is to obtain a simple, low cost but reliable process for the functionalisation of the sensing surface to form a robust immobilization of appropriate probe biomolecules. Table 6 also summarizes some reported methods for functionalisation of ZnO and AlN film surfaces.

4. Engineering thin film technologies for acoustic wave applications

4.1. Engineering film texture and wave modes

4.1.1. Texture of films

The texture of piezoelectric films is crucial for the piezoelectric effect and acoustic wave modes as well as the behaviour of the acoustic devices [337–340]. Both AlN and ZnO films crystallize in a wurtzite type structure [341,342] (see Fig. 8a), which is defined by dominant (0002), $(10\bar{1}0)$ and $(11\bar{2}0)$ crystal planes. Taking ZnO film as an example, the surface energy

Table 6
MEMS and bio-processing methods for ZnO and AlN films.

	ZnO	AlN
Wet etching	• HCl, H_3PO_4, HF, HNO_3 • Alkalis • Ammonium chloride • $NH_4Cl + NH_4OH + H_2O$ • $H_3PO_4 + HAc + H_2O$ (1:1:50) • $FeCl_3 + 6H_2O$	• Alkaline aqueous solutions, such as KOH, NaOH, tetramethyl ammonium hydroxide (TMAH) [322–324] • Some acids such as HPO_3, or HNO_3 • Molybdenum, germanium, SiO_2, amorphous silicon can be used as chemical mask
Dry Etching	• Plasma etching using oxygen • Anisotropic etching using hydrogen based gas such as $CH_4/H_2/Ar$ • Toxic chlorine based gases of Cl_2/Ar, BCl_3/Ar and $BCl_3/Cl_2/Ar$ • Ar/H_2 plasma with hydrogen ions to improve efficient and fast etching • Anisotropically etch ZnO films using HBr/Ar plasma [325]	• AlN is normally dry-etched using chlorine based plasma, such as chlorine and BCl_3 • SF_6/Ar plasma is used to etch AlN with highly anisotropic and smooth side walls • Sacrificial layers which have been used include porous Si, phoshosilicate-glass (PSG), porous silicon, metals of Al, Cu, Ge
Surface hydrophobicity	• CHx vapour treatment • Teflon solutions • CYTOP layer from Asahi Glass • Octadecyltrichlorosilane (OTS) with a hydrophobic SAM layer • A monolayer of octadecyl thiol (ODT) or octadecylesilane (ODS) • Hydrophobic nano-structures [326] • microwave plasma-enhanced chemical vapour deposition (MPECVD) [327] • Commercial (e.g. Glaco Mirror Coat “Zero”, Soft 99 Co.) and in-house superhydrophobic coatings [328]	• CHx vapour treatment • Teflon solutions • CYTOP layer from Asahi Glass • OTS with a hydrophobic SAM layer • ODT or ODS • Hydrophobic nano-structures [329] • MPECVD [311] • Commercial (e.g. Glaco Mirror Coat “Zero”, Soft 99 Co.) and in-house superhydrophobic coatings [312]
Surface hydrophilic	• UV illumination to make ZnO surface superhydrophilic [330,331];	• Oxygen plasma to make AlN surface hydrophilic
Bio-processing	• Pre-deposition with Au on ZnO surface, forming a cystamine surface atomic monolayer (SAM) on Au surface • Immobilization of antibodies on ZnO using (1) amine-terminated silane, 3-aminopropltryiethoxysilane, and glutaraldehyde as the secondary cross linker to bind a protein [332,333] • 3-mercaptopropyltrimethoxysilane in toluene to immobilize the antibody • 3-trimethoxysilane in toluene to immobilize the antibody	• Pre-treatment of AlN films with oxygen plasma; or ultrasonication of the AlN film in piranha solutions, and silanisation with OTS [334] • Immobilization of gold nanoparticle bio conjugates onto AlN surfaces using aminosilane molecules as cross-linkers [335] • Modified with alkyltrichlorosilane cross-linking molecules for chemisorption on the hydroxylated/oxidized substrate. The distal benzenethiosulfonate groups are functionalised with thiolated probes [336]

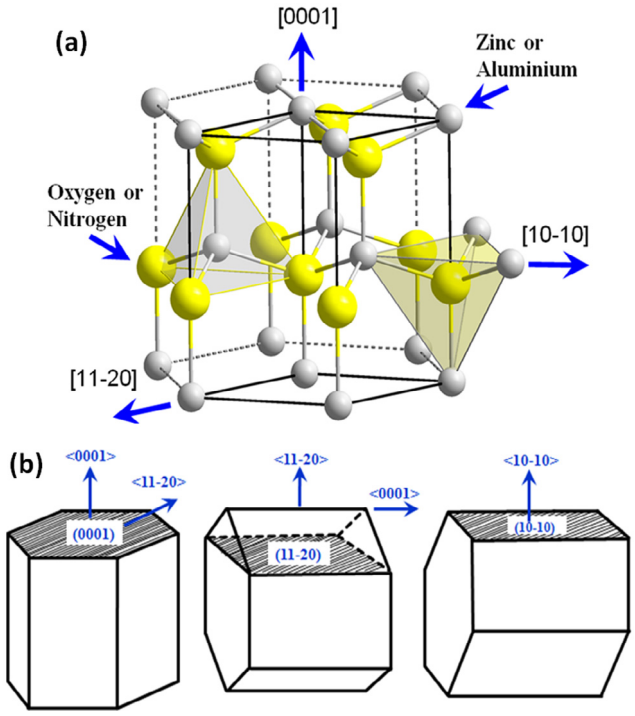

Fig. 8. (a) Illustration of wurtzite type crystal structures of ZnO and AlN including the three key directions; (b) preferred orientations along (0001), $(11\bar{2}0)$ and $(10\bar{1}0)$ planes of ZnO and AlN crystals on film surfaces.

densities of the three planes mentioned above are 0.099, 0.123, and 0.209 eV/Å^2, respectively [343]. The ZnO (0002) plane has the lowest surface free energy. If there is no epitaxial growth of the film on the substrate, and/or if the adatoms in the surface have enough energy to thermodynamically arrange themselves, the ZnO and AlN films will grow along the (0002) planes on many substrates such as silicon, quartz, glass, $LiNbO_3$, GaAs, GaN/Sapphire, and SiC [344–352]. However, as the film thickness increases, other film orientations could appear [353]. Without substrate rotation, the edge of the substrates, which is off from the plasma centre, commonly creates inclined angled columnar structures. Excess Zn (or Al) and O (or N) inside the ZnO (or AlN) films can cause the deterioration of the film (0002) crystallinity [354,355]. The O_2/Ar or N_2/Ar gas ratio and gas pressure also have significant effects on the film texture [356]. Fig. 8b illustrates film textures along the (0001), $(11\bar{2}0)$ and $(10\bar{1}0)$ planes of ZnO and AlN films [357].

Kajikawa reviewed the textural development of the ZnO films during deposition [358]. An amorphous ZnO intermediate or transitional layer generally forms before the film growth on substrates including Ni, Cu, Si, Ti, Ni and glass, and this layer is about 10 to 50 nm thick depending on the substrate used [359]. Fully crystalline ZnO films grow on this amorphous layer and their grain size increases with growth duration. The amorphous layer can result in ZnO films deposited on Ni, Cu, and Cr substrates with poor film textures. However, no such amorphous intermediate layer has been observed on Au, Ru, Pt, Al or sapphire substrates [360,361]. The ZnO films deposited on these substrates show a strong (0002) orientation. Buffer layers such as MgO, Al_2O_3, GaN, DLC, SiO_2, or metal layers such as Mo are frequently used to enhance the film crystallinity and texture (see Table 7) [362–368].

Epitaxial growth on a given substrate may lead to a film with a fixed orientation, and this can be achieved at high temperatures (sometimes over 1000 °C) using MBE or metal organic vapour phase epitaxy (MOVPE) [369–371]. The growth of ZnO and AlN films is attributed to the competition between the closest lattice mismatch between the ZnO (or AlN) growth plane and the substrate plane and the lowest surface free energy (0001) of ZnO (or AlN) [372–374]. Certain orientations in the substrates such as quartz, sapphire, $LiNbO_3$, $SrTiO_3$, diamond, MgO, CaF_2, GaAs, GaN, GaN/Sapphire, SiC and ZnO have been commonly used for epitaxial growth of ZnO and AlN films. Table 7 summarizes the substrates and lattice mismatches among different materials (intermediate layers or substrates), as well as the corresponding acoustic velocities and temperature expansion coefficients for both the ZnO and AlN films.

4.1.2. Film texture control and inclined angle growth

As mentioned in the Introduction, a liquid on the sensing surface of the device causes significant damping and attenuation of the propagating waves as the Rayleigh SAWs are coupled into the liquid. This damping problem can be solved by using a shear-horizontal SAW, which propagates with an in-plane shear horizontal motion [375,376], thus dramatically reducing

Table 7
A summary of acoustic velocity of the ZnO/AlN films on different substrates (most data is from SAW devices. The data is only for comparative purposes, as the velocity is related to the film thickness. Thus the comparison of velocities has no meaning unless the film thickness is identical).

Substrate/film materials	Substrate materials	Substrate structure	Lattice difference	Velocity (m/s)	Substrate thermal expansion coefficient (10^{-6} K^{-1})
ZnO	ZnO	HCP		2724	2.9 (4.751)
ZnO/Si	Si (1 1 1)	Cubic	41.3%	2653	3
ZnO/DLC	DLC	Amorphous		5000–7000	
ZnO/Nanocrystalline diamond				8500	1.18
ZnO/Diamond	Diamond (1 1 1)	Cubic		10,000–12,000	1.18
ZnO/AlN/diamond	ZnO/AlN/diamond			12,200	
ZnO/SiO_2	Quartz			4200	13.2 (a)/7.1c
ZnO/AlN	AlN	HCP	4.1%	4522	5.3 (4.1)
ZnO/Pt	Pt (1 1 1)	Cubic	1.8%	2684	8.8
ZnO/Au	Au (1 1 1)	Cubic	2.5%		14
ZnO/Sapphire	Al_2O_3 (0 0 0 1)	HCP	31.8%	4000–5750	7.3 (18.1)
ZnO/$LiNbO_3$	LiNbO3 (0 0 0 1)	HCP			14.8 (4.1)
ZnO/sapphire	Sapphire (0 0 0 1)	HCP	31.8%		8.4 (5.3)
ZnO/GaN	GaN	HCP	1.8%		3.17
AlN/Si	Si (1 1 1)	Cubic		5000–5050	3
AlN/Al	Al (0 0 1)	Cubic	23.15%		23.1
AlN/Pt	Pt (1 1 0)	Cubic	3%		8.8
AlN/Au	Au (1 1 1)	Cubic			14
AlN/W	W (1 1 0)				
AlN/Mo			0.87%		4.8
AlN/SiO_2	Quartz				13.2/7.1
AlN/Sapphire	Al_2O_3 (0 0 0 1)	HCP		6000	8.4 (5.3)
AlN/$LiNbO_3$	$LiNbO_3$ (0 0 0 1)	HCP			7.3 (18.1)
AlN/SiC	SiC (0 0 0 1)	HCP	31.8%	6500–7500	
AlN/GaN	GaN	HCP			
AlN/ZnO	ZnO (0 0 1)	HCP	4.1%		2.9 (4.751)
AlN/DLC	DLC	Amorphous			
AlN/Diamond	Diamond (1 1 1)	Cubic		10,000–12,000	1.18

SAW coupling into the liquid medium. To generate such a shear horizontal wave in the thin film acoustic wave devices, film textures such as $(10\bar{1}0)$ and $(11\bar{2}0)$ or along other axis (not the c-axis) of ZnO and AlN film are necessary [377–384].

Another good approach to solving the liquid sensing problem is to develop piezoelectric films where the c-axis of the film is inclined to the surface normal (as shown in Fig. 9a), thus allowing both longitudinal and shear wave modes to be generated on the same substrate [385,386]. These two modes have different propagating velocities and they resonate at different frequencies and can be individually controlled for either pumping or sensing purposes [387]. Inclined angled SAW and FBAR devices also show improved mass sensitivities under liquid conditions and improved operation using shear mode resonator [388,389]. Bjurstrom et al. [390] systematically studied the electromechanical coupling coefficients for both shear and longitudinal modes at different AlN inclined angles for FBAR devices. The k^2 value of the longitudinal mode has a maximum value for the c-axis AlN crystals ($\theta = 0°$), but gradually decreases with increasing angle as shown in Fig. 9b. In contrast, the k^2 value of the shear wave mode gradually increases with inclined angle increasing from 0 to a peak value at 45°. The k^2 value of the two modes reaches the same level at an angle of 30–35° as shown in Fig. 9b [391,392]. The pure thickness longitudinal mode for ZnO (or AlN) FBARs occurs at a c-axis tilt angle of 0° (0°) and 67.1° (65.4°), whereas pure thickness shear modes for ZnO (or AlN) occurs at 43° (46.1°) and 90° (90°) [393].

Tilted angle ZnO or AlN films can be prepared using oblique angle deposition (OAD, *i.e.*, tilting the substrate at an angle to the target during deposition) [395–400] or glancing angle deposition (GLAD) methods [401–403]. Inclined columnar or inclined crystalline structures can be formed by tilting the substrate at a large angle in the direction of the incident flux during the OAD process, and is attributed mainly to self-shadowing and ion bombardment mechanisms. GLAD is an extension to the OAD and substrate positions are precisely controlled (tilting/rotating at large titling angles) during deposition (generally from e-beam evaporation), which can easily result in the deposited films with a much larger inclined angle, nanopillars, zigzag, spiral or helical structures [404–407]. Readers may refer a recent review paper on this topic for more details [408].

For films made by inclined angle deposition, three different angles need to be especially addressed (see Fig. 9c):

(1) The substrate tilting angle or target tilting angle can be changed by experimental setting, and normally the tilting angles of the substrate can be changed from 0° to 90°, although above 80° the deposition rate is very low.
(2) The film columnar titling angle is the angle at which the columnar microstructures of the films grow, which is generally smaller than the substrate titled angle. For example, using an oblique angle of 85°, the columnar inclined angle was found to be only ~30–45° [409].
(3) The film crystal inclined angle corresponds to the crystal orientation, which is inclined to the (0 0 0 2) orientation, and the crystal inclined angle is smaller than the columnar titled angle, and much smaller than the substrate titling angle (see Fig. 9c).

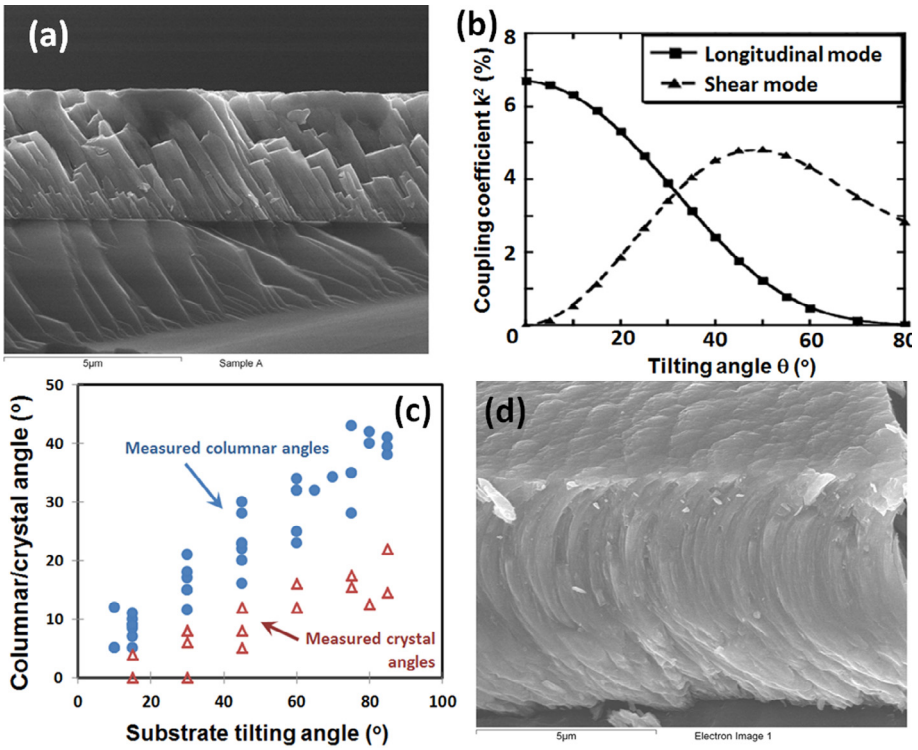

Fig. 9. Inclined angle piezoelectric films: (a) ZnO inclined film grown on silicon substrates; with a substrate tilting angle of 70° during deposition and a columnar tilting angle of 35° and crystal angles of 10–12°; (b) electromechanical coupling coefficient for both shear and longitudinal modes at different crystal tilting angles (modified from Ref. [394]); (c) three different types of angles for inclined angle deposition films: substrate tilting angle; columnar tilting angles; and crystal angles; (d) columnar angle of the inclined angled ZnO film gradually change to vertical growth during deposition with a substrate tilting angle of 60°.

At the initial growth stage of tilting-angle deposition, the growth along the substrate normal direction competes with the growth in the tilted c-axis direction. All deposition parametres influencing the surface mobility of adatoms will affect the inclined angles of the film growth [410]. In most cases, even though the films show inclined or tilted columnar structures, the crystal orientations of the ZnO or Al films are actually still c-axis, i.e., along (0002) orientation. The film crystal orientation angles need to be determined using characterisation techniques such as pole figures or rocking curves from X-ray diffraction (XRD). Taking Al doped ZnO films as an example. A substrate incident angle of 40° results in a crystal angle of only 14°. If the substrate incident angles are 60° and 80°, the (0002) crystal inclined angles become 25° and 35° respectively [411]. The columnar angle of AlN films with an incident flux angle of ~40° and 55° have been reported to be 23° and 32°, respectively [412]. Fig. 9c provides a comparison of the three different angles based on the measurement results from the inclined angled ZnO films.

Frequently, columnar angles of the inclined film have been observed to gradually change to vertical growth during deposition as shown in Fig. 9d [413,414]. These phenomena can be explained by the minor changes in the deposition conditions which could change the mobility of deposited species. Hence, adatom mobility determines the tilting columnar angle or inclined crystal angle.

Large tilted angle deposition results in porous structures and decreased deposition rates. Due to the formation of porous structures, the shear acoustic wave velocity decreases with increasing angles of inclination. This relationship is more significant for films with larger tilted angles. A good uniformity is hard to achieve in film thickness and columnar inclined angles over large areas [415]. In order to solve the issue of poor thickness uniformity, zig-zag and spiral patterns were prepared by changing the tilting angles or by rotating the substrate during tilted angle deposition [416–418]. Acoustic wave devices using the zig-zag layered patterns showed a higher frequency and higher sensitivity than those with a single layer [419,420]. Nano-columnar or nanorods structures are normally formed when the titling angle is above 80°. However, these nanostructures are porous and discrete, which may not be suitable for the piezoelectric layer in acoustic wave devices, but may be useful for sensing layers.

The sputtering target is normally placed close to the substrate during deposition. At the substrate surface, the ions in the sputtering process have various directions due to the wide angular distribution and scattering from the working gas. Positioning the substrates far away from the targets can produce apparently more clearly inclined angle films [421]. A long

rectangular shape target will produce a longer range of uniform tilted angle films, whereas a circular shaped target would probably produce a ring distribution of inclined angles.

E-beam evaporation is considered as a better method to achieve uniform inclined angled columnar or spiral structures, because of (1) the controlled directionality of the evaporated flux; (2) the large distance between source and substrates, and (3) low gas pressure. Apart from the substrate tilting angle, plasma or e-beam power, gas pressure, external ion sources and shields of plasma will all influence the kinetic energies of the atoms arriving at the substrate surface, causing different tilt angles [422,423].

During the deposition of ZnO and AlN films, the film texture can be changed from (0002) into $(10\bar{1}0)$ or $(11\bar{2}0)$ by using a directional oxygen or nitrogen ion beam placed at an angle to the substrate surface, which is mainly due to ion channelling effects [424,425]. The films with the $(10\bar{1}0)$ or $(11\bar{2}0)$ textures can excite a pure shear acoustic wave. A low chamber pressure is required to generate significant oxygen ion bombardment effect in order to provide a longer mean free path for the oxygen ions.

In summary, the following methods can be employed to obtain film texture other than the c-axis (0002) type:

(1) Epitaxial growth on a specific substrate using a suitable deposition method, such as MBE.
(2) Control of the sample position, tilting the substrates under the plasma, or locating samples in off-centre positions [426].
(3) Use of an additional anode (or electric field) near the substrate, which can have an apparent orientation effect on the growing films [427].
(4) Use of an external oxygen or nitrogen ion source and control of the oxygen ion bombardment during film growth.
(5) Use of a shutter or blind which can be positioned between the target and substrate to only allow oblique particles arriving on the substrate surface [428].
(6) Pre-depositing a seed layer with inclined angle to promote the inclined growth of top film layer [429].

4.2. Doping of ZnO and AlN films for device performance enhancement

Doping and alloying have been used to modify the material properties of ZnO or AlN such as their energy band gap, refractive index, transmission/absorption, conductivity and dielectric properties [430,431]. Recently, doping and alloying have been utilized to alter the piezoelectric and ferroelectric properties of ZnO and AlN films, and enhance their piezoelectric coefficients and electromechanical coupling coefficients.

4.2.1. Doping of ZnO films

Doping ZnO films with various elements is a routine process to enhance their conductivity [432,433]. Group V elements N, P, As, Sb can be added to ZnO films to form p-type ZnO [434,435]. For example, low nitrogen doped ZnO piezoelectric thin films have been used for FBAR device applications [436]. A ZnO film becomes n-type through doping with group III and IV elements such as Al, Ga, In, Sn and Si. Al doped ZnO (AZO) has been successfully applied as transparent electrode on a ZnO/-glass transparent SAW device [437].

Doping the ZnO films with group I elements such as Li, Na, K increases the film resistivity and piezoelectricity [438,439], and improves film crystallinity and (0002) orientation [440]. Moderately doped ZnO with Cu (a few atomic percentages) can enhance the c-axis orientation, and increase its electrical resistivity up to $10^9\ \Omega$ cm as well as its piezoelectric coefficient d_{33} [441–444]. Doping ZnO with transition-metal elements (e.g. Mn, Fe, V, Cr) has also been reported to improve the piezoelectric and paramagnetic properties [445] and resistivity for acoustic wave device applications [446,447]. For example, the piezoelectric properties of ZnO were reported to be improved by tuning the Mn composition in the ZnO film [448–450], being able to increase the d_{33} value from 12.1 pC/N for the pure ZnO to 86 pC/N for the ZnO films doped with 8% Mn. Mn-doped-ZnO/SiO_2/Si SAW devices have shown excellent performance for glucose sensing [418].

An enhancement of the piezoelectric coefficient has also been obtained from ZnO doped with vanadium (V) [451]. The d_{33} values increased with the V content, reaching a value of 110 pC/N (accompanied by a high resistivity in the order of $10^{13}\ \Omega$ cm when 2.5% of V was incorporated into ZnO), which is an order of magnitude higher than that of undoped ZnO. This has been attributed mainly to the switchable spontaneous polarization induced by V dopants.

Furthermore, Ca and Sr have been used to dope ZnO films deposited on quartz substrates to form a Love wave mode SAW device [452], showing an improved sensitivity for biosensing. On the other hand, Co, Ni and Fe doped ZnO films showed enhanced c-axis orientation and crystallization. However, the piezoelectric coefficient of the ZnO doped with these elements became smaller compared with that of the pure ZnO. Ti and Cr doped ZnO films, showing decreased resistivity due to a significant narrowing effect of the energy band gaps [453,454]. Thus, doping with these elements is more suitable for modification of the electrical and optical properties, rather than for piezoelectric applications. $Mg_xZn_{1-x}O$ ($x \leq 35$) has also been considered to be a new piezoelectric material for SAW and BAW devices. Through controlling the Mg composition, or using ZnO/$Mg_xZn_{1-x}O$ multilayer structures, one can tailor the SAW properties.

However, we note that the enhanced piezoelectric coefficients of most of the above mentioned doped films were measured using piezoelectric force microscopy, and their performance after integrating into various acoustic wave devices is yet to be confirmed.

4.2.2. Doping of AlN films

Similarly, many elements have been used to dope AlN film to modify its piezoelectricity. For example, Akiyama et al. discovered that the piezoelectricity of $Al_{1-x}Sc_xN$ alloys increases with the Sc content, showing a maximum increase of 400% in d_{33} at x = 0.43 compared to that of the pure AlN [455,456]. This value is the largest piezoelectric constant among the known tetrahedrally bonded semiconductors. Since then, AlN films with Sc-doping have been intensively studied [457–459]. Density functional theory (DFT) was applied to study the origin of this enhancement of the piezoelectric coefficient [460], and results showed that doping AlN with Sc leads to softening of the wurtzite phase. The increase of Sc concentration in the wurtzite phase causes ionic displacements, leading to larger dielectric and piezoelectric responses. The transverse piezoelectric coefficient e_{31} of $Al_{1-x}Sc_xN$ thin films was also found to be affected by Sc doping [461]. This coefficient was increased by about 50% when the Sc concentration was increased from $x = 0$ to $x = 0.17$ [462]. Recently, a ScAlN/diamond layered structure was fabricated, and the theoretical maximum k^2 value of 14.5% was obtained for a SAW device operating in the 2–3 GHz range [463].

However, incorporating Sc in AlN often leads to a non-uniform distribution of Sc in the alloy, possibly due to the preferential phase separation of the ScN rocksalt and AlN wurtzite crystals. This non-uniformity can result in large variations in localized stress and piezoelectric coefficients within a wafer, or from wafer to wafer. However, owing to the significant enhancement of the piezoelectric properties, $Al_{1-x}Sc_xN$ materials with different Sc contents have been utilized to fabricate various piezoelectric devices, including SAW [464], FBAR [465] and Lamb wave resonators. For the ScAlN SAW device fabricated on a 6H-SiC substrate, the Sezawa mode wave showed a higher coupling coefficient, a higher frequency and a higher phase velocity than those of the Rayleigh waves [466]. A ScAlN film with a c-axis tilt up to 5.5° was deposited on sapphire and the wave propagation direction and tilt angle both influenced the performance of the SAW devices [467].

One of the most important features of the AlN is its high melting temperature and consequently the potential for high temperature acoustic wave sensing devices. Wurtzite type BN is another high temperature piezoelectric material, but is metastable. Therefore, sputtered AlBN films have been investigated for high temperature acoustic wave sensing applications, with higher acoustic velocities, higher Young's modulus and piezoelectric coefficient compared to those of AlN films [468–470].

Ga doped AlN films possess high acoustic velocities and coupling coefficients, and are suitable for high-frequency SAW and BAW devices in wireless communication systems. Doping AlN films with Y [471,472], Cr [473], Ta [474] and Er [475] improved the values of d_{33}, but a deterioration in the values of d_{33} was found with Ti doped AlN. These studies clearly indicate that the ionic radius of the dopant is the critical parameter for the enhanced piezoelectric properties of the doped AlN films.

Recently co-doping multiple elements into AlN films have been frequently reported. For example, Mg and Zr co-doped AlN thin films showed a linear improvement of d_{33} value with an increase of the ratio of Mg—Zr to Al up to 0.5, and a d_{33} value of ~15 pC/N was obtained compared to 5.5 pC/N for pure AlN. These co-doped AlN films were used for high frequency FBAR applications [476]. Through first principle calculation, co-doping with two or more elements with different valence cations can be designed and their piezoelectricity properties have been assessed, for example, $(\alpha_y,\beta_{1-y})_xAl_{1-x}N$ (with (α and β are elements of Ti, Zr, Mg, H_f and Si, etc.), and the ionic radii of the dopant elements were identified as the key to improve the piezoelectric properties of the co-doped AlN [477]. Co-doped $(Mg, M)_xAl_{1-x}N$ (M = Zr or Hf) thin films showed a higher d_{33} value. FBARs employing $(Mg, Zr)_{0.13}Al_{0.87}N$ and $(Mg, Hf)_{0.13}Al_{0.87}N$ films showed an increase of electromechanical coupling coefficient from 7.1% for pure AlN to 8.5% for Mg-Zr-doped AlN and 10.0% for Mg-Hf-doped AlN [478]. MgZrAlN and MgHfAlN films were used as the piezoelectric active layers in an air-bag type sensor, demonstrating their potential for wideband and high frequency FBAR applications [479].

Although doping or alloying of AlN and ZnO films has been used to synthesize materials with better piezoelectric properties for acoustic device application, the current research approach is largely based on "trial and error" methods without well-defined guidelines from theoretical analysis and material modelling. This is particularly true for the ZnO as there are not many reports on the DFT based studies for doping in ZnO. Only a few research groups reported DFT-based modelling for the AlN films [480]. Therefore it is necessary to conduct a systematic investigation using the DFT for doping and alloying of ZnO and AlN, to provide robust guidelines for the "doping" strategies.

4.3. Film thickness/dispersion effects

Thin film acoustic wave devices have significant dispersion effects, *i.e.*, the acoustic wave velocity, resonant frequency, electro-mechanical coupling coefficient and quality factors, all depend significantly on the piezoelectric film thickness [481]. Hence, the effects of film thickness on wave propagation properties have been extensively investigated for SAWs, FBARs and Lamb wave devices, and these are now discussed.

4.3.1. SAW dispersive effects

For thin film SAW devices, the ratio between the wavelength and the film thickness (or more precisely, the normalized film thickness *hk*, where *h* is film thickness and *k* is wave vector, $k = 2\pi/\lambda$) is a critical parameter which determines the wave modes and their velocities as shown in Fig. 10a. If the piezoelectric film is relatively thick, or if the film thickness is larger than or comparable to wavelength of the SAW, the waves will mainly propagate inside the film layer. Thus, the acoustic velocity will approach that of Rayleigh waves for thin film materials (about 2800 m/s for ZnO and 5600 m/s for AlN). The

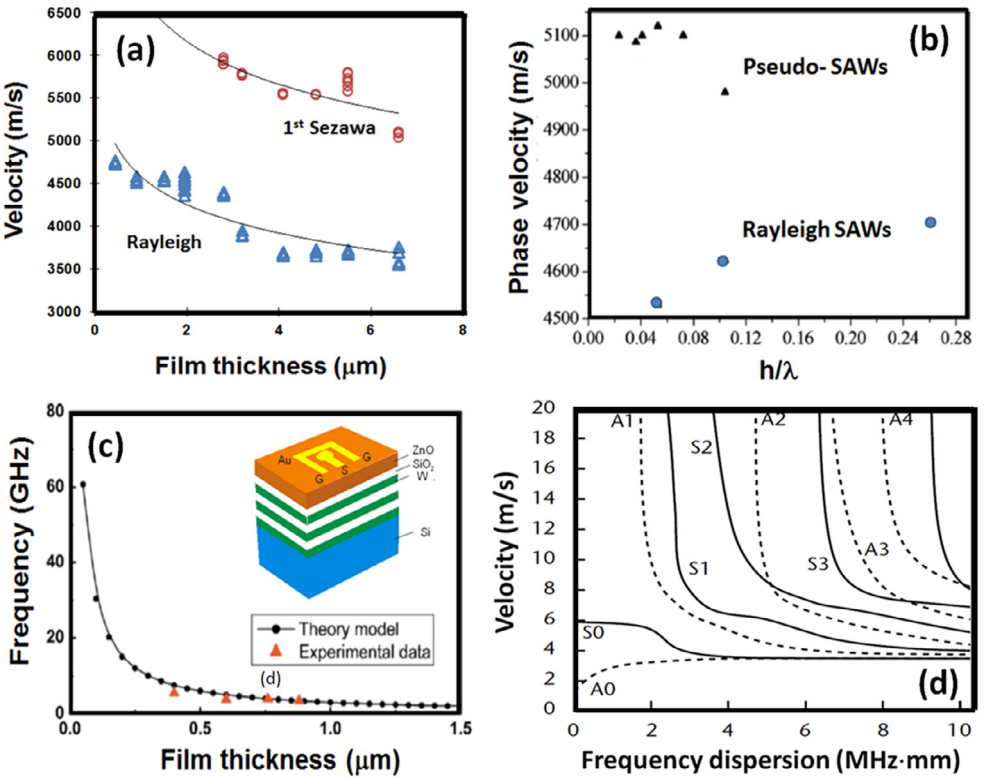

Fig. 10. Dispersive effects for thin film acoustic wave devices. (a and b) Phase velocities of ZnO and AlN films as a function of thickness/wavelength ratio for different acoustic wave modes, (b) is modified from [486]; (c) resonant frequency of ZnO FBAR devices as a function of film thickness (modified from [487]); (d) frequency dispersion effects of Lamb waves, showing the fundamental and higher harmonic A mode and S mode Lamb waves.

SAW energy is largely dissipated in the substrate if the film thickness is much less than one wavelength. Consequently, the wave velocity of the SAW approaches the Rayleigh velocity of the substrate material (for example, Si in Fig. 10a). Therefore, changing the ratio between film thickness and SAW wavelength can tune the phase velocity of the SAW devices between the acoustic velocities of the thin film and the substrate material as shown in Fig. 10a.

Depending on the different wave propagating velocities of film and substrates, dispersion effects can be totally different. For instance, the frequency and velocities on ZnO/Si decrease with increasing normalized film thickness as shown in Fig. 10a. This behaviour is opposite to that observed with AlN/Si SAW devices, where the velocities increase significantly with thicker AlN films as shown in Fig. 10b [482]. However, there is a minimum cut-off film thickness on the order of tens of nanometres (or less than ~10% of the wavelength). Below this cut-off thickness, no significant SAWs can be generated, due to the limited piezoelectric effect for SAW generation and the low electromechanical coupling coefficient for a very thin piezoelectric film.

Another dispersive phenomenon is that higher modes of the SAWs can be generated with increasing film thickness, *i.e.*, 1st and higher Sezawa mode waves can be detected. As explained previously, the Sezawa modes can be realised from a layered structure, where the substrate (or sub-layer below the film) has a higher acoustic velocity than that of the top film [483]. These Sezawa waves exhibit larger phase velocities and higher resonant frequencies than those of Rayleigh waves for a given thickness (Fig. 10a), and are thus suitable for high-frequency applications [484,485].

However, the dispersion effects and higher modes become complicated with multi-layered acoustic wave device designs, as each single layer and its variation in thickness and material properties will change the wave propagation properties, for example, resulting in pseudo-waves (or thin film based bulk wave modes) [488–491].

4.3.2. FBAR dispersive effects

The resonant frequency of the FBAR devices depends significantly on the thickness and the material type of the piezoelectric layer. With a decrease in piezoelectric film thickness, the resonant frequency increases significantly, especially when the film thickness is less than few hundreds nanometres, as shown in Fig. 10c [492,493]. This is mainly due to shorter transmission paths for bulk acoustic waves in the thinner layer.

However, there is a practical limit on the minimum thickness of piezoelectric layer, or the best thickness range, for both ZnO and AlN FBAR devices. A thin film of less than tens of nanometres leads to dramatic changes of the frequency and a significant decrease of the peak intensity. Both the electromechanical coupling coefficient (k^2) and the quality factor (Q value) of the FBAR devices significantly decrease with reducing film thickness to tens of nanometres. On the other hand, for a thick

film, the propagation/transmission path will be increased, thus reducing the resonant frequency. The surface roughness tends to increase with increasing film thickness and grain size, thus leading to an increased acoustic wave loss and dispersion. Surface roughness has a detrimental effect on the resonant frequency and quality factor of the FBARs as a rougher surface makes surface scattering stronger. Therefore the requirement for precise control of the thickness uniformity and smoothness of the piezoelectric layers is strict for high frequency FBARs. Similarly, the resonant frequency of the FBAR devices decreases with increasing thickness of the intermediate layer or supporting sub-layer due to the mass loading effect and increase of propagation route through the thickness direction [494].

4.3.3. Lamb wave and Love wave dispersive effects

Lamb waves have significant dispersion effects as a function of thickness of substrate membrane. The frequencies of the Lamb waves (including fundamental and higher A modes and S modes) are sensitive to the thicknesses of the thin plate or membrane structures as shown in Fig. 10d. The thickness of the top piezoelectric film has a relatively smaller influence compared with that of the membrane/plate layer because of its thin nature.

SAW devices of ZnO/SiO_2/Si and ZnO/AlN/Si have been commonly regarded as Love mode devices. Both the thicknesses of the ZnO film and interlayers, such as SiO_2, or AlN, have significant influences on the phase velocities, frequencies and electromechanical coupling coefficients, which have been discussed in Section 2.5.

4.4. Engineering film stress

4.4.1. Film stress effect and its dominant factors

As-deposited sputtered ZnO or AlN films generally have large compressive or tensile stresses, which are a combination of intrinsic, extrinsic and thermal stresses. The intrinsic stress is caused by a combination of defects in the films (voids, dislocations, impurities, grain boundaries), the interfacial structures of film/substrate (differences in lattice mismatch), and/or ion/electron bombardment/impinging during sputtering and recrystallization [495]. For multilayer SAW or FBAR structures, intrinsic stresses are also caused by lattice constant mismatches of the various layers of materials with different lattice structures, and these are generally called epitaxial stress. Once the thickness of the film exceeds a critical value the intrinsic stress is reduced due to structural relaxation.

Extrinsic film stress is induced by external factors, resulting from interactions between deposited material and the environment. These factors are mainly related to film process parametres such as temperature, pressure, partial pressure of gases, power and bias voltage, which are important elements in the development of film stress. The magnitudes and signs (tensile or compressive) of the film stress are highly dependent on the deposition technique.

Generally a lower gas pressure will result in a large compressive stress, due to the long mean free path during which ions and radicals receive more energy from the electric field. The high energy bombardment and the formation of a dense film structure lead to a large compressive stress [496]. High deposition pressure has the opposite effects on the film, *i.e.* the formation of tensile stress which is due to the formation of a more porous film structure. Higher O_2 or N_2 chamber pressure or excess oxygen inside the deposited ZnO films will deleteriously affect the crystal quality and increase the surface roughness, also changing the film stress [497].

Deposition at elevated temperatures can be employed to reduce the film intrinsic stress as atoms/ions have high migration rates at high temperatures [498]. High deposition temperature may also reduce defects significantly, leading to a reduced intrinsic stress in the film, although this may make the thermal stress component more significant [499]. Post-deposition thermal annealing is frequently used to reduce both the film stress and defect density, and improve the crystal quality, which in turn benefits the device performance [500–506].

External bombardment with atoms, ions or electrons during the sputtering process has a significant effect on the development of the compressive stress [507,508]. During ZnO and AlN film growth, a positive bias increases the kinetic energies of oxygen or nitrogen ions, and enhances the mobilities of adatoms arriving onto the film surface, causing significant surface disruption, large compressive stress and roughness. A negative bias will have less bombardment effect but still provide sufficient mobility of adatoms arriving at the film surface. In order to avoid the high energy bombardment by ions and radicals during film deposition, deposition systems such as the HiTUS have been developed. As described in Section 3.1, a high density plasma is generated by a high RF power and is delivered onto the substrate in another chamber using an electromagnetic field. In this way, a high density plasma can be generated for film deposition, but the energy of ions and radicals of the elements can be significantly reduced, leading to thin films with high deposition rates and extremely low stress on the order of a few tens of MPa.

Film stress generally depends on the film thickness, and initially increases with thickness. It reaches a maximum value and then decreases when the film thickness increases further, mostly due to the relaxation of the intrinsic stress once it exceeds a critical value. This critical thickness is determined by the evolution of lattice mismatch between film and substrate, porosity/density, stiffness, which are all linked closely with deposition parametres.

Stress is more serious for sputtered AlN films, which generally have much larger film stresses compared to ZnO thin films [509]. Films of AlN often show delamination/cracking and significant warping of coated structures [510–515]. Large film stress can induce changes in the mechanical, thermal and piezoelectric properties of the different layers, thus changing the elastic constants of thin films and deformation of the structures. This phenomenon is generally called the acoustoelectric (AE) effect [516]. Large film stress changes both the mechanical and electrical properties of films, leading to a long term

instability and unreliability of the acoustic wave devices. The AE effect in the tensile stress condition is of more concern than that in compressive stress, as compressive stress can help to mitigate crack propagation [517–519]. The AE effect can be more significant for the Sezawa mode waves than for the Rayleigh ones, because the wave is more concentrated in the film/-substrate interface and has a more significant longitudinal motion.

The piezoelectric and dielectric characteristics of the ZnO and AlN films can be altered by large film stresses. Electromechanical coupling coefficients have been observed to decrease with increasing tensile stress [520]. Lappalainen et al. [521] showed that an increase in residual stress is linked to a reduction in dielectric material properties. For the FBARs and Lamb wave devices, the film stress is more critical, as they generally have thin membrane multilayer structures and are prone to bending or buckling when over-stressed. For FBARs with a back-trench structure or air bag structure, large stress levels can cause cracking or breaking of the membrane, leading to an early failure of the FBARs and low device yields.

Inclined angle deposited films, including spiral or zig-zag with tilted columnar structures generally show much lower film stress due to their relatively porous structures. The film stress can be decreased significantly at a larger columnar tilting angle [522]. Therefore, depositing a thin layer of inclined-angled AlN layer followed by the standard deposition process is a good way to reduce the film stress in the later vertical film growth stage of a thick AlN film.

4.4.2. Film stress measurement

Film stresses can be measured using a number of different methods. One of the most commonly used ones is the beam/-cantilever/wafer bending-curvature method based on Stoney's equation [523],

$$\sigma = \frac{1}{6}\frac{E_s t_s^2}{t_f(1-\nu_s)}\left(\frac{1}{R_2}-\frac{1}{R_1}\right) \tag{26}$$

where E_s is the elastic modulus, ν_s is the Poisson's ratio, t_s and t_f are the substrate and film thicknesses and R_1 and R_2 are the initial and final radii of curvature of the substrate, before and after the deposition. This well-known equation is valid only in the thin film regime when $t_s \gg t_f$.

XRD analysis and Raman spectroscopy analysis have also often been used to estimate the film stress. For example, based on XRD analysis, the stress can be calculated using Hoffman's equation [524,525]:

$$\sigma_f = \left[2C_{13} - \frac{C_{33}(C_{11}+C_{12})}{C_{13}}\right]\left[\frac{C-C_o}{C_o}\right] \tag{27}$$

where C and C_o are the lattice constant of the film under stress free conditions. The constant C_o can be obtained from the JSPDS card of films. The constant C_{ij} are the elastic lattice constants in different directions. Taking ZnO as an example, C_{11} is 209.7 GPa, C_{12} = 121.1 GPa, C_{33} = 210.9 GPa, and C_{13} = 105.1 GPa, and C_0 is 0.5205.

Thin film stress can also be calculated from the XRD measured peak angles:

$$\sigma_f = \frac{E_{\mathrm{ZnO}}}{(1+\nu_{\mathrm{ZnO}})}\frac{\Delta 2\theta}{2\tan\theta_o} \tag{28}$$

where θ and θ_o are the peak angles. E_{ZnO} and ν_{ZnO} are the modulus and Poisson ratio of the ZnO films. The residual stress σ_φ in the thin film along the φ direction can also be obtained using a plot of 2θ vs. $\sin^2\psi$ by measuring the changes of 2θ values at different incident angles of ψ [526]

$$\sigma_\varphi = -\frac{E}{2(1+\nu)}\cot\theta_o\frac{\pi}{180}\frac{\partial(2\theta)}{\partial(\sin^2\varphi)} \tag{29}$$

where θ_0 is the Bragg's angle for diffraction peaks in the samples without residual stress and θ_ψ is the Bragg's angle at diffraction peaks in the samples with residual stress, E is Young's modulus and ν is the Poisson's ratio for the thin film. Much research has shown that the relationship between 2θ and $\sin^2\psi$ is linear.

It is worthy pointing out that the stress values obtained by XRD method are frequently different from those obtained from the bending-curvature method. The possible reason is that the XRD method measures the stress of a localized small area, whereas the bending-curvature method obtains the average stress of the whole structure or wafer, in which stress relaxation across the substrate may occur. Distributed impurities and structural defects may also contribute to this discrepancy.

The thermal stress of a two-layer system, σ_{th}, can be calculated using:

$$\sigma_{th} = \frac{1}{d_A}\left[\frac{1-\gamma_A}{d_A E_A}+\frac{1-\gamma_B}{d_B E_B}\right]^{-1}\int_{T_o}^{T_1}(\alpha_B(T)-\alpha_A(T))dT \tag{30}$$

where A and B refer to two layers, γ is the Poisson ratio, d is thickness, E is thickness, α is the TCE value. Once the thermal stress is obtained, the intrinsic stress, σ_{intrin}, can be calculated based on the following equations, thus it can be used to link with the film microstructural changes:

$$\sigma_{intrin} = \sigma_{total} - \sigma_{th} \tag{31}$$

5. Engineering electrode materials and patterns

5.1. Electrode materials

Apart from piezoelectric film material quality, the electromechanical coupling coefficient of acoustic wave devices is also dependent on the type of electrode materials, patterns and dimensions of the electrodes [527–529]. This element is more critical for FBAR or SMR devices as the piezoelectric films are normally grown on the bottom electrode of the devices, which can influence the crystallinity and orientation of the piezoelectric films. Therefore, the selection of electrode materials for the FBARs is extremely critical.

For sensing applications, the electrodes should have a low mass to minimise wave damping, and should have a high acoustic impedance to confine the acoustic waves within the piezoelectric layer, and also have a high conductivity in order to minimise the series resistance in the transmission of the excitation signal. Therefore, electrode materials with high acoustic impedances ($Z = \rho \cdot v$, in which ρ and v are the density of material and velocity of the waves) are the best choices as they can be used to increase the Q factor and resonant frequency, simultaneously. The acoustic impedance of electrode materials is critical for acoustic wave device applications, along with their chemical/thermal stabilities, stress and adhesion to the substrate. Electrodes with a large acoustic impedance help to confine the acoustic energy within the piezoelectric layer, leading to a higher coupling coefficient. However, a thick electrode may cause a mass-damping (loading) effect. Table 8 lists the key properties of commonly used electrode materials. In this paper, we used a new acoustic performance parameter, $X = Z/\xi$, to compare the different electrode materials, in which ξ is resistivity of the materials. Fig. 11 presents the acoustic impedance as a function of density for a range of electrode materials, with AlN and ZnO as references.

For acoustic wave devices, the most frequently used electrode materials are Al and Au/Cr (or Au/Ti). Generally, at a relatively low frequency below GHz, an Al electrode has a low resistivity and low acoustic impedance, as well as a high Q factor, thus it is often used for delay lines and transversal filters. However, due to their low mechanical strength, low melting points and poor electro-corrosion resistance, the lifetime of the Al electrodes is a major concern. Au electrodes on the other hand are often used for resonators and filters. At a high frequency on the order of several GHz, aluminium electrodes can provide high reflection coefficients and a high Q factor. However gold electrodes can have large mechanical losses, relatively large mass loading and reflection and thus may not be suitable for high frequency applications [530].

The other commonly used electrode materials for acoustic wave devices include Mo, W, Ta, Ir, Pt, Ni, Ru, etc. (see Table 8) [531–533]. Both Mo and W have large acoustic impedance, low acoustic attenuation and high Q factors and thus can potentially produce high effective coupling coefficients. Therefore, Mo and W are among the most reported electrodes in FBARs and AlN based acoustic wave devices [534–537]. Pt has good chemical and thermal stabilities as well as a good high-temperature performance. Other metals such as Hf, Ag, Ti, Co, Cr, Cu, Fe, Nb, Zn and Zr have been reported as electrode materials for acoustic wave devices [538], but all have various problems, such as high resistivity (Hf, Cr, Ti), poor corrosion resistance (Ag, Zn, Fe), poor adhesion and large stress (Co). For high temperature acoustic wave devices, Pt, Ti/Pt, Pt/Rh, Pd and Ir have frequently been used [539].

Table 8
Key properties of commonly used electrode materials.

	Resistivity, ξ, 10^{-8} O m	Phase velocity (longitudinal and shear, m/s)	Poisson ratio	Density (10^3 kg/m^3)	Young's Modulus (GPa)	Acoustic impedance, Z (10^6 kg/m^2 s)	Acoustic performance: X = Z/ξ (10^{14} kg/m^3 s ohm)
Al	2.82	6350–6500 (3040–3120)	0.33	2.695	76	17.65	6.26
Au	2.44	2650–3210 (1200)	0.42	19.32	78	51.20	20.98
Mo	5.3	6290–6700 (3400)	0.307	10.28	230	63.74	12.03
Pt	10.5	3260 (1730)	0.38	21.14	170	63.42	6.04
Cu	1.7	5010–5200 (2270)	0.355	8.96	128	44.89	26.41
Ir	4.7	5350–5560	0.21	22.3	525	118.19	25.15
Ag	1.59	3600 (1600)	0.37	10.6	100	38.16	24.00
Ru	7.1	1260	0.3	12.2	220	27.57	3.88
W	5.6	5200–5500 (2900)	0.28	19.25	410	92.40	16.50
Ni	6.99	5600 (3000)	0.31	8.84	200	44.20	6.32
Ti	42	6100 (3100)	0.32	4.48	110	27.33	0.65
Hf	33	3010	0.37	13.3	110	40.03	1.21
Ta	13.2	4100 (2900)	0.34	16.6	200	68.06	5.16
Cr	12.5	6650 (4030)	0.21	7.19	140	46.74	3.74
ZnO		6340 (2720)	0.36	5.68	210.9	36.01	
SiO_2		5760	0.17	2.2	74	12.67	
Al_2O_3		11,100 (6040)	0.23–0.30	3.99	350	44.29	
Si_3N_4		11,000 (6250)		3.27	250	36.30	
AlN		12,000 (6000)	0.22–0.29	3.27	300–350	39.24	
CNT	1.5		0.22	1.5	1300	57.20	38.13

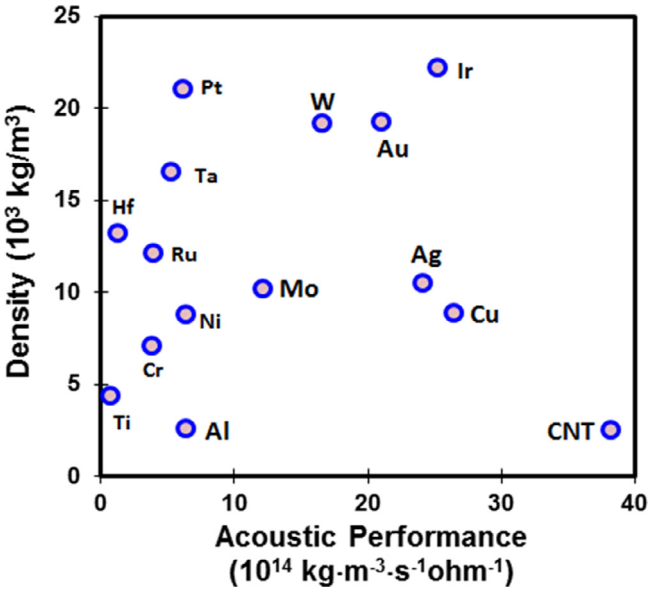

Fig. 11. Relationship between density and acoustic performance of commonly used electrode metals. The best material would be located at the top-left corner, with low mass and high acoustic impedance and low resistivity.

In FBAR devices, the bottom metal layer significantly affects the texture of the piezoelectric films and hence its electro-acoustic properties [540]. ZnO or AlN films deposited on electrode materials with a face centred cubic (FCC) lattice structure show a good c-axis orientation, especially for Au, Al, Mo, or Pt contacts. A better quality of c-axis grown ZnO or AlN films can also be obtained by depositing films onto metals with a hexagonal structure such as Ti and Ru [541–544], or body centred cubic (BCC) structures of Mo or W [545–548]. Some conducting and transparent oxides, such as AZO and ITO, have also been applied as electrode materials for transparent SAW or FBAR devices [549].

The electrodes define the resonant area of the FBARs, and if properly designed they can efficiently restrict the acoustic energy, thus minimizing mass loading and signal losses and maximizing the Q-factor. Carbon nanotubes (CNTs) possess low densities in the range of 1–2 g cm^{-3}, high acoustic impedance of ~78 Mrayl, electrical conductivities of up to 10^6 S m^{-1}, and exceptionally high elastic moduli, and thus a high acoustic impedance [550,551]. Another advantages of using the CNTs as the top electrode for acoustic wave biosensors is that the CNTs can be used as both electrodes and a sensing layer with a extremely large surface area [552], which can be further functionalised for enhancing the sensitivity of biosensing [553]. Using the CNTs as the top electrode material for FBARs led to a Q-factor of over 2000, i.e., a 5-fold improvement [554]. The FBARs with a CNT electrode showed an improved sensitivity compared to that with Au electrodes, with a mass detection limit of 10^{-13} g and a potential for reducing this to 10^{-15} g.

Similarly, graphene [555,556] also makes a good electrode material, because of its theoretically high conductivity and being an extremely thin and light material which would cause insignificant mass loading [557]. SAW devices with graphene IDTs exhibit well define resonant peaks and signal amplitudes [558,559]. Multilayer graphene with a sheet resistance of a few tens of Ω/sq could improve the transmission properties. However, this hypothesis is yet to be tested in actual biosensing applications. It should be noted that the theoretical mechanical and tribological properties of a single atomic graphene layer structure might not be as good in practical applications.

5.2. Engineering electrode designs

Different designs of electrode patterns for acoustic wave devices have been investigated mainly for communication or RF filters applications. A number of papers have reported on the design and patterning of different electrodes to enhance the sensing performance, and more importantly, to improve microfluidic functions [560,561]. Most of these current electrode designs are applied in devices made on bulk materials, such as quartz or $LiNbO_3$. Considering SAW reflection properties, the four basic mechanisms are mass loading, piezoelectric shorting, electrical regeneration and geometric discontinuity. The importance of these four depends on the substrate and electrode properties, such as the strength of the electromechanical constant and the metallization patterns [562,563]. Due to the isotropic nature of thin film materials deposited onto a planar substrate, flexible designs of electrodes or IDTs, such as focused, curved, circular/annular, or randomly shaped patterns are readily achievable on thin film acoustic wave devices, without needing to take account of the differences in wave velocities in various crystal-cut directions, These are, however, essential when designing IDT layouts on the bulk piezoelectric materials [564]. This flexibility is a key advantage associated with thin film based devices. For example, using the thin

Table 9
Various types of interdigitated transducer (IDT) designs for SAWs and Lamb waves, and electrodes for FBARs [574–581].

Mode	Name	Illustration	Advantages	Problems	Applications
SAW and Lamb Wave	Standard bidirectional IDTs		Simple design	Internal mechanical edge reflections, Loss of wave energy at two sides with half the energy wasted	General usage
	Split IDTs,		Reflect back some of the waves, thus reduce reflections. Operation at third harmonic is possible allowing higher frequency for a given minimum fabrication electrode width. Another design is meander line, or single-meander-single design, with all gaps and fingers at 3λ/8, which will generate a third harmonic response stronger than its fundamental response	Not so effective in reduction of reflections	General usage
	Single phase unidirectional transducer (SPUDTs)		Reflect back or cancel regenerated waves using the internally tuned reflectors within the IDT to form a unidirectional SAW propagation from one side of the IDT. Can eliminate triple transition effect Low insertion loss	Reduction in total SAW energy, SAW generation efficiency is not good	Essential for SAW microfluidics and sensors as it not only improves the performance, but maintains the SAW devices at the best operating conditions
	Distributed acoustic reflecting transducer (DARTs)	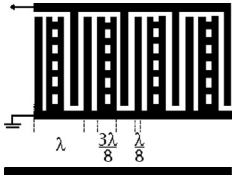	A sequence of identical cells with length equal to wavelength, and each cell has two electrodes width of lamda/8, and one electrode of width lamda/4, the inter-electrode space are lambda/8. Variable reflection can be achieved to cancel the net reflection and transmission effects	By segmenting the reflecting electrodes, a variable reflectivity can be achieved, thus providing design flexibility	Essential for SAW microfluidics and sensors as it not only improves the performance, but maintains the SAW devices at the best operating conditions
	Floating electrode unidirectional transducers (FEUDTs).	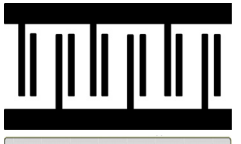	One (or more) electrodes is/are not connected to others and floating Fanned SPUDTs. Inclined grating as reflectors, Fanned SPDUT, to increase the bandwidth of frequency	Floating electrode SPUDT (FEUDT), the shorted or open electrode configuration changes the transductor/reflector interaction and select forward and reverse directions	
	Apodized IDT	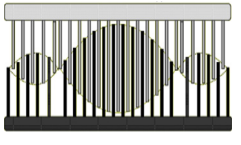	Varying and non-uniform beam profiles. In apodization technique, the top electrode is designed with non-parallel edges which increases the resonant path and leads to more attenuated modes and thus degrades the strength of spurious lateral modes	Complex patterns. Apodization design is difficult to be used for pairs or many similar IDTs or the frequency response would become complex	Generally used for wave shaping and manipulation of frequency response of the IDT

(*continued on next page*)

Table 9 (*continued*)

Mode	Name	Illustration	Advantages	Problems	Applications
	Dispersive delay lines And Chirped IDTs		Varying the width and frequency of IDTs in order to control wave modes and reflectivity, to linearly modulate the wave pitch or frequency. Including expander: (from large width to smaller width); and compressor (from small width to larger width). The frequency can be changed up gradually by decreasing the electrode spacing or down by increasing the electrode spacing	Can have large bandwidth	For manipulating droplets in different directions and for focused acoustic energy propagation
	Slant IDT Or tapered IDTs		Slanted transducer: varying the frequency in the IDT section by changing the electrode periodicity. Slanted down-chirp filter; linear phase slanted transducer have a very broad bandwidth, and they are able to change the moving direction of a droplet by changing the operating frequency continuously	The slant IDT SAW devices have a very broad bandwidth	They are able to change the moving direction of a droplet by changing the operating frequency continuously
	Focused or circular IDTs		Large focused acoustic force or energy, and have been utilized for better pumping and mixing, and for sensing with better sensitivity and resolution	Due to the anisotropic nature of most piezoelectric crystal cuts, it is recommended to add IDTs with a concentric elliptic shape, etc., whose curvature might be smaller than that of the wave surface	The curved IDTs have a large acoustic force, and have been utilized for better pumping and mixing, and for sensing with better sensitivity and resolution. The curved IDT SAW has the highest droplet motion velocity, concentration effects. [582]
Film bulk acoustic wave electrode and reflectors Step-like frame FBAR structure [583]	LFE	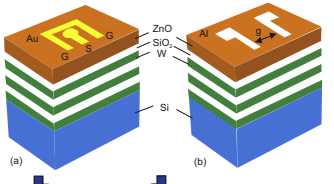	Lateral excitation between two planar IDTs to generate shear mode waves	Low signal to noise ratio [584]	Generate shear waves
	Step-frame electrode		Design of a new step-like frame structure film bulk acoustic wave resonator operating near 1.5 GHz. The spurious resonances are eliminated effectively and a smooth pass band is obtained with an effective coupling coefficient of 5.68% and quality factor of 1800	Complicated process	Eliminate spurious resonances
	Contour mode	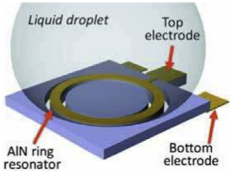	Resonator structures based on film bulk acoustic wave resonant designs	Fragility of the structures	Enhancement in sensitivity

Table 9 (*continued*)

Mode	Name	Illustration	Advantages	Problems	Applications
Lamb wave resonators (LWRs)	IDTs	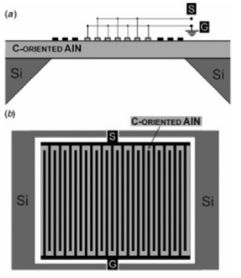	Resonator structures based on IDT designs	Fragile of the structures	Enhancement in the Lamb wave's sensitivity

film devices, one can control the wave velocity in all directions and in particular render it isotropic in the normal plane, which is of particular significance when producing an isotropic focused-SAW (FSAW) or annular- SAW with a fixed operation frequency. Previously, isotropic SAWs generated on ZnO thin films, with a (0002) crystal orientation have been proposed, including a "liquid needle" which used a circular self-focused bulk wave acoustic transducer to generate a focused acoustic wave and produce a needle-shape liquid column on the free liquid surface [565–570]. However, the device fabrication involved multiple lithography processes together with silicon bulk micromachining, increasing the complexity of processing.

The main objectives for the new types of electrode designs include: (i) increasing the generation efficiency of acoustic waves; (ii) improving spurious signal suppressions; (iii) decreasing insertion loss; and (iv) reducing signal distortion. For designing electrodes and IDT patterns, some key parametres must be considered, including resonant frequency, power output density, choice of electrode materials, shape/dimensions (including thickness), positions, substrate anisotropic properties, and number of reflective electrodes [571]. It is possible to design electrodes with different mechanical to electrical periodicity to enable harmonic operation, which can allow operation at a higher frequency for a given fabrication resolution. The arrangements and shapes of electrodes can also control the reflectivity and directionality (bidirectionality/unidirection ality) of the electrode arrays and their frequency spectrum. New techniques such as electron beam lithography, focused ion beam (FIB) milling, or nanoimprinting, have been used for making sub-micron wavelengths leading to super-high frequency devices. For example, a super-high frequency (20 GHz) SAW device based on $ZnO/SiO_2/Si$ was made using nanoimprint lithography [572,573].

Table 9 summarizes the common designs which are suitable for microfluidics and biosensing together with their illustrations and attributes.

6. Recent development in thin film acoustic wave biosensors

Thin film acoustic wave devices have been used for detection of adsorbed biomolecules, viruses, bacteria and cells on surfaces through the interactions of DNA with complementary strands, antibody with antigen, etc., and specific recognition of protein-ligands by immobilized receptors [585]. This affinity-based detection concept can be utilized to diagnose early stages of diseases and cancers, allowing for early intervention and measures to be taken to prevent further development of illnesses and spreading of cancers [17].

Recent developments in thin film acoustic devices have been focused on:

a. Sensors prepared on cheap and commonly used substrates to reduce the cost, or new substrate materials to introduce novel functionality, or flexible substrates for wearable and wireless applications;
b. High frequency sensing with improved sensitivity;
c. Shear-wave or Love mode based thin film devices for liquid sensing;
d. Development of various sensing layers/material systems;
e. Integration with acoustic streaming and microfluidics to form the LOC systems.

6.1. SAW biosensors

6.1.1. SAW biosensors made of ZnO/Si and ZnO/glass

Devices based on ZnO/Si SAWs have been traditionally used for pH, UV and humidity sensing [586–591]. Recently, a number of studies on biosensing applications have been reported. For instance, a ZnO/Si SAW device was modified to serve as streptavidin/biotin based immunoassay for detecting mammoglobin, a well-known breast cancer marker. This device showed a frequency sensitivity of 8.704 pg/Hz and a mass sensitivity of 2810.25 m^2/kg [592]. A similar ZnO/Si SAW device (as shown in Fig. 12a) was used to detect a prostate-specific antigen (PSA) cancer marker through antibody-antigen immuno-reaction with a good selectivity against bovine serum albumin (BSA) [593,594]. Similarly, the ZnO/Si SAW device was used to detect the bio-specific interaction between 6-(2,4-dinitrophenyyl) aminohexanoic acid (DNP) antigen and its antibody. The resonant frequency shifts of the SAW device increased exponentially as a function of anti-DNP antibody concentration in the range of 20–20,000 ng/ml.

For biosensing applications, the Sezawa mode with a higher frequency generally shows a higher sensitivity than that of the Rayleigh mode. For example, SAW devices made of $ZnO/Si_3N_4/Si$ using a Sezawa mode with a frequency of 1.497 GHz were used to detect the human immunoglobulin-E (Ig-E) with a good sensitivity of 4.44×10^5 m^2/kg [595].

Shear wave ZnO SAW biosensing was demonstrated using inclined angled ZnO films [596], with these films being utilized as Love mode sensors [597]. A common approach for making a ZnO-based Love mode sensor is using a polymer layer such as PMMA, polyimide, SU-8 or Parylene C as the wave-guiding layer on top of the inclined ZnO layer. However, the polymer waveguide leads to a relatively large intrinsic acoustic attenuation compared to the other commonly used solid waveguides, such as SiO_2.

The SAW sensor made of $ZnO/SiO_2/Si$ (often regarded as a Love mode SAW) has a sensitivity 8.64×10^6 m^2/kg [598], which is about 2–5 times higher than those made of $ZnO/LiTaO_3$ and SiO_2/quartz [599]. Another Love mode SAW biosensor made of $ZnO/SiO_2/Si$ was used for the detection of interleukin-6 (IL-6) [600], operating at frequencies of 747.7 MHz and 1.586 GHz. The ZnO film surface was functionalized by immobilizing the monoclonal IL-6 antibody both through direct sur-

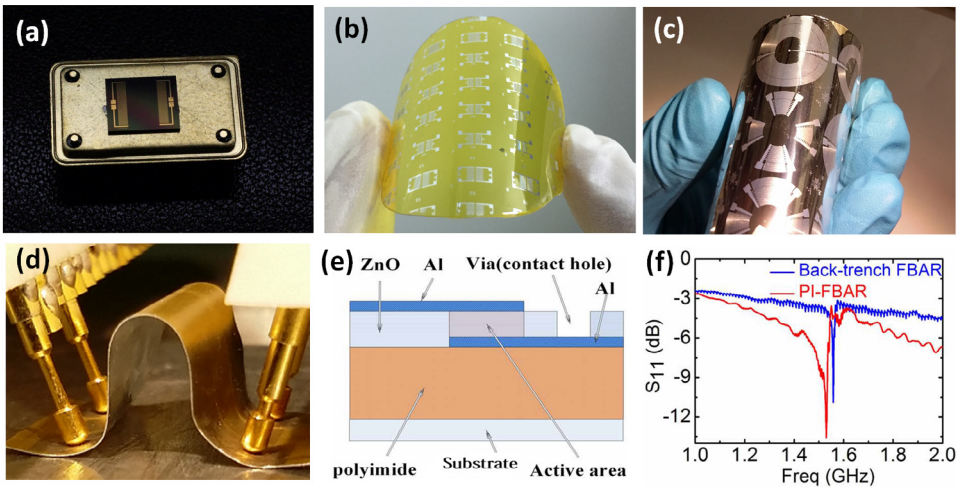

Fig. 12. Thin film ZnO acoustic wave sensing devices: (a) A ZnO/Si SAW device bonded onto a package with Au wires; (b) flexible ZnO/PI surface acoustic wave devices under a bending condition; (c) fabricated ZnO/Al foil based surface acoustic wave devices with various IDT designs; (d) testing of Al foil based SAW devices working under a significant bending condition; (e) schematic illustration of a flexible FBAR device with Al electrodes made on PET directly; (f) comparison of the resonant frequency of the flexible FBAR with a traditional back trench FBAR on Si substrate.

face adsorption and covalent binding on gluteraldehyde. A passivated ZnO SAW sensor with a resonant frequency of 400 MHz was developed for long-term monitoring of *E. coli* growth in an animal serum or bacterial growth media, and the film was protected by a thin layer of Al_2O_3 film [601]. This Al_2O_3/ZnO/SiO_2/Si SAW device has a detection limit of 5.3 pg.

By using a transparent conducting oxide layer such as AZO or ITO as the electrodes, ZnO films have also been deposited onto glass substrates to obtain a fully transparent SAW device [602–605]. Various attempts at sensing have been performed, including strain, temperature, humidity and pressure, but there are not many reports of biodetection applications.

6.1.2. SAW biosensors made of AlN/Si

SAW devices made of AlN/Si have higher phase velocities than ZnO/Si SAW devices. Such an AlN/Si Rayleigh SAW device with a velocity of 4590 m/s was fabricated for surface biofunctionalisation using amiosilane molecules as a cross-linker to form a monolayer of DNA-Au particles [606]. The electrostatic interaction between the positively charged surface amine groups and negatively charged DNA-Au nanoparticle conjugates allowed for the self-assembly of a probe nanoparticle monolayer onto the functionalized AlN surfaces under physiological conditions. However, not many reports on AlN based SAW biosensors have been reported recently [607]. The main reason is probably attributable to difficulties in depositing the required thick AlN film for fabricating a SAW device due to the large film stresses and poor film/substrate adhesion associated with AlN films.

6.2. Lamb wave and flexible acoustic wave biosensors

6.2.1. Lamb wave biosensors

Membrane-based thin film Lamb wave devices have been used for biosensing, especially for applications in a liquid environment [608]. For Lamb wave sensing, the S_0 mode is more preferred for liquid sensing as it has higher phase velocities (5500 m/s for ZnO and ~10,000 m/s for AlN) and low phase velocity dispersion. For example, a 2 μm AlN membrane Lamb wave device showed a fluid mass sensitivity of 200 cm^2/g [609]. As the propagation velocity of the FPW (commonly known as the A_0 mode) in the membrane is lower than that in the fluids on the surface, the acoustic energy is not easily dissipated. The performance varies significantly with membrane materials and thickness [610], as do the damping and noise performance of the sensing layer [611,612]. A ZnO based Lamb wave device was used to monitor the growth of bacterium-pseudomonas putida in a boulus of toluene, as well as the reaction of antibodies in an immunoassay for an antigen present in breast cancer patients [613]. Another Si/SiO_2/Si_3N_4/Cr/Au/ZnO Lamb wave device was used to detect human IgE based on conventional cystamine SAM technology, with a sensitivity as high as 8.52×10^7 cm^2/g at a wave frequency of 9 MHz [614].

Lamb wave biosensors, athough extensively studied at the end of 1990s, have not been widely reported lately because:

(1) The sensitivity is not as high as that of the other devices mentioned previously due to the low operation frequency.
(2) The thin and fragile membrane structures are difficult to fabricate.
(3) The fragility sets a practical limit to the minimum film thickness of the membrane.
(4) The thin film structure has a high temperature sensitivity.

However, recently there have been significant improvements in thin film based Lamb wave devices including new structural designs, electrode designs, high-frequency-wave modes, and Lamb wave on flexible SAW devices [615–617].

6.2.1.1. Progess in structural designs. Thin film Lamb wave resonators (LWRs, see Table 9) based on S0, A0, or higher A and S modes have recently been widely explored [618,619]. For example, an AlN/SiO_2/diamond LWR has been developed with a super-high frequency of tens of GHz, and a high k^2 value of 2–4% [620]. The LWR was found to have a better performance than the standard membrane Lamb wave structure. Another new Lamb wave sensor example is a thin film membrane guided wave resonator designed to use the AlN or ZnO as the waveguide, and this provides acoustic confinement, with the air/solid surface on one side and an acoustic Bragg mirror on the other [621]. The bottom electrode was implemented as a floating metallic plane, while the top electrode was patterned to form IDTs. The advantage of this guided wave resonator is the ability to adjust the resonant frequency by design of the IDT structure. Other exampes include: SMR and IDT guided wave resonator with Bragg mirrors and guided Lamb waves based on AlN/Al strcutures [622].

6.2.1.2. Progress in electrode designs. An example of this is a checkerboard pattern of electrodes which was fabricated onto an AlN membrane, and generated a Lamb wave with a k^2 value of 5.33% at a frequency of 285.3 MHz [623].

6.2.1.3. High frequency-wave modes. Higher order modes of the S Lamb waves rather than the S_0 modes can achieve better sensitivity for applications due to their high phase velocity, low phase velocity dispersion, and lower impedance. However, higher order modes of the A_0 Lamb waves could have more signficant attenuation in the liquid, thus might not be suitable for liquid sensing applications.

6.2.2. Flexible acoustic wave devices

As mentioned in Section 2.1, one of the great advantages for thin film acoustic wave devices is that the device can be made on flexible substrates, such as plastics, polymers or metallic foils. Fabricating SAW devices on inexpensive and flexible substrates has a huge potential for production of wearable, disposable or recyclable applications. Recently, a number of studies were carried out on the fabrication and characterisation of flexible SAW devices based on both ZnO and AlN films deposited on various polymers including polyethylene terephthalate (PET), polyimide (PI, see Fig. 12b) and polytetrafluoroethylene (PTFE), bendable glass, flexible ultrathin silicon wafers, and metallic foils (see Fig. 12c and d) [624]. Various sensing characterisations for UV, strain, pressure, humidity and temperature have been explored using these flexible SAW devices, although little work has been focused on bio-sensing [625].

The deposition processes of ZnO films onto polymeric substrates have been extensively studied [626–632]. Generally well-adhered c-axis oriented ZnO films can be deposited on different polymer substrates, although stress, adhesion and texture have always been major concerns in this process [633–635]. Zhou et al. [636] investigated the effects of the deposition conditions, crystal quality and film thickness of ZnO films on the performance of the ZnO/polyimide flexible SAW devices. Flexible SAW devices with a resonant frequency of 153 MHz, a phase velocity of 1836 m/s, and a coupling coefficient of 0.79% have been reported on a 4-μm thick ZnO film, demonstrating great potential for biosensing applications.

Acoustic wave propagation of a thin film SAW device is influenced significantly by the substrate materials. Akiyama et al. [637] deposited AlN films on polyimide substrates and observed the piezoelectric effect as a function of pressure variations. The authors also investigated AlN thin films deposited on polyimide diaphragms to obtain a high-sensitivity response [638]. Jin et al. reported AlN film SAW devices made on a polyimide substrate using reactive DC magnetron sputtering [639]. Similar AlN/PI flexible sensor work has also been reported by Smecca et al. [640]. An AlN film with a thickness of 6.2 μm was deposited onto a PI substrate and SAW devices were fabricated with a centre frequency of 520 MHz [641].

Despite recent progress, significant technological challenges in the fabrication of flexible SAW devices on polymer substrates remain, and these are listed as follows [642]:

- There can be significant attenuation and dissipation of acoustic waves and energies into polymer substrates.
- Most flexible substrates are amorphous, hence they do not match the lattices of the required thin films, thus the crystallinity of the films is not as good as those on silicon.
- The large mismatch in thermal expansion coefficients between the substrates and the piezoelectric films can cause serious problems during film deposition.
- The poor adhesion of thin films on the polymer substrates is another potential problem.
- SAW devices generally require thick piezoelectric layers (the thickness is usually required to be larger than 10% of the SAW wavelength), which makes film growth and fabrication difficult.
- As the substrates for flexible acoustic waves are generally very thin, multiple wave modes, such as SAWs, Lamb waves or Love mode, Sezawa, and higher harmonic modes can be generated. Therefore, the vibration modes need to be systematically investigated for sensing and microfluidic applications.

Glass substrates are often used to make transparent electronics. However, glass is rigid and not suitable for flexible electronics. Chen et al. [643] used an ultrathin flexible glass, Corning® Willow® Glass with a thickness of 100 μm, and fabricated flexible/transparent ZnO SAW devices, which were developed as strain sensors with an extremely broad strain detection

ranges. Such flexible SAW devices showed excellent flexibility, stability and repeatability when subjected to repeated bending.

Flexible aluminium foil substrates promote the desired texture growth of ZnO films, and provide good film adhesion, and reduce film stress during the deposition process, all of which are difficult to achieve on a polymer substrate. Al foils, compared to their polymer counterparts, have the distinct advantages of deformability (forming and then maintaining temporary shapes) and plasticity (easily returning back to their un-deformed shape), and they thus solve many common problems associated with most polymer based flexible devices including large energy dissipation and permanently deformed shapes. Using commercially available large area Al foils and thin film processes, mass-production or roll-to-roll processes at a low cost can be implemented to fabricate high performance flexible/deformable acoustic wave sensors and microfluidic devices (see Fig. 12c). The flexibility and deformability of the ZnO/Al foil acoustic wave devices have been demonstrated with bending strains up to 1.38% (with one example shown in Fig. 12d). The fatigue and cycling performance of the flexible devices have been tested by bending the devices with a fixed strain of 0.6% for up to 2000 cycles, and the resonant frequency of the device decreased only by 0.91% [644]. These types of ZnO/Al foil acoustic devices have also been annealed at different temperatures to find the best conditions for sensing applications [645]. However, biosensing using this type of SAW device is yet to be conducted to prove its suitability for biosensing applications.

6.3. FBAR biosensors

6.3.1. FBAR biosensor on silicon

FBAR biosensors have recently attracted great attention due to their inherent advantages over the SAW, Lamb wave and QCM counterparts such as high sensitivity, high power handling capability and small size [646–649]. The ability to generate and trap acoustic waves within a thin piezoelectric layer between two electrodes allows the device size to be scaled down to a footprint two to four orders of magnitude smaller than devices based on SAW and QCM [650,651]. The small size makes the integration of an FBAR array for parallel and multi-variable detection feasible. The size reduction also decreases the fabrication cost of the devices. FBARs typically have a resonant frequency of a few GHz, and devices with frequency of tens of GHz have been demonstrated [652,653]. Various vibration modes have been explored in the operation of FBAR devices, including the thickness extensional mode (TEM) and the thickness shear mode (TSM, which can be generated on c-axis inclined films), as well as the lateral field excitation (LFE) mode [654–663].

6.3.1.1. Fbars with c-axis film structures. Gabl et al. reported a label free ZnO FBAR gravimetric biosensor with an operating frequency of 2 GHz to detect DNA and protein molecules [664]. The high frequency allows for a sensitivity of 2400 Hz cm^2/ng, which is three orders of magnitude higher than that of a conventional QCM device operated at a frequency of 20 MHz. An FBAR sensor made of ZnO film with a resonant frequency of 800 MHz has been used to investigate *in-situ* growth of bacterial layers, protein and DNA, achieving a sensitivity of 2 kHz cm^2/ng and a minimum detectable mass of 1 ng/cm^2 [665]. An odorant biosensor based on ZnO FBAR devices with a resonant frequency of 1.5 GHz has also been designed in which the device surface was functionalised with odorant protein to detect organic vapours. Another FBAR device made of Al/ZnO/Pt/Ti has demonstrated a sensitivity of 3654 kHz cm^2/ng with a good thermal stability [666]. Dong et al. [667] proposed an electrically tuneable Au/ZnO/Al FBAR where the stack resonator is Au-piezoelectric ZnO-Al and the Schottky diode junction is made using an Au/n-ZnO semiconductor structure. A ZnO SMR based FBAR device has also been used to detect the tumour marker Mucin-1 based on a standard binding system of avidin-biotin [668].

Compared to the ZnO films, the AlN film is attractive for fabrication of FBAR devices owing to its advantageous characteristics, such as high electric resistivity, low dielectric loss, high bulk acoustic wave velocity, good thermal stability and chemical stability [669]. AlN FBAR devices with an operating frequency of 2.48 GHz and a sensitivity of 3514 Hz cm^2/ng were reported for the detection of carcinoembryonic antigen (CEA), which is associated with breast, colorectal and lung cancers [670]. Similarly, AlN based FBARs with a protein functionalized surface were used as a breathe analysis biosensor to study the feasibility for sensing an odorant binding protein with N,N-diethyl-*meta*-toluamide as its ligand. An AlN based FBAR was also used as a biosensor for detection of the CEA [671], and the resonator consisted of an AlN piezoelectric layer and a Mo/Ti Bragg reflector with a working frequency approaching 2.0 GHz. The CEA binding aptamers were self-assembled on the top gold electrode as the sensitive layer to capture the CEA molecules. The sensor modified with the CEA binding aptamer exhibited a high sensitivity of 2284 Hz cm^2/ng and a Q value around 520.

Binding of biomolecules on the surface of a resonator is essential for biodetection. This requires the biosensors having not only a high frequency but also a high density of binding sites. The SMRs made using CNTs as the top contact electrode have higher operating frequency compared to that with Au electrode owing to the reduced electrode mass and higher Young's module of the CNTs. The porous CNTs network provides much higher density of binding sites, leading to an improved sensitivity compared to that with Au electrodes.

6.3.1.2. Shear wave FBARs and LFE FBARs. For FBAR sensing in liquid, the development of both ZnO and/or AlN films with crystal orientation inclined relative to the surface normal enables the generation of shear waves suitable for detection in liquid [672–676]. For example, FBAR viscosity sensors have been developed using the films with tilted c-axis orientations [677], which were used for detecting self-assembled monolayers (SAM). A ZnO shear mode FBAR device utilizing a (1120)-textured ZnO film was used in a water-glycerol solution, with a relatively high operating frequency of 830 MHz and a sen-

sitivity of 1000 Hz cm^2/ng [678]. For an avidin/anti-avidin system, the fabricated FBAR device had a high sensitivity of 585 Hz cm^2/ng and a mass detection limit of 2.3 ng/cm^2. Link et al. have also made a shear wave FBAR device with a stable temperature coefficient of frequency [679]. A shear wave mode AlN FBAR was made using c-axis 20° inclined AlN film with a resonant frequency of 1.2 GHz, with a high mass sensitivity of 2045.89 Hz cm^2/ng for CEA detection in a liquid condition [680]. Another shear mode FBAR device, made utilizing the AlN films with a 23°-tilted columnar structure and was used for sensing of human IgE with the high frequency of 1.175 GHz [681]. Similarly, a shear-mode FBAR device based on *c*-axis 23°-tilted AlN thin film was used as a biosensor for human IgE biosensing [682]. An Au/Cr layer was deposited at the back side of the FBAR and used as the detection layer. The Au surface was modified using self-assembled monolayers, achieving a shear-mode FBAR device with a k_t^2 value of 3.18% and a sensitivity of about 1.425×10^5 cm^2/g for human IgE detection. This FBAR sensor is sensitive to each injection of anti-avidin, BSA or avidin in the microfluidic system.

However, the deposition of large scale and uniform c-axis tilted piezoelectric thin films is not straightforward. The process requires sophisticated equipment and setups for tilting the substrate/wafer and the electrical field as explained in Section 4.1.

Another potential method for liquid-phase biodetection for the FBAR devices is using the LFE structure for the piezoelectric layer as shown in Table 9 [683–686]. This lateral structure FBAR requires both signal and ground electrodes being in-plane and parallel to the exposed surface of the piezoelectric film [687,688]. The resonator configuration consists of a laterally excited, solidly mounted ZnO or AlN thin film resonator that can easily be integrated with an acoustic mirror. The ZnO LFE FBAR device was reported to operate stably in biologically equivalent environments such as NaCl solution [689]. A pure shear mode ZnO FBAR based on the LEF design was used in air, water and viscous liquid [690], and reported to deliver a mass sensitivity of 670 Hz cm^2/ng, and a mass resolution of 0.06 ng/cm^2 [691]. Whole blood coagulation sensing has also been reported using an LFE FBAR device [692].

However, Clement et al. [693] argued that using the lateral excitation of c-axis vertical films (LEF designs) is ineffective in generating shear mode waves, but instead produces dominant longitudinal thickness modes [694]. Laterally structured FBARs normally have a low quality factor and the mechanism of the exciting resonance is not yet fully understood. More work is required before this device type can be effectively used as a liquid sensor. Furthermore, lateral structure FBARs have a relatively narrow active area, and are difficult to incorporate with microfluidic components such as microchannels for practical sensing applications.

Although FBAR based biosensors shows a high sensitivity and good resolution, some issues remain to be addressed. FBARs have a better sensitivity than the other types of acoustic wave sensors, but they do have a low quality factor, a high acoustic wave attenuation, large noise level. The shape and material properties of the electrodes also significantly affect the quality factor. Other issues of potential concerns include the sensor packaging and the effect of high frequency on biochemistry.

Contour-FBAR (C-FBAR) structures could be a possible solution in which a suspended circular shaped AlN ring is sandwiched between the top and the bottom electrodes (see Table 9) [695]. The AlN ring is excited with the vibration displacement parallel to the resonator/liquid interface, thus reducing the acoustic energy loss and increasing the Q factor. The C-FBAR has been used to characterize an aptamer-thrombin binding pair for a biosensor with a mass sensitivity of 112 Hz cm^2/ng, and a mass resolution of 1.78 ng/cm^2.

6.3.1.3. FBAR or SMR?. One issue associated with FBAR devices is that there is always a choice between the FBAR and SMR for biosensing applications. The selection of a specific design is dependent primarily on the ability of the users to design/fabricate membranes and/or Bragg reflectors. Garcia-Gancedo et al. showed that identically designed FBAR and SMR devices resonating at the same frequency exhibit different responsivities to mass loadings, with FBARs showed a better sensing performance [696]. This shows that FBAR devices should be favoured over SMRs in gravimetric sensing applications if the FBARs' fragility is not an issue.

6.3.2. FBAR on flexible and arbitrary substrates

A flexible FBAR with a working frequency as high as of 5.2 GHz [697] has been fabricated on a polyimide substrate using piezoelectric thin film AlN for acoustic wave excitation. The resonators showed good performance after experiencing repeated bending cycles. An AlN FBAR device has also been fabricated onto a thin silicon wafer with a thickness of 50 μm for flexible microsystems [698]. Petroni et al. [699] fabricated FBARs consisting of Mo/AlN/Mo layered structures on a PI substrate.

The FBAR devices with a back-trench membrane or a membrane over an air-gap often have a low yield due to residual stresses in both suspended membrane and piezoelectric layer, as well as a lengthy etching processes. Whereas the Bragg mirror SMRs require long deposition time and precise control of the thicknesses of all layers, making them not so cost-effective. Chen et al. recently [700] proposed a new FBAR architecture, which could be made on many substrates including metal plates, glass, and even normal printing paper as well as roughened silicon without compromising the performance of the FBAR devices. The new idea is to fabricate resonant FBAR structures on a pre-deposited polyimide layer which has a high attenuation coefficient and a near-zero acoustic impedance that can confine the acoustic wave within the piezoelectric layer above as shown in Fig. 12e. This new design of FBARs allows the fabrication of high performance devices on arbitrary substrates of almost any surface morphology, such as flexible and transparent polymer, rigid and non-planar metal foils and semiconductor wafers. The fabrication process is simple, the yield is high, and the devices are extremely robust and strong with a Q-factor comparable to those with a back-trench on rigid substrate (see Fig. 12f).

Similarly, a flexible lateral field excited FBAR based on an AlN film deposited onto PI substrates was fabricated [701]. Using a thickness extension mode, the flexible FBAR achieved a working frequency of 5.23 GHz, and functioned well after repeated bending processes. A flexible FBAR device with Al electrodes was also made on a PET substrate directly with a series and parallel resonant frequency at 1.188 and 1.211 GHz and k^2_{eff} of 4.7% and a Q value of 56.7 [702]. In summary, flexible FBARs have made substantial progress recently, but their application in sensing, particularly biosensing is yet to be significantly explored.

6.4. Dual wave mode or multiple wave modes

Dual mode or multiple wave modes with different frequencies are frequently observed in SAW, Lamb wave and FBAR devices. Examples include Rayleigh and Sezawa based modes for SAW devices; shear-horizontal and longitudinal waves in c-axis inclined SAW or FBAR devices; Rayleigh and Lamb waves in flexible acoustic wave devices; and fundamental and higher S and higher A modes in Lamb wave devices [703]. These waves might have different sensing performance for different properties. For example, Zhou et al. found in Lamb wave devices that the A_0 mode is more sensitive to density changes, and the S_0 mode is more sensitive to viscosity changes, thus these two modes can be used for density and viscosity sensing, respectively [704]. The reason is that the mode with perpendicular motion (longitudinal wave dominant) is sensitive to density changes, whereas the mode with parallel motion (shear wave or transverse wave) is more sensitive to viscosity [705]. By changing the thickness of film/substrates, many higher order modes of Lamb waves can have either predominantly longitudinal waves or transverse waves, and thus can be used for density or viscosity sensing applications, respectively.

For SAW devices, multiple frequencies and multi-modes can be excited using multilayer designs or special electrode or IDT designs such as single-double (operated at f_o and $2f_o$), double-double (operated at f_o and $3f_o$), meander line (operated at $3f_o$) or floating electrode unidirectional transducers (FEUDTs, as shown in Table 9) [706], which offers the abilities to undertake simultaneous sensing of parametres, such as mass loading, viscosity, or conductivity changes.

FBARs are very sensitive to the environment, including temperature and humidity [707]. FBAR devices could generate different wave modes, with varying sensing performance. For example, an FBAR with two resonant frequencies and opposite responses to temperature changes has recently been reported. The two resonant modes responded differently to changes in temperature and pressure [708], and the pressure coefficient of frequency for the lower frequency peak of the FBAR sensors is approximately -17.4 ppm kPa^{-1}, while that for the second peak is approximately -6.1 ppm kPa^{-1}. Using a similar approach, Garcia-Gancedo et al. have successfully used two different frequencies of one FBAR device to measure mass loading and temperature effects [709], simultaneously.

7. Thin film SAW based acoustofluidics

As already mentioned in Section 1.3, acoustically induced force or pressure enables liquid and particle manipulation in microfluidic devices. Basic processes such as liquid pumping, mixing, ejection and atomization have been demonstrated with devices made of bulk piezoelectric material such as $LiNbO_3$, and the readers may refer to several review papers for more details of acoustofluidics based on bulk $LiNbO_3$ SAW devices [710–713]. Recently, acoustic wave devices based on ZnO and AlN thin films have shown the same capability and better performance in some aspects and applications (for example in large RF power conditions) [714,715]. This section will focus on recent progress in thin film acoustofluidics, in particular SAW devices based on ZnO thin films. Microfluidics using AlN/Si [716,717] and AlScN/Si SAW devices [718] have not been as frequently reported.

Substrates such as silicon, glass and polyimide (PI), on which the piezoelectric layer is deposited, play a significant role on the device performance in acoustofluidic applications [719]. Acoustic wave devices made of a ZnO film on Si typically generate Rayleigh and Sezawa modes, whereas those made with ZnO on glass only generate the Rayleigh mode due to the very close acoustic velocities of the glass substrate and the ZnO layer. Devices made from of ZnO film on a flexible PI substrate produced Rayleigh and Lamb modes. Devices made of ZnO film on Si provide the best transmission properties, and the best microfluidic performance in term of acoustic streaming velocity among the devices on these three types of substrates. Compared to devices made on silicon and glass, the flexible devices based on PI have an inferior performance due to the large acoustic attenuation of the PI as well as the large mismatch in acoustic impedance at the interface between ZnO and PI. Thin film based flexible devices on Al foils show a better microfluidic performance compared to those made on polymers.

7.1. Acoustofluidics with thin film SAW devices

7.1.1. SAW streaming and particle concentration

Similar to the bulk devices discussed in Section 1.3, a single IDT on a thin film SAW device induces acoustic streaming in a liquid droplet placed on the device surface. The streaming flow has a typical butterfly pattern due to the recirculation of liquid within the droplet as shown in Fig. 13a and b. The two major vortexes of the butterfly pattern are recognizable from experimental (top and side views in Fig. 13a and b) and numerical results (Fig. 13c). The shapes of the streaming patterns and vortex positions depend on the surface hydrophobicity, droplet sizes, relative position to the IDTs and the IDT shapes.

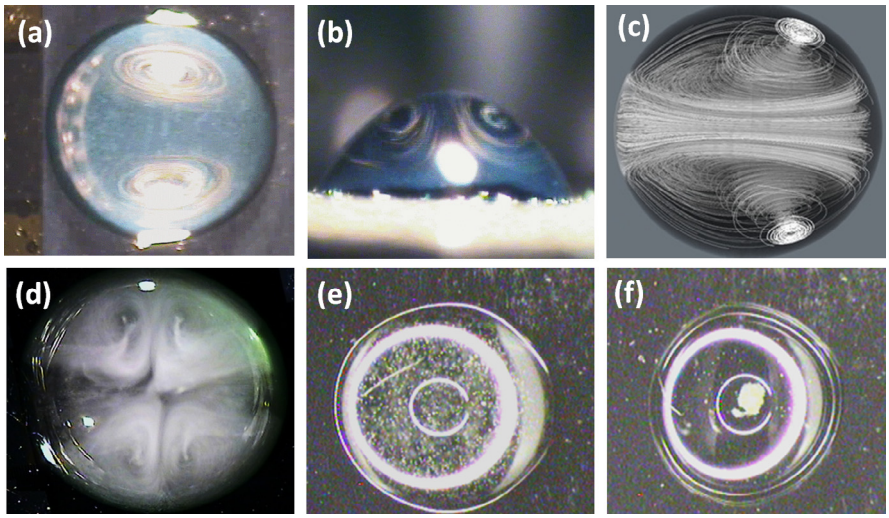

Fig. 13. Flow patterns of acoustic streaming in a droplet induced by ZnO/Si SAWs: (a) Top view, where a single IDT on the left causes the butterfly streaming patterns inside the droplet; (b) the front-side view of butterfly streaming patterns induced by the ZnO/Si SAW; (c) the corresponding simulated streaming pattern using finite volume software induced by a SAW launched from the left; (d) the experimentally obtained streaming pattern induced by two SAWs launched from both sides of the droplets; (e) The liquid droplet with uniformly distributed 6 μm polysterene particles inside; (f) Particle concentration induced by the SAW actuation for the same droplet in (e) when the droplet is put on the side of the IDT of the ZnO/Si SAW device.

Using a pair of IDTs and launching the waves from both sides of the droplet, a double butterfly streaming pattern can be generated. Fig. 13d shows the four vortexes generated with this configuration. Placing a droplet on the edge of the IDTs of a ZnO/Si SAW device concentrates particles inside the droplet as shown in Fig. 13e and f.

7.1.2. Liquid transport and mixing

Fig. 14 illustrates the typical transport and mixing processes of two droplets using SAWs generated by a ZnO/Si SAW device. The smaller droplet was transported by a SAW launched from the left as shown in Fig. 14a and b. After coalescence, the merged droplet was mixed by the induced acoustic streaming as shown in Fig. 14c and e. The images show that the small droplet was deformed and transported by rolling and sliding movements. The flow pattern, shown in Fig. 14, facilitates rapid mixing through convective transport within the merged droplet. Transportation of a droplet depends on the hydrophobic treatment of the surface, RF power applied, frequency, and droplet size.

7.1.3. Liquid jetting

On a hydrophobically treated ZnO SAW device surface, if the acoustic power is high enough, the droplet will be ejected from the surface. Using one side IDTs, large acoustic energy dissipated into the droplet results in a large inertial pressure in the droplet to overcome the capillary force, leading to a coherent cylindrical liquid beam as shown in Fig. 15a. The droplet was continuously ejected in an elongated jetting beam following the Rayleigh angle until the entire water droplet has been consumed as shown in Fig. 15a. The jet length increases with the applied RF powers. If the liquid droplet volume is large, then the droplet will experience significant deformation before being fully ejected from surface as shown in Fig. 15b.

Vertical jetting of the droplet can be realised using various methods with two examples shown in Fig. 15b and c. The first example in Fig. 15b shows that vertical jetting can be easily generated by using two opposite IDTs in a standing-wave configuration. Fig. 16 illustrates the high-speed images showing the step-by-step droplet ejection process using this method. The SAWs are launched from two sides of the droplet, thus the droplet is pushed up from both sides by the opposing waves

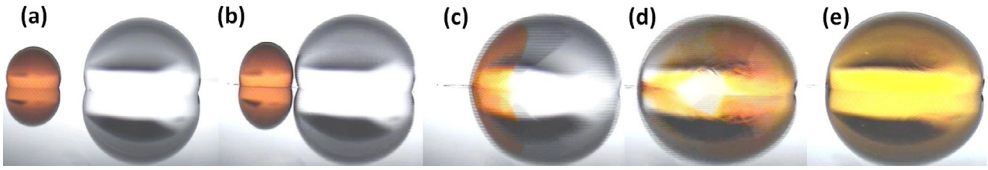

Fig. 14. Acoustic mixing of a water droplet with a red dye droplet at different durations induced by a ZnO/Si SAW device with the SAW launched from left side; (a) the two separated droplets at time t = 0 s, (b) the left dye droplet is pumped towards the large droplet at time t = 0.4 s, (c) the merging of the dye droplet and internal flow along Rayleigh angle inside the large droplet at time t = 0.44 s, (d) internal streaming patterns at time t = 0.45 s and (e) a uniformly mixed droplet at time t = 0.5 s.

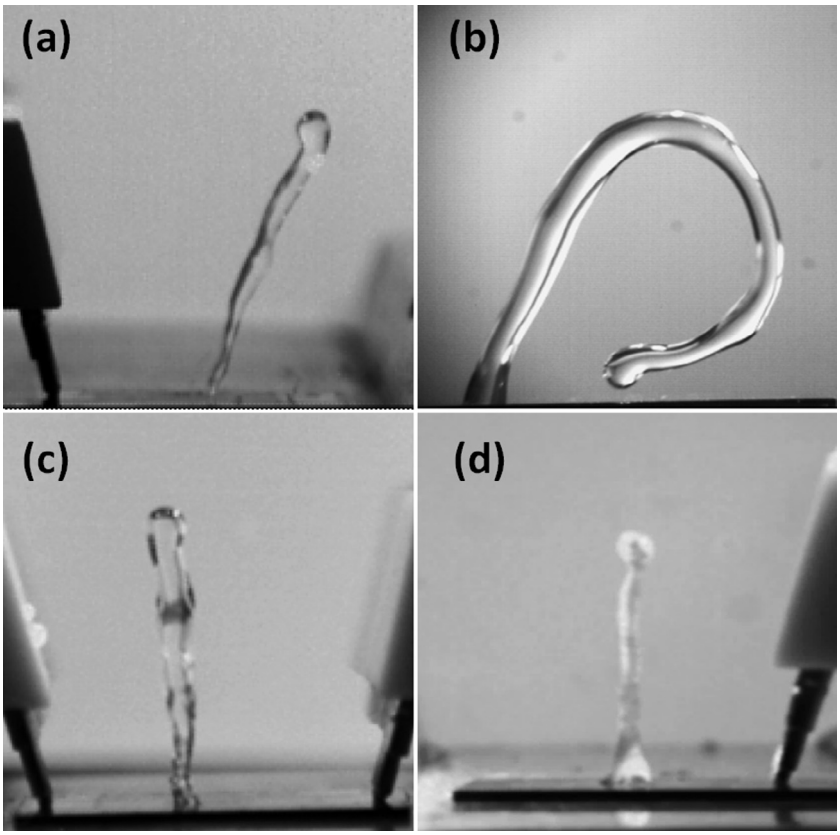

Fig. 15. (a) Liquid droplet jetting generated using a single IDT for a droplet of 2 μL induced by the surface acoustic waves on a ZnO substrate (input power of 28 W). The SAW generates from left to right. (b) A large droplet (30 μL) experienced significant deformation before being fully ejected from surface by the surface acoustic waves on a ZnO substrate (input power of 28 W). The SAW generates from left to right; (c) vertical liquid droplet jetting based on standing wave based configuration by launching two waves from two IDTs; (d) liquid droplet jetting based on a circular IDT patterns from a ZnO/Si annular SAW device.

with the Rayleigh angle as shown in Fig. 3b. The leaky waves propagate inside the droplet and reach the surfaces of the deformed liquid and then are reflected back into the liquid, thus further pushing the liquid upwards (see Fig. 16). Vertical jetting of the droplet continues until the elongated liquid beam break up into small droplets (see Fig. 16). The liquid beam and the broken up droplets are ejected perpendicularly to the surface, in a similar manner to conventional nozzle-based droplet ejectors. These thin film SAW ejectors do not require a nozzle head and potentially offer a more cost-effective solution to the current inkjet technology. Pulsed RF signals can be applied to the two opposite IDTs to obtain fixed volume droplets ejected vertically, achieving similar performance of nozzle-based droplet ejectors. But this requires further investigation and optimization of device and operation.

Liquid droplet jetting can also be realised using a circular IDT pattern (see Fig. 15d at a low magnification). Fig. 17a shows the basic design of a circular IDT pattern. Fig. 17b and c demonstrate the jetting behaviour of a water droplet on a ZnO SAW device at different stages of the process. At the start, the large concentrated acoustic energy is dissipated into the droplet, inducing an inertial pressure to the centre of the fluid. The induced energy overcomes surface tension and produces a coherent thin and sharp cylindrical liquid column in the centre of the drop as shown in Fig. 17b. The energy is so concentrated that a cylindrical liquid column is ejected vertically from the droplet. This design has a higher energy efficiency than that using two opposite IDTs, but it is difficult to realise continuous droplet ejection as liquid needs to be transported to the centre of the device periodically whereas the two opposite IDT designs could have a microchannel being integrated to provide the liquid continuously.

When the droplet is positioned at the edge of two unaligned IDTs (see Fig. 17d), the droplet has been observed to be agitated and twisted at a low power as shown in Fig. 17e. If the power is large enough, the liquid droplet can be ejected from the device surface as shown in Fig. 17f. This configuration of droplet ejector requires even higher RF power to generate the droplet as a large proportional of the RF power will be lost and not be coupled into liquid.

7.1.4. Liquid nebulisation

If the applied RF power is sufficiently large and the device surface is hydrophilic, it is difficult to eject the whole droplet from the device surface, but small droplets with a volume ranging from a few femtolitres to a picolitre could be ejected. A

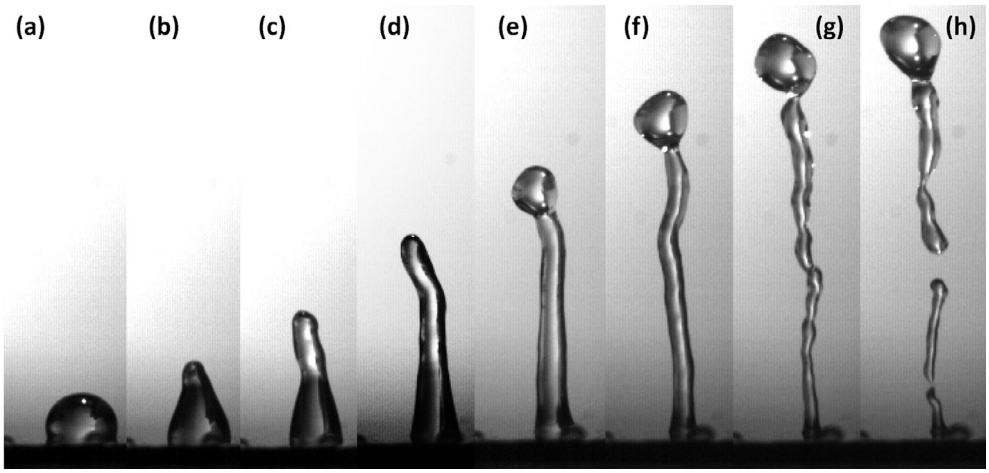

Fig. 16. Vertical liquid jetting of a 2 μL droplet actuated by ZnO/Si SAWs from two opposite IDTs. The SAWs are launched from two sides of the droplet, thus the droplet is pushed up from both sides by the opposing waves at the Rayleigh angle, i.e., (a) to (c). The leaky waves propagate inside the droplet and reach the surfaces of the deformed liquid and then are reflected back into the liquid, thus further pushing the liquid upwards, i.e., (c) to (f). The vertical jetting of the droplet continues until the elongated liquid beam break up into small droplets, i.e., (g) and (h).

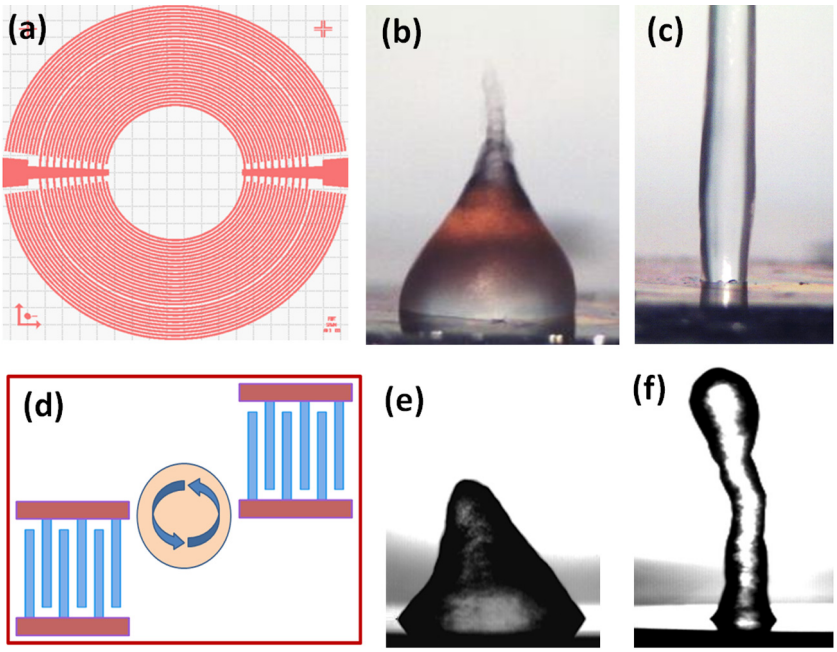

Fig. 17. (a) The schematic design of a circular IDT pattern with reflectors; (b) jetting behaviour of a water droplet on a ZnO SAW device at the initial stage, showing a large concentrated acoustic pressure to the centre of the fluid; (c) vertical jetting of the droplet forming a coherent thin and sharp cylindrical liquid column induced by a circular SAW; (d) illustration of a droplet positioned at the edge of two unaligned IDTs; (e) agitation and twisting of the water droplet at a low RF power for the situation in (d); (f) vertical jetting and twisting of liquid droplet at a high power.

large energy is required for the generation of small droplets as a continuous mist as shown in Fig. 18, *i.e.*, atomization or nebulisation. Atomization using thin film SAW devices is capable of producing aerosol droplets with a good particle size distribution due to the possible usages of a much higher frequency up to 100 MHz and a large RF power of 70 W, without damaging the device owing to high thermal conductivity of the Si-substrate [720]. Controlling the power of the RF signal applied to the IDTs enables the generation of droplets with a diameter smaller than 1 μm, which is suitable for pulmonary drug delivery and nanostructure or nanoparticle generation. The higher frequency and higher power enabled by ZnO thin film based SAW devices allows for the formation of much finer particles. Compared to bulk $LiNbO_3$ SAW devices, the thin film devices have a clear advantage in structural integrity. The SAW devices seldom break during microfluidic operations at high frequency and high power, and show a better performance and reliability.

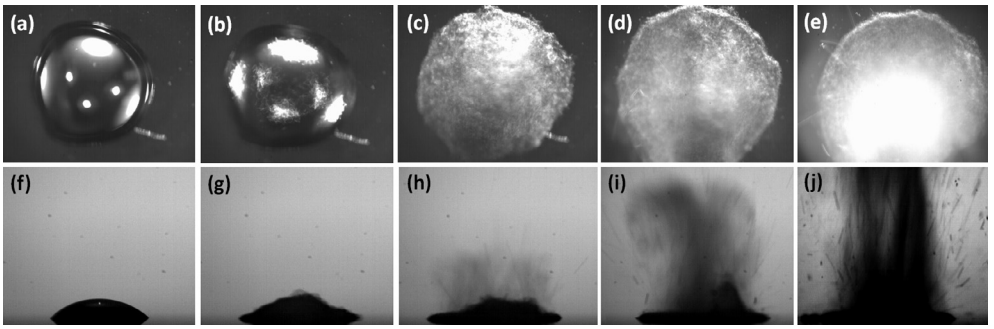

Fig. 18. Acoustic wave nebulisation on a ZnO SAW device: (a) to (e) top view of a typical nebulisation process; (f) to (j) cross-sectional view of successive nebulisation processes, including capillary formation, fine droplet formation, rising-up mist generated at a sufficiently high power and a hydrophilic device surface [721]

7.1.5. Particle and cell manipulation

Particle and cell manipulations in a microchamber or microchannels have also been easily achieved using a thin film SAW device with a pair or multiple IDT electrodes. The manipulation mechanisms are more or less similar to those presented in Fig. 3. Fig. 19 shows some examples of particle manipulation using the ZnO/Si SAW devices. Fig. 19a–c demonstrate the alignment of polysterene particles with an average size of 6 μm. The particles are aligned precisely in a microchannel of 300-μm width, at resonant frequencies of 11, 23 and 46 MHz. Fig. 19d shows the manipulation of fluorescence particles in a 500-μm microchannel and at a resonant frequency of 23 MHz.

Fig. 19e and f show the particles with different sizes of 6 μm and 2 μm being manipulated using phase angle control methods in a ZnO/Si SAW device at a frequency of 23 MHz. The different particles can be precisely controlled using the SAWs by precisely changing the phase angles. The migration of the two different types of particles slightly deviates from each other and this feature can be used to differentiate and sort the particles. Fig. 19g shows the formation of matrix of 6-μm particles inside a chamber manipulated using four IDTs to generate waves from two vertical directions.

Compared with conventional SAWs using a $LiNbO_3$ substrate, one advantage of thin film SAWs is that the shapes or patterns of the IDTs can be randomly designed without being affected by crystal orientations (as discussed in Section 5.2), thus providing flexibilities in complex manipulations of cells or particles on Si, glass or even flexible substrate.

7.2. Lamb wave and flexible microfluidics

A piezoelectric thin film allows for the fabrication of flexible acoustic wave devices. Early research focused on FPW or the A_0 mode of Lamb waves, which were mainly utilized for liquid transportation, pumping, agitation of a small liquid volume to

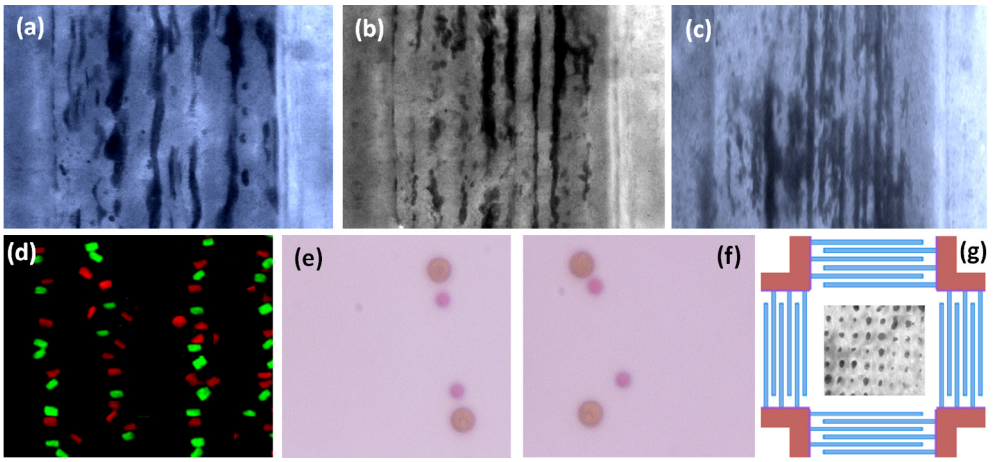

Fig. 19. Microparticle manipulation using the ZnO SAW devices; (a)–(c) demonstrate the alignment of polysterene particles with an average size of 6 μm. The particles were aligned precisely in a microchannel of 300-μm width, at resonant frequencies of 11, 23 and 46 MHz. (d) Manipulation of fluorescence particles in a 500-μm microchannel and at a resonant frequency of 23 MHz; (e and f) particles with different sizes of 6 μm and 2 μm being manipulated using phase angle control methods in a ZnO/Si SAW device at a frequency of 23 MHz. The different particles can be precisely controlled using the SAWs by precisely changing the phase angles. There is a slight deviation in the migration of the two different types of particles. (g) Formation of a matrix of 6-μm particles inside a chamber manipulated using four IDTs to generate waves from two vertical directions.

enhance biochemical reactions [722]. Fluid pumping was implemented with acoustic streaming induced by the travelling flexural waves in a ZnO or AlN piezoelectric membrane. The wave amplitude and the driving voltage are the critical parametres that control the flow rate.

The vibrating membrane acts as the acoustic source where the FPW induces acoustic streaming in the liquid. If the FPW contacts with the liquid, the slow mode of wave propagation can be used for pumping. Potential applications of acoustic streaming with the FPW include micro total analysis systems (μTAS), cell manipulating systems, and drug delivery systems [723]. However, the major drawback of FPW-based devices is the fragile actuating membrane. A microfluidic system with a thin membrane vibrating at a high frequency is not as robust as the SAW-based acoustic micropumps and mixers. Furthermore, the operation frequency is relatively low and consequently insufficient energy can be coupled into the liquid making pumping and mixing less effective. Therefore, recent reports in the literature on the research and the application of FPW-based microfluidics have been limited [724].

Flexible SAW devices, on the other hand, would be ideal for the development of flexible and disposable lab-on-chip applications. Flexible SAW on PI substrate has demonstrated similar microfluidic functions such as streaming, mixing and particle concentration, with one example shown in Fig. 20a. Although acoustic streaming speed is smaller than those found in SAWs on a rigid substrate such as $LiNbO_3$, it is still much larger than most fluidic flows delivered by other microfluidics such as micro-osmosis and microphoresis, and the particles uniformly distributed in the droplets can be concentrated in the middle of the droplet in a few tens of seconds, demonstrating their potential for applications [725].

Flexible substrates such as polymers dissipate most of the energy from the acoustic source, leading to a major attenuation of the wave. Other problems associated with polymeric substrates are poor film crystallinity and poor adhesion of the thin piezoelectric film. A solution for this problem is to use a thin metal foil as the substrate. Flexible acoustofluidics based on aluminium foil could provide efficient microfluidic functions with the resonant frequencies from both the Lamb wave mode and Rayleigh wave mode. Fig. 20b shows one example of droplet jetting behaviour on a ZnO/Al foil device with significant pre-bending of the Al foil, revealing the efficient microfluidic functions. As the wave-liquid interaction is different from the conventional Rayleigh waves, liquid transportation on the ZnO/Al foil device generally leads to significant vibration and deformation of the droplets.

7.3. Acoustic heating

A larger RF power applied to a SAW device could generate faster streaming, better mixing, faster pumping, as well as jetting and atomization. However, it can also induce localized heating due to the high-frequency induced mechanical vibration and stress generated in the substrate, the so-called acoustic heating which is a common phenomenon in SAW-based devices.

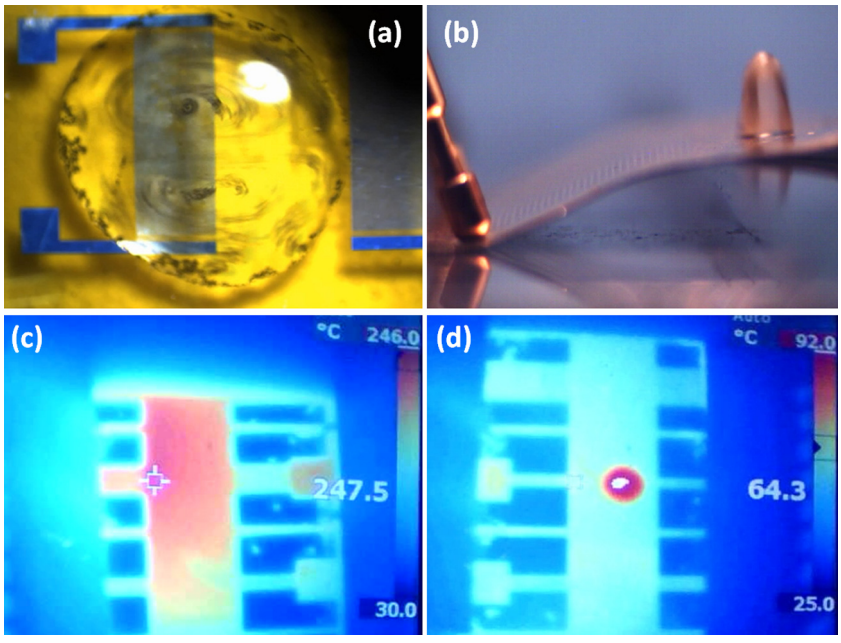

Fig. 20. (a) Flexible SAW microfluidic devices: a snapshot of acoustic streaming induced by the flexible SAW device on PI substrate, showing a double vortex streaming pattern. (b) A snap shot of one example of droplet jetting behaviour on a ZnO/Al foil device with significant pre-bending of the Al foil, revealing the efficient microfluidic functions. Temperature measurement on the surface of the ZNO/Si SAW devices; (d) surface temperature of the ZnO SAW device without any liquid droplet measured by an IR camera, reaching a maximum temperature of about 250 °C with an RF power of 36 W; (b) surface temperature of the a ZnO/Si SAW device with a droplet of 2 μL put on the surface of the ZnO SAW device. The signficant increase of temperature occurs mainly inside the water droplets before the evaporation of the droplet due to the signficant acoustic streaming effect and thermal conduction.

Rapid and controllable heating of microdroplets using SAWs have been reported using bulk $LiNbO_3$ SAW devices [726]. Acoustic heating could raise the temperature of the device substantially, and affect the performance of SAW resonators, acoustic streaming and pumping significantly. As the resonant frequency of SAW devices strongly depends on the operation temperature, it shifts when acoustic heating occurs. This will affect operation of electronics as well as the performance of acoustic streaming and pumping significantly [727,728].

Thin film SAW devices are efficient in generating high temperatures on device surfaces. As shown in Fig. 20c, the surface temperature of the ZnO SAW device without any liquid droplet measured by the IR camera increases with the RF power applied, and can reach to a maximum temperature of about 250 °C for an RF power of 36 W within 2 min (see Fig. 20c). Another phenomenon observed is that when a droplet of 2 μL was put on the surface of the ZnO SAW device, the surface temperature of the SAW device was much lower than that without water droplets as shown in Fig. 20d. The significant increase of temperature occurs mainly inside the water droplets (Fig. 20d), due to the significant acoustic streaming effect and thermal conduction. However, when the water droplet was ejected away or evaporated, the temperature of the SAW devices increases quickly to above 100 °C.

If heating is not desirable, the following approaches can be used to lower the surface temperature:

(1) Using substrates with a high thermal conductivity such as silicon or metal foils.
(2) Application of temperature compensated crystal substrates, such as SiO_2 (quartz) or $GaPO_4$.
(3) Compensation methods, such as layered designs using SiO_2 layer.
(4) Using a heat sink with high conductivity and capacity such as a metal block.

Although acoustic heating is not desirable in many applications, controlled acoustic heating is useful for biomedical applications such as PCR for DNA amplification for detection [729]. Controlled heating can also accelerate other bioreaction processes, speeding up detection and diagnosis process which are particularly important for on-site applications. The droplet-based SAW PCR system can avoid common problems of continuous-flow systems such as clogging, large pressure drop and evaporation. Furthermore, the induced acoustic streaming also helps to speed up biobinding reactions, resulting in a more homogeneous fluorescence signal. Thin film SAW based acoustic streaming has been intensively studied, but related thin film SAW PRC for DNA amplification, as well as acoustic heating induced accelerated biochemical reactions have not been reported to date.

8. Summary and future trends

8.1. Summary

The present review discusses the recent developments on preparation and application of ZnO and AlN films for lab-on-chip, acoustofluidics and biosensors. Both ZnO and AlN films are promising materials for the fabrication of fully automated and digitized microsystems with compactness, simple operation, precision, low cost, fast response, and reduced reagent requirement. This type of microsystem has multiple functions, yet it can be operated by a single acoustic wave mechanism, a unique characteristic no other microsystem can achieve. High quality and strongly textured piezoelectric thin films can be prepared using RF magnetron sputtering. Their microstructure, texture and piezoelectric properties are determined by the sputtering conditions such as target power, gas pressure, substrate material and temperature as well as film thickness.

ZnO or AlN acoustic wave devices have been successfully used to fabricate biosensors which can be combined with affinity binding and biomolecule recognition systems to detect traces of biomolecules associated with certain types of diseases and illnesses. Among these biosensors, high-frequency SAWs, Love-mode and film bulk acoustic resonator devices (with or without inclined films) are promising for applications in highly sensitive bio-detection systems for both dry and liquid environments with high sensitivities and low detection limits. FBARs have a small footprint and can be fabricated on the same substrate as those SAW devices, allowing the fabrication of a FBAR sensor array for multi-parameter detection with microfluidics integrated on the same chip, which can significantly improve the diagnostic speed of a disease or allow detection of multiple diseases in parallel.

The acoustic waves generated on the ZnO or AlN acoustic devices can induce significant acoustic streaming with velocity much faster than those delivered by most of other microfluidic systems. The strong acoustic streaming can be employed for mixing, pumping, ejection and atomization of the fluid on the small scale depending on the wave mode, amplitude and surface condition. An integrated lab-on-a-chip diagnostic system with combined functions of sample preparation, microfluidics and biosensors is critical for detection illnesses at their early stage, preventing the spread of pandemic diseases and enabling a swift response to biological terrorist attack. Further functions such as droplet formation and cell sorting can also be obtained from or integrated with thin film acoustic wave technology. We foresee that such microsystems are capable of performing the complete task from delivering drops of bio-sample into the device through to the delivery of the detection results.

Thin film acoustic wave technology has many advantages over its counterpart using piezoelectric bulk materials. The most important and unique ones are the possibility of integration of acoustic wave devices and functions with electronics for control and signal processing, fabrication of acoustic devices and function with no constraint on crystal orientation,

capability to control and tune temperature coefficient of frequency, fabrication of thin film based FBAR, SMR arrays with highest sensitivity for multiple detection and monitoring, and the possibility to fabricate flexible and transparent acoustic wave based devices and platforms.

8.2. Future trends

8.2.1. Integration

8.2.1.1. Integration with new materials. Much recent work has reported the combination of advanced thin film SAWs with novel sensing materials such as metal nanoparticles, ZnO nanowires, carbon nanotubes or even graphene for the fabrication of new generation highly sensitive sensors [730–732]. For example, ZnO nanostructures, especially ZnO nanowires, have been shown to be an attractive candidate for precision sensing of biomolecules. These nanostructures offer a significantly increased sensing area, faster response, and higher sensitivities over planar sensor configurations, and additional functions such as surface plasmon, bioactive surfaces or biobinders for specific target molecules, so that new biodetection methods can be developed. From the commercialization point of view, this is a very promising but an under-studied topic with a huge market potential. The selectivity and sensitivity of ZnO nanowires can be improved by surface modifications or doping.

8.2.1.2. Integration with CMOS and other acoustic wave technologies. Thin film acoustic wave devices can readily be integrated with standard MEMS and CMOS technologies. Integration on CMOS chips could greatly reduce the cost and footprint of the chip and improve the microsystem performance with less noise and human interference, whereas integration with other MEMS would greatly increase the functionality of the microsystems. Dual or multiple SAW devices or an array of FBAR devices can be integrated and fabricated adjacent to each other, so that the neighbouring devices can be used as reference sensors. One of the devices without pre-deposited probe molecules can be used as a reference, with the other ones with probe molecules being used to sense. An additional device can also be used as a calibration device for temperature, humidity, etc., for the sensor as well as the microsystem. Such combinations can minimise the errors caused by temperature drift or other interference on the measurement. Multi-sensor arrays can easily be prepared on a chip and a judicious selection of different immobilized bio-binders enables the simultaneous detection of multiple DNA or proteins, leading to accurate diagnosis of a disease or detection of multiple diseases in parallel. The creation of these cost-effective sensor arrays with integrated CMOS driving/sensing electronics can increase the functionality in real time and provide parallel reading functions.

8.2.1.3. Integration with other microfluidic and sensing technologies. ZnO or AlN based acoustic wave technologies can be integrated with other technologies, such as surface plasma resonance and optical sensors. SPR sensor technology has been commercialized with SPR biosensors becoming a major tool for characterizing and qualifying bimolecular interactions. The detection principle of the SPR sensors lies in the changes in the refractive index due to the biomolecules interaction or formation of a new layer near the surface. A combination of SAW microfluidics and SPR sensing would be viable for both microfluidic and detection functions [733–736]. Besides the SAW microfluidics, SAW sensors could also be integrated with SPR sensors to form a platform with multiple sensing technologies. For *in-situ* measurements in a solution, label-free detection and real-time monitoring, SAW sensors do not compete with but are complementary to the SPR technology. The main advantage of the SAW sensors over the SPR sensors is their capability in sensing changes in other variables such as density, mass and viscosity. The integration of SAW microfluidics could also speed up the specific biobinding and eliminate non-specific biobinding, thus increasing the detection speed and improving the accuracy of the SPR sensors. The same principle could apply to other optical biosensors based on the change of reflection, refraction, diffraction to improve the detection speed and accuracy.

There are other types of integration of a SAW with optical methods, *i.e.*, optoacoustic integration. One of the examples is the cell manipulation using the opto-thermally generated bubbles which can be activated and manipulated using acoustic waves. Generation of surface bubbles can be controlled by laser power and positions. The cells are manipulated using the acoustic radiation forces generated from the acoustic waves to the surface bubble arrays [737].

The integration of SAW and DEP can be used to realise precise particle manipulation and cell manipulation [738–740]. A further example is the integration of acoustic wave manipulation and impedimetric sensing [741]. ZnO and AlN based acoustic wave microfluidic devices can be combined with liquid or gas chromatography, which is then used to identify the protein or molecules by mass spectroscopy [742]. Thin film SAW devices can be easily integrated with ZnO-based phononic crystal structures, which shape the deformation of liquid droplets as reported by Reboud et al. using the bulk $LiNbO_3$ SAW [743].

Digital microfluidics is the foundation for digital diagnosis and digital medicine. For digital microfluidics, there is a need to precisely and continuously generate droplets of biosamples and reagents with fixed volumes for analysis and detection. ZnO and AlN acoustic wave technology can be used to control the formation process of liquid droplets. In the past ten years, electrowetting on dielectrics (EWOD) technology has been successfully developed to dispense and transport nanolitre to microlitre bio-samples in droplet forming the volumes required [744]. However, one of the weaknesses of EWOD technology is that it does not provide efficient mixing, and requires the integration of other technologies, e.g. CMOS, to realise bioreaction and biosensing. A novel idea is to integrate the thin film SAW devices with the EWOD device to form a lab-on-a-chip equipped with functionalities of droplet generation, transportation by EWOD and mixing/biosensing by SAW [745]. Integration of EWOD and FBAR has also been proposed recently [746]. On the other hand, pulsed RF signals could be utilized

on SAW to generated droplets with fixed volumes through a nozzle-like structure on planar surface. This technique will provide a mechanism to develop fully digitized lab-on-a-chip systems, but is yet to be developed.

8.2.2. Portable, wireless, flexible and remotely controlled devices

Currently, one limitation of acoustic wave devices is that they require expensive electronic detection systems, such as network analysers. A final product aimed at the end user market must be small, portable and packaged into a highly integrated and cost-effective system. The detection of a resonant frequency can be easily realised using standard oscillator circuits on a portable device. The fabrication of portable thin film based acoustic wave detection devices provides the option to enable the system size to be minimised along with reduced power consumption. As SAW devices can be wirelessly interrogated, SAW-based lab-on-a-chip systems can be wirelessly powered and controlled for physical, chemical and biological sensing and quantitative detection, providing a system that does not require a directly wired power supply. Unlike silicon based Radio Frequency Identification (RFID) tags which need significant incoming power to reach the threshold voltage of a rectifying diode, all piezoelectric processes are linear and thus the interrogation range is only limited by the receiver noise [747]. As the operating frequency of the SAW devices is much higher than those of inductor/capacitor based RF wireless communication system, SAW based lab-on-a-chip wireless detection system can have a long-working distance. The hardware, operating following the strategies of frequency-swept pulse-mode monostatic radar, are controlled by digital electronics to implement adaptive frequency generation dependent on the signals returned by the acoustic wave sensor [748–750].

The nonlinear interaction between SAWs, liquids and particles is yet to be studied in depth. There is still a lack of quantitative studies and numerical analyses on this aspect of the technology. Secondly, the liquid used in most SAW applications reported is of a single phase. Multi-phase SAW platforms could be of interest in many applications and are worthy of further exploration. The evaporation of droplets over time is the main hindrance in some systems where long sample processing times or heating are required. Some environmental perturbations still need to be overcome such as the temperature, humidity, optical response and the vibration from the holders.

8.2.3. Theoretical analysis and new theory?

The coupling mechanism of the acoustic wave with fluids is sensitive to the deformation of the interface, which is difficult to predict. Hence, an accurate interpretation of the interaction between the SAW and fluids is an important topic to be further developed to aid the design of novel microfluidic devices. Mathematical modelling and simulations of these devices are essential for the development of new sensors, especially with respect to the study of new materials and wave propagation.

Numerical calculations and finite element or finite volume analysis of acoustic wave sensors could also help with the development and understanding of the piezoelectricity of materials, as well as doping functions, operation mechanisms of devices, vibration wave patterns, etc. [751–754]. Density function theory (DFT) and first principle calculations should be used to study the fundamental doping mechanisms of elements for improving piezoelectric properties of new thin film materials [755,756].

Acknowledgement

The authors acknowledge support from the Innovative electronic Manufacturing Research Centre (IeMRC) through the EPSRC funded flagship project SMART MICROSYSTEMS (FS/01/02/10), Knowledge Transfer Partnership No KTP010548, EPSRC project EP/L026899/1, EP/F063865/1; EP/F06294X/1, EP/P018998/1, the Royal Society-Research Grant (RG090609) and Newton Mobility Grant (IE161019) through Royal Society and NFSC, the Scottish Sensing Systems Centre (S3C), Royal Society of Edinburgh, Carnegie Trust Funding, Royal Academy of Engineering-Research Exchange with China and India, UK Fluidic Network and Special Interest Group-Acoustofluidics, the EPSRC Engineering Instrument Pool. We also acknowledge the National Natural Science Foundation of China (Nos. 61274037, 51302173), the Zhejiang Province Natural Science Fund (No. Z11101168), the Fundamental Research Funds for the Central Universities (No. 2014QNA5002), EP/D03826X/1, EP/C536630/1, GR/T24524/01, GR/S30573/01, GR/R36718/01, GR/L82090/01, BBSRC/E11140. ZXT acknowledges the supports from the National Natural Science Foundation of China (61178018) and the NSAF Joint Foundation of China (U1630126 and U1230124) and Ph.D. Funding Support Program of Education Ministry of China (20110185110007) and the NSAF Joint Foundation of China (Grant No. U1330103) and the National Natural Science Foundation of China (No. 11304209). NTN acknowledges support from Australian Research Council project LP150100153. This work was partially supported by the European Commission through the 6th FP MOBILIS and 7th FP RaptaDiag project HEALTH-304814 and by the COST Action IC1208 and by the Ministerio de Economía y Competitividad del Gobierno de España through projects MAT2010-18933 and MAT2013-45957R. All previous students, researchers and collaborators, including Dr. Xiaoye Du, Dr. Hua Feng Pang, Dr. Luis Garcia-Gancedo, Dr. Gregory Ashley. Dr. Xiubo Zhao, Dr. Jia Zhang, Dr. Jian Zhou, Dr. Xingli He, Dr. Yuanjun Guo, Dr. Chao Zhao, Dr. Wenbo Wang, Dr. Weipeng Xuan, Dr. Jinkai Chen, Dr. Mansuor Alghane, Dr. Baixin Chen, Yong Liu, Sam Hasan, Dr. Zhijie Li, Dr. M. DeMiguel-Ramos, Dr. Stuart Brodie, Dr. Sam Porro, Prof. Jonathan Cooper, Dr. Julien Rebond, Dr. Robert Wilson, Dr. Jingting Luo, Prof J.T.M. Stevenson, Dr A. Bunting, Dr J.G. Terry, A.M. Gundlach, Dr. Michael I. Newton and Dr. Electra Gizeli are specially acknowledged.

References

[1] Mark D, Haeberle S, Roth G, von Stetten F, Zengerle R. Chem Soc Rev 2010;39:1153–82.

[2] Gopinath SCB, Tang TH, Citartan M, Chen Y, Lakshmipripa T. Biosens Bioelectron 2014;57:292–302.
[3] Dittrich PS, Manz A. Nat Rev Drug Discov 2006;5:210–8.
[4] Nguyen NT, Huang X, Chuan TK. J Fluids Eng 2002;124:384–92.
[5] Laser DJ, Santiago JG. J Micromech Microeng 2004;14:R35.
[6] Ong SE, Zhang S, Du HJ, Fu YQ. Front Biosci 2008;13:2757–73.
[7] Cho SK, Moon H, Kim C-J. J Microelectromech Syst 2003;12:70–80.
[8] Lacharme F, Gijs MA. Sensors Actuat A 2006;117:384–90.
[9] Darabi J, Rada M, Ohadi M, Lawler JJ. Microelectomech Syst 2002;11:684–90.
[10] Jones TB. J Electrostat 2001;51(52):290–9.
[11] Pollack MG, Fair RB, Shenderov AD. Appl Phys Lett 2000;77:1725.
[12] Pollack MG, Shenderov AD, Fair RB. Lab Chip 2002;2:96–101.
[13] Mugele F, Herminghaus S. Appl Phys Lett 2002;81:2303.
[14] Wixforth AJ. Automach Lab Automat 2006;11:399–405.
[15] Destgeer G, Sung HJ. Lab Chip 2015;15:2722–38.
[16] Barani A, Paktinat H, Janmaleki M, Mohammadi A, Mosaddegh P, Fadaei-Tehrani A, et al. Biosens Bioelectron 2016;85:714–25.
[17] Cote GL, Lec RM, Pishko MV. IEEE Sens J 2003;3:251–66.
[18] Friend R, Yeo LY. Rev Modern Phys 2011;83:647–704.
[19] Yeo LY, Friend JR. Biomicrofludics 2009;33:012002.
[20] Yeo LY, Friend JR. Annu Rev Fluid Mech 2014;46:379–406.
[21] Vellekoop MJ. Ultrasonics 1998;36:7–14.
[22] Galipeau DW, Story PR, Vetelino KA, Mileham RD. Smart Mater Struct 1997;6:658–67.
[23] Lakin KM. Thin film resonator technology. IEEE Trans Ultrason, Ferroelect, Freq Contr 2005;52:707–15.
[24] Campanella H, Esteve J, Montserrat H, Uranga A, Abadal GBarniol N, Romano-Rodrigeuz A. Appl Phys Lett 2006;89:33 507.
[25] Du J, Harding GL, Collings AF, Dencher PR. Sens Actuat A 1997;60:54–61.
[26] Ballantine DS, White RM, Martin SJ, Ricco AJ, Zellers ET, Frye GC, et al. Acoustic wave sensors: theory, design, and physico-chemical applications. San Diego: Academic Press; 1997.
[27] Campbell CK. Surface acoustic wave devices for mobile and wireless communications. San Diego: Academic Press Inc; 1998.
[28] Gizeli E, Stevenson AC, Goddard NJ, Lowe CR. IEEE Trans Ultrason Ferroelect Freq Control 1992;39:657.
[29] Kovacs G, Venema A. Appl Phys Lett 1992;1992(61):639.
[30] Martin SJ, Ricco AJ, Niemczyk TM, Frye GC. Sens Actuat 1989;20:253.
[31] Rocha-Gaso MI, March-Iborra C, Montoya-Baides A, Aranau-Vives A. Sensors 2009;9:5740–69.
[32] Kanazawa KK, Gordon JG. Anal Chem 1985;57:1770–1.
[33] Buttry DA, Ward MD. Chem Rev 1992;92:1355–79.
[34] Redwood MR. Mechanical waveguides. Oxford: Pergamon Press; 1960.
[35] Duhamel R, Robert L, Jia H. Ultrasonics 2006;44:E893–7.
[36] Dickherber A, Corso CD, Hunt WH. Sens Actuat A 2008;144:7–12.
[37] Chen D, Xu Y, Wang J, Zhang L, Wang X, Liang M. Vacuum 2010;85:302–6.
[38] Lakin KM, Wang JS. Appl Phys Lett 1981;38:125.
[39] Pang W, Zhao H, Kim ES, Zhang H, Yu H, Hu X. Lab Chip 2012;12:29–44.
[40] Grate WJ, Wenzel SW, White RM. Anal Chem 1991;63:1552–61.
[41] Lamb H. Proc R Soc A 1917;93:114–28.
[42] Muralt P, Ledermann N, Baborowski J. IEEE Trans Ultrason Ferroelect Freq Control 2005;52:2276–88.
[43] White RM, Wenzel SW. Appl Phys Lett 1988;52:1653–5.
[44] Moroney RM, White RM, Howe RT. Appl Phys Lett 1991;59:774–6.
[45] Sezawa K, Kanai K. Bull Earthquake Res Inst 1935;13:237–43.
[46] Barie N, Rapp M. Biosens Bioelectron 2001;16:979–87.
[47] Kovacs G, Venema M. Appl Phys Lett 1992;61:639.
[48] Josse F, Bender F, Cernosek RW. Anal Chem 2001;73:5937.
[49] Lindner G. J Phys D 2008;41:123002.
[50] Pedros J, Calle F, Grajal J, et al. Phys Rev B 2005;72:075306.
[51] McHale G, Newton MI, Martin F. J Appl Phys 2003;93:675–90.
[52] McHale G, Newton MI, Banerjee MK, Cowen JA. Mater Sci Eng C 2000;12:17–22.
[53] McHale G, Banerjee MK, Newton MI, Krylov VV. Phys Rev B 1999;59:8262–70.
[54] Gizeli E, Bender F, Rasmusson A, Saha K, Josse F, Cernosek R. Biosens Bioelectron 2003;18:1399–406.
[55] McHale G. Meas Sci Technol 2003;14:1847–53.
[56] Brodie S, Fu YQ, Li Y, Alghane M, Walton A. Appl Phys Lett 2011;99:153704.
[57] Jakubik WP. Thin Solid Films 2011;520:986–93.
[58] Grate WJ, Martin SJ, White RM. Anal Chem 1993;65:940A–8A.
[59] Kuznestsova LA, Coakley WT. Biosens Bioelectron 2007;22:1567–2577.
[60] Teles FRR, Fonseca LP. Talanta 2008;77:606–23.
[61] Shiokawa S, Kondoh J. J Jap Appl Phys 2004;43:2799–802.
[62] Greve DW, Chin TL, Zheng P, Ohodnicki P, Baltrus J, Oppenheim IJ. Sensors 2013;13:6910–35.
[63] Afzal A, Iqbal N, Mujahid A, Schirhagl R. Anal Chim Acta 2013;787:36–49.
[64] Groewold TMA. Anal Chim Acta 2007;603:119–28.
[65] Lange K, Rapp B, Rapp M. Anal Bionanal Chem 2008;391:1509–19.
[66] Hoummady M, Camitelli A, Wlodarski W. Smart Mater Struct 1997;64:647–57.
[67] Sauerbrey GZ. Z Phys 1959;155:206.
[68] Bruckenstein S, Shay M. Electrochim Acta 1985;30:1295.
[69] Kanazawa KK, Gordon JG. Anal Chim Acta 1985;175:99.
[70] Weinberg MS, Cunningham BT, Clapp CW. J Microelectromech Syst 2000;9:370–9.
[71] Rey-Mermet S, Bjurstrom J, Rosen D, Petrov I. IEEE Trans Ultrason Ferroelect Freq Control 2004;51:1347–53.
[72] Chen Q, Wang QM. Appl Phys Lett 2005;86:022904.
[73] Hara M, Kuypers J, Abe T, Esahi M. Sens Actuat A 2005;117:211–6.
[74] Sritharan K, Strobl CJ, Schneider MF, Wixforth A, Guttenburg Z. Appl Phys Lett 2006;88:054102.
[75] Shoji S, Esashi M. J Micromech Microeng 1994;4:157–4171.
[76] Shilton R, Tan MK, Yeo LY, Friend JR. J Appl Phys 2009;104:014910.
[77] Wixforth A, Strobl C, Gauer C, Toegl A, Scriba J, Guttenberg ZV. Anal Bioanal Chem 2004;379:982.
[78] Chono K, Shimizu N, Matsu Y, Kondoh J, Shiokawa S. Jap J Appl Phys 2004;43:2987–91.
[79] Murochim N, Sugimoto M, Matui Y, Kondoh J. Jap J Appl Phys 2007;46:4754–9.

[80] Toegl A, Kirchner R, Gauer C, Wixforth A. J Biomed Technol 2003;14:197–204.
[81] Newton MI, Banerjee MK, Starke TK, Bowan SM, McHale G. Sensor Actuat 1999;76:89–92.
[82] Nyborg WL. In: Hamilton MF, Blackstock DT, editors. Acoustic streaming Nonlinear Acoustics. New York: Academic; 1998. p. 207–331.
[83] Rotter M, Kalameitsev AV, Govorov AO, Ruile W, Wixforth A. Phys Rev Lett 1999;82:2171–4.
[84] Renaudin A, Tabourier P, Camart JC, Druon C. J Appl Phys 2006;100:116101.
[85] Renaudin A, Tabourier P, Zhang V, Camart JC, Druon C. Sens Actuat B 2006;113:389–91.
[86] Du XY, Fu YQ, Tan SC, Luo JK, Flewitt AJ, Maeng S, et al. J Phys: Conf Ser 2007;76:012035.
[87] Toegl A, Scribe J, Wixforth A, Strobl C, Gauer C, Guttenburg ZV. Anal Bioanal Chem 2004;379:982–91.
[88] Franke T, Wixforth A. Chem Phys Chem 2008;9:2140.
[89] Wixforth A. Superlatt Microstruct 2004;33:389–98.
[90] Shiokawa S, Matsui Y, Morizum T. Jpn J Appl Phys 1989;28:126.
[91] Alghane M, Fu YQ, Li Y, Luo JK, Bobbili B, Feng Y, et al. J Microeng Micromech 2011;21:015005.
[92] Schmid L, Wixforth A, Weitz DA, Franke T. Microfluid Nanofluid 2012;12:229–35.
[93] Frommelt T, Gogel D, Kostur M, Talkner P, Hanggi P. IEEE Transact Ultrason, Ferroelect Freq Control 2008;55:2298–305.
[94] Gao Y, Tran P, Petkovic-Duran K, Swallow T, Zhu YG. Biomed Microdev 2015;17:79.
[95] Boon WC, Petkovic-Duran K, White K, Tucke E, Albiston A, Marasseh R, et al. Biotechniques 2011;50:116–9.
[96] Fu YQ, Luo JK, Du XY, Flewitt AJ, Li Y, Walton AJ, et al. Sens Actuat B 2010;143:606.
[97] Yeo LY, Friend JR, McIntosh MP, Meeusen EN, Morton DA. Expert Opin Drug Del 2010;7:663–79.
[98] Heron SR, Wilson R, Shaffer SA, Goodlett DR, Cooper JM. Anal Chem 2010;82:3985–9.
[99] Qi A, Friend JR, Yeo LY, Morton DA, McIntosh MP, Spiccia L. Lab Chip 2009;9:2184–93.
[100] Rajapaksa A, Qi A, Yeo LY, Coppel R, Friend JR. Lab Chip 2014;14:1858–65.
[101] Collins DJ, Manor O, Winkler A, Schmidt H, Friend JR, Yeo LY. Phys Rev E 2012;86:056312.
[102] Tveen-Jensen K, Gesellchen F, Wilson R, Spickett CM, Cooper JM, Pitt AR. Sci Rep 2015;5:9736.
[103] Reboud J, Wilson R, Zhang Y, Ismail MH, Bourquin Y, Cooper JM. Lab Chip 2012;12:1268–73.
[104] Ho, Tan MK, Go DB, Yeo LY, Friend JR, Chang H-C. Anal Chem 2011;83:3260–6.
[105] Winkler A, Harazim SM, Menzel SB, Schmidt H. Lab Chip 2015;15:3793–9.
[106] Ang KM, Yeo LY, Friend JR, Hung YM, Tan MK. J Aerosol Sci 2015;79:48–60.
[107] Qi A, Yeo LY, Friend JR. Phys Fluids 2008;20:074103–74114.
[108] Tan MK, Friend JR, Yeo LY. Phys Rev Lett 2009;103:024501.
[109] Sesen M, Alan T, Neild A. Lab Chip 2015;15:30303038.
[110] Brenker JC, Collins DJ, Phan HV, Alan T, Neild A. Lab Chip 2016;16:1675.
[111] Chong ZZ, Tan SH, Ganan-Calvo AM, Tor SB, Loh NH, Nguyen NT. Lab chip 2016;16:35–58.
[112] Shi JJ, Ahmed D, Mao XL, Lin SCS, Lawit A, Huang TJ. Lab Chip 2009;9:2890.
[113] Laurell T, Petersson F, Nilsson A. Chem Soc Rev 2007;36:492.
[114] Jo MC, Guldiken R. Sens Actuat A 2014;207:39–42.
[115] Meng L, Cai FY, Zhang ZD, et al. Biomicrofluidics 2011;5:044144.
[116] Destgeer G, Sung HJ. Lab Chip 2015;15:2722–38.
[117] Ding XY, Lin SCS, Kiraly B, Yue HJ, Li SX, Chiang IK, et al. PNAS 2012;109:11105–9.
[118] Nilsson J, Evonder M, Hammarstrom B, Laurell T. Anal Chim Acta 2009;649:141–57.
[119] Gedge M, Hill M. Lab Chip 2012;12:2998–3007.
[120] Weigel R, Morgan DP, Owens JM, Ballato A. IEEE Trans Microwave Theory Technol 2002;50:738–49.
[121] Sigh R, Sankaranarayanan SKRS, Bhethanabotla VR. Appl Phys Lett 2009;94:265503.
[122] Wingqvist G. Surf Coat Technol 2010;205:1279–86.
[123] Du XY, Fu YQ, Tan SC, Luo JK, Flewitt AJ, Milne WI, et al. Appl Phys Lett 2008;93:094105.
[124] Jin H, Zhou J, He XL, Wang WB, Guo HW, Dong SR, et al. Sci Rep 2013;3:2140.
[125] Laurenti M, Stassi S, Lorenzoni M, Fontana M, Canavese G, Cauda V, et al. Nanotechnology 2015;26:215704.
[126] Smecca E, Maita F, Pellegrino G, Vinciguerra V, Magna LL, Mirabella S, et al. Appl Phys Lett 2015;106:232903.
[127] Mastronardi VM, Ceseracciu L, Guido F, Rizzi F, Athanassiou A, De Vittorio M, et al. Appl Phys Lett 2015;106:162901.
[128] Du XY, Fu YQ, Luo JK, Flewitt AJ, Milne WI. J Appl Phys 2009;105:024508.
[129] Muralt P. IEEE Trans Ultrason, Ferroelect, Freq Control 2000;47:903–15.
[130] Harris NR, Hill M, Torah R, Stavrinidis A, Stefanescu A, Stavrinidis G, et al. Sens Acutaut A 2006;132:311–6.
[131] Watermore RW, Zhang Q, Huang Z, Dorey RA. Mater Sci Semiconduct Process 2003;5:65–76.
[132] Khan A, Abas Z, Kim HS, Oh IK. Smart Mater Struct 2016;25:053002.
[133] Muralt P. J Am Ceram Soc 2008;91:1385–96.
[134] Muller A, Konstantinidis G, Buiculescu V, Dinescu A, et al. Sens Actuat A 2014;209:115–23.
[135] Muller A, Giangu I, Stavrindis A, Stefanescu A, Stavrinidis G, Dinescu A, et al. IEEE Electron Dev Lett 2015;36:1299–302.
[136] Stefanescu A, Muller A, Giangu I, Dinescu A, Konstantindis G. IEEE Electr Dev Lett 2016;37:321–4.
[137] Pantazis AK, Gizeli E, Konstantindis G. Appl Phys Lett 2010;96:194103.
[138] Lu X, Lee CM, Wu SY, Ho HP, Lau KM. IEEE Sens J 2012;13:1245–51.
[139] Pantazis AK, Konstantindis G, Gizeli E. IEEE Sens J 2014;14:908–11.
[140] Lam HK, Dai JY, Chan HLW. J Cryst Growth 2004;268:144–8.
[141] Saddik GN, Boesch DS, Stemmer S, York RA. Appl Phys Lett 2007;91:0435901.
[142] Kadota M, Ogami T, Yamamoto K, Tochishita H, Negoro Y. IEEE Trans Ultrason, Ferro Freq Control 2010;57:2564–71.
[143] Kadota M, Ogami T, Yamamoto K, Tochishita H. Phys Stat Solidi A 2011;208:1068.
[144] Zhou C, Yang Y, Zhan J, Ren T, Wang X, Tian S. Appl Phys Lett 2011;99:022109.
[145] Vorobiev A, Loffler M, Olsson E, Gevorgian S. J Appl Phys 2014;115:084105.
[146] Chen J, Zhang Q, Hao T, Zhou L, Tang G, Liu B, et al. AIP Adv 2015;5:087173.
[147] Ozgur U, Hofstetter D, Morkoc H. Proc IEEE 2010;98:1255–68.
[148] Klingshrin C. Phys Stat Sol B 2007;244:3027–73.
[149] Yoshino Y. J Appl Phys 2009;105:061623.
[150] Fan L, Zhang SY, Ge H, Zhang H. J Appl Phys 2013;114:024504.
[151] Wu TT, Wang WS. J Appl Phys 2004;96:5249.
[152] Arya SK, Saha S, Ramirez-Vick JE, Gupta V, Bhansali S, Singh SP. Anal Chim Acta 2012;737:1–21.
[153] Wei A, Pan L, Huang W. Mater Sci Eng B 2011;176:1409–21.
[154] Phan DT, Chung GS. J Electroceram 2013;30:185–90.
[155] Hong HS, Phan DT, Chung GS. Sens Acuat B 2012;171–172:1283–7.
[156] Cong GW, Wei HY, Zhang PF, Peng WQ, Wu JJ, Liu XL, et al. Appl Phys Lett 2005;87:231903.
[157] Hou RZ, Hutson D, Kirk KJ, Fu YQ. J Appl Phys 2012;111:148207.
[158] Aubert T, Bardong J, Legrani Q, Elmazria O, Assouar MB, Bruckner G, et al. J Appl Phys 2013;114:014505.

[159] Olivares J, Iborra E, Clement M, Vergara L, Sangrador J, Sanz-Hervás A. Sensors Actuat A 2005;123–124:590–5.
[160] Piazza G, Felmestsger V, Muralt P, Olsson III RH, Ruby R. MRS Bull 2012;37:1051–61.
[161] Hernando J, Sánchez-Rojas JL, González-Castilla S, Iborra E, Ababneh A, Schmid U. J Appl Phys 2008;104:053502.
[162] Ch Kaletta U, Santos PV, Wolansky D, Scheit A, Fraschke M, Wipf C, et al. Semiconduct Sci Technol 2013;28:065013.
[163] Iborra E, Olivares J, Clement M, Vergara L, Sanz-Hervás A, Sangrador J. Sensors Actuat 2004;115:501–7.
[164] Caliendo C, Imperatori P. Appl Phys Lett 2003;83:1641–3.
[165] Olivares J, González-Castilla S, Clement M, Sanz-Hervás A, Vergara L, Sangrador J, et al. Diamond Related Mater 2007;16:1421–4.
[166] Campanella H, Uranga A, Romano-Rodriguez A, et al. Sens Actuat B 2008;142:322–8.
[167] Clement M, Vergara L, Sangrador J, Iborra E, Sanz-Hervás A. Ultrasonics 2004;42:403–7.
[168] Loebl HP, Klee M, Metzmacher C, Brand W, Milsom R, Lok P. Mater Chem Phys 2003;79:143–6.
[169] Chiu KH, Chen JH, Chen HR, Huang RS. Thin Solid Films 2007;515:4819–25.
[170] Shih WC, Zoh ZX. Ferroelectrics 2014;459:52–62.
[171] Neculoiu D, Muller A, Deligeorgis G, Dinescu A, Starrinidis A, Vasilache D, et al. Electron Lett 2009;45(1196–119):7.
[172] Kaletta UC, Wipf C, Fraschke M, Wolansky D, Schubert MA, Schroader T, et al. IEEE Trans Elect Dev 2015;62:764–8.
[173] Spina LL, Iborra E, Schellevis H, Clement M, Olivares J, Nanver LK. Solid-State Electron 2008;52:1359–63.
[174] Lee JB, Cho DH, Kim DY, Park CK, Park JS. Thin Solid Films 2007;516:475–80.
[175] Yong KK, Yu SF. J Mater Sci 2012;47:5341–60.
[176] Andrei A, Jozwik K, Delobelle P, Delobelle P, Hirsinger L, Gorecki C, et al. Sens Actuat A 2008;141:565–76.
[177] Krupa K, Jozwik M, Gorecki C, Andrei A, Nieradko L, Delobelle P, et al. Opt Laser Eng 2009;47:211–6.
[178] Piazza G, Stephanou PJ, Pisano AP. J MEMS 2006;15:1406–8.
[179] Piazza G, Stephanou PJ, Pisano AP. J MEMS 2007;16:319–28.
[180] Zuo C, Sinha N, Van der Spiegel J, Piazza G. J MEMS 2010;19:570–80.
[181] Lin CM, Yen TT, Lai YJ, Felmestger VV, Hopcroft MA, Kuypers JH, et al. IEEE Trans Ultrason Ferroelect Freq Control 2010;57:524–32.
[182] Wang Y, Wasa K, Zhang SY. IEEE Trans Ultrason Ferroelect Freq Control 2012;59:1613–7.
[183] Wang Y, Zhang SY, Fan L, Shui XJ, Zhang ZN, Wasa K. IEEE Trans Ultrason Ferroelect Freq Control 2013;60:1213–8.
[184] Raj VB, Singh H, Nimal AT, Tomer M, Sharma MU, Gupta V. Sens Actuat B 2015;207:375–82.
[185] Penza M, Aversa P, Cassano G, Wlodarski W, Kalantar-Zadeh K. Sens Actuat B 2007;127:168–78.
[186] Kalantar-Zadeh K, Trinchi A, Wlodarski Q, Holland A. Sens Actuat A 2002;100:135–43.
[187] Youssef IB, Alem H, Sarry F, Elmazria O, Rioboo RJ, Arnal-Herault C, et al. Sens Actuat B 2013;185:309–20.
[188] Zhou FM, Li Z, Fan L, Zhang SY, Shui XJ. Ultrasonics 2010;50:411–5.
[189] Powell DA, Klantar-Zageh K, Wlodarski W. Sens Actuat A 2004;115:456–61.
[190] Jian SJ, Chu SY, Huang TY, Water W. J Vac Sci Technol A 2004;22:2424–30.
[191] Chang RC, Chu SY, Hong CS, Chuang YT. Thin Solid Films 2006;498:146–51.
[192] Kalantar-Zadeh K, Pawell DA, Wlodarski W, Ippolito S, Galatis K. Sens Actuat B 2003;91:303–8.
[193] Dutheil P, Orlianges JC, Crunteanu A, Catherinot A, Champeaux C. Phys Staus Solid A 2015;212:817–25.
[194] Hong HS, Chung GS. Sens Actuat B 2010;148:347–52.
[195] Shih WS, Su HY, Wu MS. Thin Solid Films 2009;517:3378–81.
[196] Lin CM, Chen YY, Felmetsger VV, Lien WC, Riekkinen T, Sensesky DG, et al. J Micromcech Microeng 2013;23:025019.
[197] Hakiki ME, Elmazria O, Alnot P. IEEE Trans Ultrason Ferroelect Freq Control 2007;54:676–81.
[198] Matsukura F, Kakio S. Jap J Appl Phys 2014;53(07K):D04.
[199] Brizoual LL, Elmazria O, Zhgoon S, Sousson A, Sarry F, Djouadi MA. IEEE Trans Ultrason Ferroelect Freq Control 2010;57:1818–2010.
[200] Li R, Reyes PI, Ragavendiran S, Shen H, Lu Y. Appl Phys Lett 2015;107:073504.
[201] Lin CM, Yen TT, Felmetsger VV, Hopcroft MA, Kuypers JH, Pisano AP. Appl Phys Lett 2010;97:083501.
[202] Zou J, Lin CM, Chen YY, Pisano AP. J Appl Phys 2014;115:094510.
[203] Weinberg MS, Cunningham BT, Clapp CW. J MEMS 2000;9:370–9.
[204] Laurent T, Bastien FO, Pommier JC, Cachard A, Remiens D, Cattan E. Sens Actuat A 2000;87:26–37.
[205] Yantchev V. IEEE Trans Ultrason Ferroelect Freq Control 2010;57:801–7.
[206] Wingqvist G, Arapan L, Yantchev V, Katardiev I. J Micromech Microeng 2009;19:035018.
[207] Lin CM, Yen TT, Felmestger VV, Hopcroft MA, Kuypers JH, Pisano AP. Appl Phys Lett 2011;99:143501.
[208] Jia H, Duhamel R, Manceau JF, de Labachelerie M, Bastien F. Sens Acutat A 2005;121:321–6.
[209] Chen X, Liu D. Sens Acutuat A 2009;156:317–22.
[210] Chen X, Liu D, Chen J, Wang G. Smart Mater Struct 2009;18:115021.
[211] Krishnamoorthy S, Iliadis AA. Sold Stat Electro 2006;50:1113–8.
[212] Horrillo MC, Fernandez MJ, Fontecha JL, Sayago I, Garcia M, Aleixandre M, et al. Sens Actuat B 2006;188:356–61.
[213] Su J, Kuang ZB, Liu H. J Sound Vib 2005;286:981–99.
[214] Iqbal A, Walker G, Lacopi A, Mohd-Yasin F. J Cryst Growth 2016;440:76–80.
[215] Legrani O, Elmazria O, Zhgoon S, Pigeat P, Bartasyte A. IEEE Sens J 2013;13:487–91.
[216] Qian L, Li C, Li M, Wang F, Yang B. Appl Phys Lett 2014;105:183501.
[217] Chiang YF, Sung CC, Ro R. Appl Phys Lett 2010;96:154104.
[218] Zuerbig V, Hees J, Pletschen W, Sah RE, Wolfer M, Kirste L, et al. Thin Solid Films 2014;558:267–71.
[219] Salut R et al. Microelectr Eng 2013;112:133–8.
[220] Dow ABA, Ahmed A, Popov C, Schmid U, Kherani NP. Micro Nano Lett 2012;7:1030–2.
[221] Shikata S, Fujii, Sharda T. Diam Relat Mater 2009;18:253–7.
[222] Chung GS, Phan DT. J Korean Phys Soc 2010;57:446–50.
[223] Zaitsev BD, Kuznestsova IE, Joshi SG. J Appl Phys 2001;90:3648–9.
[224] Glushkov E, Glushkova N, Zhang C. J Appl Phys 2012;112:064911.
[225] Pensala T, Ylilammi M. IEEE Trans Ultrason Ferroelect Freq Control 2009;56:1731–44.
[226] Kumar P, Tripathi CC. Radioengineering 2013;22:687–93.
[227] Caeyssens F, Freeman CL, Allan NL, Sun Y, Ashfold MNR, Harding JH. J Mater Chem 2005;15:139–48.
[228] Cheng HE, Lin TC, Chen WC. Thin Solid Films 2003;425:85.
[229] Wu MS, Shih WC, Tsai WH. J Phys D 1998;31:943–50.
[230] Hachigo A, Nakahata H, Higaki K, Fujii S, Shikata S. Appl Phys Lett 1994;65:2556–8.
[231] Sundaram KB, Khan A. Thin Solid Films 1997;295:87–91.
[232] Atanas JP, Asmar RA, Khoury A, Foucaran A. Sens Acutat A 2006;127:49–55.
[233] Narayan J, Dovidenko K, Sharma AK, Oktyabrsky S. J Appl Phys 1998;84:2597–601.
[234] Szekeres A, Fogarassy Z, Petrik P, Vlaikova E, Cziraki A, Socol G, et al. Appl Surf Sci 2011;257:5370–4.
[235] Wang W, Liu Z, Yang W, Lin Y, Zhou SZ, Qian HR, et al. Mater Lett 2014;129:39–42.
[236] Liu JM, Chong N, Chan HLW, Wong KH, Choy CL. Appl Phys A 2003;76:93–6.
[237] Hullavarad SS, Vispute RD, Nagaraj B, Kulkarni VN, Dhar S, Venkatesan T, et al. J Electron Mater 2006;35:777–94.

[238] Liu ZF, Shan FK, Li YX, Shin BC, Yu YS. J Cryst Growth 2003;259:130–6.
[239] Banerjee AN, Ghosh CK, Chattopadhyay KK, Minoura H, Sarkar AK, Akiba A, et al. Thin Solid Films 2006;496:112–6.
[240] Matsumura M, Camata RP. Thin Solid Films 2005;476:317–21.
[241] Heitsch S, Bundesmann C, Wagner G, Zimmermann G, Rahm A, Hochmuth H, et al. Thin Solid Films 2006:496234–9.
[242] Chrisey DB, Hubler GK. Pulsed laser deposition of thin films. New York: Wiley; 1994.
[243] Wang YG, Lau SP, Lee HW, Yu SF, Tay BK, Zhang XH, et al. J Appl Phys 2003;94:1597.
[244] Goldsmith S. Surf Coat Technol 2006;201:3993–9.
[245] Yang RY, Weng MH, Pan CT, Hsiung CM, Huang CC. Appl Surf Sci 2011;257:7119–22.
[246] Li C, Li XC, Yan PX, Chong EM, Liu Y, Yue GH, et al. Appl Surf Sci 2007;253:4000–5.
[247] Xu XL, Lau SP, Chen JS, Chen GY, Tay BK. J Cryst Growth 2001;223:201.
[248] Znaidi L. Mater Sci Eng B 2010;174:18–30.
[249] Shinagawa T, Otomo S, Katayama J, Izaki M. Electrochim Acta 2007;53:1170–4.
[250] Kamalasanan MN, Chandra S. Thin Solid Films 1996;288:112–5.
[251] Hu TL, Mao SW, Cha CP, Wu P, Huang HL, Gan D. J Electron Mater 2007;36:81.
[252] Look DC, Reynolds DC, Litton CW, Jones RL, Eason DB, Cantwell G. Appl Phys Lett 2002;81:1830.
[253] Kipshidze G, Nikishin S, Kuryatkov V, Choi K, Gherasoiu I, Prokofyeva T, et al. J Electron Mater 2001;30:825–8.
[254] Chen Y, Bagnall DM, Koh H, Park K, Hiraga K, Zhu Z, et al. J Appl Phys 1998;84:3912.
[255] Nakamura K, Shoji T, Kang HB. Jpn J Appl Phys 2000;6:L534–6.
[256] Kim YH, Lee JH, Noh YK, Oh JE, Ahn SJ. Thin Sold Films 2015;576:61–7.
[257] Smith TP, Mecouch WJ, Miraglia PQ, Roskowski AM, Hartlieb PJ, Davis RF. J Cryst Growth 2003;257:255–62.
[258] Xi YA, Chen KX, Mont F, Kim JK, Schubert EF, Wetzel C, et al. J Electron Mater 2007;36:533–7.
[259] Minami T, Sonohara H, Takata S, Sato H. Jpn J Appl Phys B 1994;5:L743–6.
[260] Huber F, Madel M, Reiser A, Bauer S, Thonke K. J Cryst Growth 2016;445:58–62.
[261] Meng G, Liu X, Xie S, Peng D. J Cryst Growth 1996;163:232–7.
[262] Soh J, Jang S, Jeong I, Lee W. Thin Solid Films 1996;279:17–22.
[263] Stauden T, Eichhorn G, Cimalla V, Pezoldt J, Ecke G. Diamond Relat Mater 1996;5:1210–3.
[264] Ecke G, Eichhorn G, Pezoldt J, Reinhold C, Stauden T. Surf Coat Technol 1998;98:1503–9.
[265] Gorla CR, Emanetoglu NW, Liang S, Mayo WE, Lu Y, Wraback M, et al. J Appl Phys 1999;85:2595–602.
[266] Zhang BP, Wakatsuki K, Binh NT, Usami N, Segawa Y. Thin Solid Films 2004;449:12–9.
[267] Park WI, An SJ, Yi GC, Jang HM. J Mater Res 2001;16:1358–63.
[268] Huang J, Lu H, Ye Z, Wang L, Zhao B, He H. J Appl Phys 2007;102:053521.
[269] Lukasiewicz MI, Wojcik-Glodowska A, Guziewicz E, Wolska A, Klepka MT, Dluzewski P, et al. Semicond Sci Technol 2012;27:074009.
[270] Hoon JW, Chan KY, Krishnasamy J, Tou TY, Knipp D. Appl Surf Sci 2011;257:2508–15.
[271] Vashaei Z, Aikawa T, Ohtsuka M, Kobatake H, Fukuyama H, Ikeda S, et al. J Cryst Growth 2009;311:459–62.
[272] Nsimama PD, Niklasson GA, Samiji ME, Mbise GW, Wennerberg J. Vacuum 2012;86:1939–44.
[273] Feng B, Dong SR, Jin H, Zhou J, Yang Y, Ren TL, et al. Mater Lett 2012;79:25–8.
[274] Kelly PJ, Bradley JW. J Optoelectro Adv Mater 2009;11:1101–7.
[275] Martin F, Jan ME, Belgacem B, Dubois MA, Muralt P. Thin Solid Films 2006;514:341.
[276] Lin JL, Sproul WD, Moore JJ, Wu Z, Lee S, Chistyakov R, et al. JOM 2011;63:48–58.
[277] Kouznetsov V, Macák K, Schneider JM, Helmersson U, Petrov I. Surf Coat Technol 1999;122:290–3.
[278] Lin L, Moore JJ, Mishra B, Pinkas M, Sproul WD. Surf Coat Technol 2009;204:936–40.
[279] Barshilia HC, Deepthi B, Rajam KS. Thin Solid films 2008;516:4168–74.
[280] Duquenne C, Tessier PY, Besland MP, Angleraud B, Jouan PY, Aubry R, et al. J Appl Phys 2008;104:063301.
[281] Ke GS, Tao Y, Lu YS, Bian YB, Zhu T, Guo HB, et al. Alloy Comp 2015;646:446–53.
[282] Musil J. Vacuum 1986;36:161–9.
[283] Charker M, Moisan M, Zakrzewski Z. Plasma Chem Plasma Process 1986;6:79–96.
[284] Moisam M, Pelletier J. Microwave excited plasmas. 1st ed. New York: Elsevier Science Publisher; 1992. p. 11–52.
[285] Ehiasarian AP, New R, Munz WD, Hultman L, Helmersson U, Kouznetsov V. Vacuum 2002;65:147–54.
[286] Ehiasarian AP, Wen JG, Petrov I. J Appl Phys 2007;101:054301.
[287] Sittinger V, Ruske F, Werner W, Jacobs C, Szyszka B, Christie DJ. Thin Solid Films 2008;516:5847–59.
[288] Konstantinidis S, Hemberg A, Dauchot JP, Hecq M. J Vacuum Sci Technol B 2007:L19–21.
[289] Chang C, Yang Y, Lee J, Lou B. Thin Solid Films 2014;572:161–8.
[290] Flewitt AJ, Dutson JD, Beecher P, Paul D, Wakeham SJ, Vickers ME, et al. Semicond Sci Technol 2009;24:085002.
[291] Garcia-Gancedo L, Pedros JP, Zhu Z, Flewitt AJ, Milne WI, Luo JK, et al. J Appl Phys 2012;112:014907.
[292] Flewitt AJ, Luo JK, Fu YQ, Garcia-Gancedo L, Du XY, Lu J, et al. J Non-Newtonian Fluid Mech 2015;222:209–16.
[293] Li FM, Waddingham R, Milne WI, Flewitt AJ, Speakman S, Dutson J, et al. Thin Solid Films 2011;520:1278.
[294] García-Gancedo L, Ashley GM, Zhao XB, Pedrós J, Flewitt AJ, Milne WI, et al. Int J Nanomanufact 2011;7:371–82.
[295] Zhu H, Hupkes J, Bunte E, Huang SM. Surf Coat Technol 2010;205:773–9.
[296] Kluth O, Schöpe G, Hüpkes J, Agashe C, Müller J, Rech B. Thin Solid Films 2003;442:80–5.
[297] Wang Q, Ba DC, Zhang YC, Jiang RH. Mater Lett 2012;68:320–3.
[298] Prepelita P, Medianu R, Sbarcea B, Garoi F, Filipescu F. Appl Surf Sci 2010;256:1807–11.
[299] Lee JB, Lee MH, Park CK, Park JK. Thin Solid Films 2004;447–448:296–301.
[300] Tvarozek V, Novotny I, Sutta P, Flickyngerova S, Schtereva K, Vavrinsky E. Thin Solid Films 2007;515:8756–60.
[301] Singh AV, Chandra S, Bose G. Thin Solid Films 2011;519:5846–53.
[302] Kumada T, Ohtsuka M, Fukuyama H. AIP Adv 2015;5:017136.
[303] Gao YQ, Ma JH, Haung ZM, Wu J, Chu JH. Appl Phys A 2010;98:129–34.
[304] Jin H, Feng B, Dong SR, Zhou CJ, Zhou J, Yang Y, et al. J Electron Mater 2012;41:1948–54.
[305] Kao KS, Cheng CC, Chen YC. IEEE Trans Ultrason Ferroelect Freq Control 2002;49:345–9.
[306] Artieda A, Barbieri M, Sandu CS, Muralt P. J Appl Phys 2009;105:0245042.
[307] Iriarte GF, Rodriguez JG, Calle F. Mater Res Bull 2010;45:1039.
[308] Liu WJ, Wu SJ, Chen CM, Lai YC, Chuang CH. J Cryst Growth 2005;276:525.
[309] Zhu S, Su C, Lehoczky SL, Peters P, George MA. J Cryst Growth 2000;211:106–10.
[310] Sayago I, Aleixandrew M, Ares L, Fernansez MJ, Santos JP, Gutierrez J, et al. Appl Surf Sci 2005;245:273–80.
[311] Chu SY, Water W, Liaw JT. J Eur Ceram Soc 2003;23:1593–8.
[312] Severin D, Kappertz O, Nyberg T, Berg S, Wuttig M. Thin Solid Films 2007;515:354–3558.
[313] Arakelova E, Khachatryan A, Kteyan A, Ayjyan K, Grigoryan S. Thin Solid Films 2016;612:407–13.
[314] Auger MA, Vazquez L, Sanchez O, et al. J Appl Phys 2005;97:123528.
[315] Cherng JS, Chang DS. Thin Solid Films 2008;516:5293–5.
[316] Cherng JS, Lin CM, Chen TY. Surf Coat Technol 2008;202:5684–7.

[317] Cherng JS, Chen TY, Lin CM. Ferroelectric 2009;380:89–96.
[318] Vergara L, Clement M, Iborra E, Sanz-Hervás A, García López J, Morilla Y, et al. Diam Relat Mater 2004;13:839–42.
[319] Akiyama MT, Kano Kamohara K, et al. Appl Phys Lett 2008;93:021903.
[320] Xu T, Wu G, Zhang G, Yao Y. Sens Actuat A 2003;104:61–7.
[321] Kenanakis G, Stratakis E, Vlachou K, Vernardou D, Koudoumas E, Natsarakis N. Appl Surf Sci 2008;254:5695–9.
[322] Jasinki J, Liliental-Weber Z, Paduano QS, Weyburne DW. Appl Phys Lett 2003;83:2811.
[323] Sheng TY, Yu ZQ, Collins GJ. Appl Phys Lett 1988;52:576.
[324] Tan SS, Ye M, Milnes AG. Solid Stat Electro 1995;38:17–24.
[325] Min SR, Cho HN, Li YL, Chung CW. Thin Solid Films 2008;516:3521–9.
[326] Esmeryan KD, McHale G, Trabi CL, et al. J Phys D 2013;46:345307.
[327] Andreeva N, Ishizaki T, Baroch P, et al. Sens Actuat B 2012;164:15–21.
[328] Roach P, Shirtcliffe N, Newton MI. Soft Matter 2008;4:224–40.
[329] Lee M, Lee S, Yim C, et al. Sens Actuat B 2015;220:799–804.
[330] Sun RD, Nakajima A, Fujishima A, Watanabe T, Hashimoto K. J Phys Chem B 2001;105:1984–90.
[331] Liu H, Feng L, Zhai J, Jiang L, Zhu DB. Langmiur 2004;20:5659–61.
[332] Corso CD, Dickherber A, Hunt WD. Biosens Bioelectron 2008;24:805–11.
[333] Krishnamoorthy S, Bei T, Zoumakis E, Chrousos GP, Iliadis AA. Biosens Bioelectron 2006;22:707–14.
[334] Cao T, Wang AF, Liang XM, Tang HY, Auner GW, Salley SO, et al. Colloids Surf B 2008;63:176–82.
[335] Chiu CS, Lee HM, Kuo CT, Gwo S. Appl Phys Lett 2008;93:163106.
[336] Chan E, Jackson N, Mathewson A, Galvin P, Dow ABA, Kherani NP, et al. Appl Surf Sci 2013;282:709–13.
[337] Sanz-Hervás A, Clement M, Iborra E, Vergara L, Olivares J, Sangrador J. Appl Phys Lett 2006;88:161915.
[338] Clement M, Olivares J, Capilla J, Sangrador J, Iborra E. IEEE Trans Ultrason Ferroelect Freq Control 2012;59:128–34.
[339] Rambu AD, Iftimie N, Rusu GI. Mater Sci Eng B 2012;177:157–63.
[340] Gardeniers JG, Rittersma ZM, Burger GJm. J Appl Phys 1998;83:7844–54.
[341] Özgür U, Alivov YI, Liu C, Teke A, Reshchikov MA, Doğan S, et al. J Appl Phys 2005;98:041301.
[342] Clement M, Iborra E, Sangrador J, Sanz-Hervás A, Vergara L, Aguilar M. J Appl Phys 2003;94:1495–500.
[343] Fujimura N, Nishihara T, Goto S, Xu JF. ITO T J Cryst Growth 1993;130:269.
[344] Koch MH, Hartmann AJ, Lamb RN, Neuber N, Grunze M. J Phys Chem B 1997;101:8231–6.
[345] Caliendo C, Imperatori P, Cianci E. Thin Solid Films 2003;441:32–7.
[346] Lee JB, Jung JP, Lee MH, Park JS. Thin Solid Film 2004;447–448:610–4.
[347] Cheng CC, Chen YC, Horng RC YC, Wang HJ, Chen WR, Lai EK. J Vac Sci Technol 1998;16:3335–40.
[348] Kao HL, Chen WC, Chien WC, Lin HF, Chen TC, Lin CY, et al. Jap J Appl Phys 2008;47:124–9.
[349] Xu J, Thakur JS, Hu G, Wang Q, Danylyuk Y, Ying H, et al. Appl Phys A 2006;83:411–5.
[350] Takagaki Y, Santos PV, Wiebicke E, Brandt O, Schönherr HP, Ploog KH. Appl Phys Lett 2002;81:2538–40.
[351] Lim WT, Son BK, Kang DH, Lee CH. Thin Solid Film 2001;382:56–60.
[352] Liu HF, Chua SJ, Hu GX, Gong H, Xiang N. J Appl Phys 2007;102:083529.
[353] Lee Y, Kim Y, Kim H. J Mater Res 1998;13:1260–5.
[354] Okano H, Takahashi Y, Tanaka T, Shibata K, Nakano S. Jpn J Appl Phys 1992;3:3446–51.
[355] Chou K, Liu G. J. Cryst Growth 2003;243:439–43.
[356] Naik RS, Reif R, Lutsky JJ, Sodini CG. J Electrochem Soc 1999;146:691.
[357] Yanagitani T, Tomohiro S, Nohara T, Matsukawa M, Watanabe Y, Otani T. Jap J Appl Phys 2004;43:3004.
[358] Kajikawa Y. J Cryst Growth 2006;289:387–94.
[359] Yoshino Y, Lnoue K, Takeuchi M, Makino T, Katayama Y, Hata T. Vacuum 2000;59:403–10.
[360] Kim EK, Lee TY, Hwang HS, Kim YS, Park Y, Song JT. Superlatt Microstr 2006;39:138–44.
[361] Matsuda T, Furuta M, Hiramatsu T, et al. J Cryst Growth 2008;310:31.
[362] Phan DT, Suhm HC, Chung GS. Microlectro Eng 2011;88:105–8.
[363] Shih WC, Su HY, Wu MS. Thin Solid Films 2009;517:3378–81.
[364] Shih WC, Huang RC. Vacuum 2008;83:675.
[365] Shih WC, Wang TL, Chu MH. Jap J Appl Phys 2010;49(07H):D19.
[366] Shih WC, Wang TL, Pen YK. Appl Surf Sci 2012;258:5424–8.
[367] Jung JP, Lee JB, Kim JS, Park JS. Thin Solid Films 2004;447–448:605–9.
[368] Riekkinen T, Nurmela A, Molarius J, Pensala T, Kostamo P, Ylilammi M, et al. Thin Solid Films 2009;517:6588–92.
[369] Triboulet R, Perriere J. Prog Cryst Growth Charact Mater 2003;47:65–138.
[370] Imura M, Nakajima K, Liao M, Koide Y, Amano H. J Cryst Growth 2010;312:368–72.
[371] Vogg G, Miskys CR, Garrido JA, et al. J Appl Phys 2004;96:895–902.
[372] Jo YD, Koo SM. Appl Surf Sci 2009;255:3480–4.
[373] Novák P, Utta P, Medlín R, Netrvalová M, Ríha J. Sensor Lett 2014;12:1760–4.
[374] Iborra E, Vergara L, Sangrador J, Clement M, Sanz-Hervás A, Olivares J. IEEE Trans Ultrason Ferroelect Freq Control 2007;54:2367–75.
[375] Wingquist G, Bjurstrom J, Liljeholm L, Yantchev V, Katardjiev I. Sens Actuat B 2007;123:466–73.
[376] Cao X, Jin F, Yang J. IEEE Trans Ultrason Ferroelect Freq Control 2012;59:2522–7.
[377] Jose F, Ramaseshan R, Sundari S, Tripura, et al. Appl Phys Lett 2012;101:254102.
[378] Kawamoto T, Yanagitani T, Matsukawa M, Watanabe Y. J Jap Appl Phys 2010;49(07H):D16.
[379] Chen J, Deng H, Ji H, Tian Y. J Vac Sci Technol A 2011;29:03A116.
[380] Kashiwaba Y, Abe T, Onodera S, Masuoka F, Nakagawa A, Endo H, et al. J Cryst Growth 2007;298:477–80.
[381] Abe T, Kashiwaba Y, Onodera S, Masuoka F, Nakagawa A, Endo H, et al. J Cryst Growth 2007;298:457–60.
[382] Yanagitani T, Matsukawa M, Watanabe Y, Otani T. J Cryst Growth 2005;276:424–30.
[383] Ro R, Lee R, Lin ZX, Sung CC, Chiang YF, Wu S. Thin Solid Films 2013;529:470–4.
[384] Cui J, Du J, Wang J, Yang JS. Philos Mag Lett 2014;94:447–54.
[385] Bjurström J, Wingqvist G, Katardjiev I. IEEE Trans Ultrason Ferroelect Freq Control 2006;53:2095–100.
[386] Xiong J, Gu HS, Wu W. J Elect Mater 2011;40:1578–83.
[387] Sharma G, Liljieholm L, Enlund J, Bjurstrom J, Katardjiev I, Hjort K. Sens Acutat A 2010;159:111–6.
[388] Anderas E, Katardjiev I, Yantchev VM. IEEE Sens J 2012;12:2653–4.
[389] DeMiguel-Ramos M, Mirea T, Clement M, Olivares J, Sangrador J, Iborra. Thin Solid Films 2015;590:219–23.
[390] Bjurstrom J, Rosen D, Katardjiev I, Yanchev VM, Petrov I. IEEE Trans Ultrason Ferroelect Freq Control 2004;51:1347–53.
[391] Rouvaern JM, Menhaj-Rivenq A, Logette P, Goutin P, Haine F. J Phys D 2000;33:1287–97.
[392] Jen CK. J Acoust Soc Am 1988;84:26–9.
[393] Qin L, Chen Q, Cheng H, Wang QM. IEEE Trans Ultras Ferroelect Freq Control 2010;57:1840–53.
[394] Chen QM, Wang QM. Appl Phys Lett 2005;86:022904.
[395] Chu J, Peng X, Sajjad M, Yang B, Feng PX. Thin Solid Films 2012;520:3493–8.

[396] Bensmaine S, Brizoual LL, Elmazria O, Fundenberger JJ, Belmahi M. Diam Relat Mater 2008;17:1420–3.
[397] LaForge JM, Taschuk MT, Brett MJ. Thin Solid Films 2011;519(3530):3537.
[398] Mukhtar S, Asadov A, Cao W. Thin Solid Films 2012;520:3453–7.
[399] Park YJ, Sobahan KMA, Nam HJ, Kim JJ, Hwangbo CK. J Korean Phys Soc 2010;57:1657–60.
[400] Lai YF, Huang JH, Chen YC, Liu CP, Yang YW. J Eur Ceram Soc 2013;33:1809–14.
[401] Chen LC, Tien CH, Xuguang L, Binghe X. J Nanomater 2012;2012:409123.
[402] Yanagitani T, Suzuki M. Scit Mater 2013;69:724–7.
[403] Kwan JK, Sit JC. Sens Actuat B 2013;181:715–9.
[404] Lee YE, Kim SG, Kim YJ. J Vac Sci Technol A 1997;15:1194–9.
[405] Robbie K, Sit JC, Brett MJ. J Vac Sci Technol B 1998;16:1115–22.
[406] He Y, Fu J, Zhao Y. Front Phys 2014;9:47–59.
[407] Robbie K, Brett MJ. J Vac Sci Technol 1997;15:1460.
[408] Barranco A, Borras A, Gonzalez-Elipe AR, Palmero A. Progr Mater Sci 2016;76:59–153.
[409] Toledano D, Galindo RE, Yuste M, Albella JM, Sánchez O. J Phys Appl Phys 2013;46:045306.
[410] Deniz D, Karabacak T, Harper JME. J Appl Phys 2008;103:083553.
[411] Sato Y, Yanagisawa K, Oka N, Nakamura S, Shigesato Y. J Vac Sci Technol A 2009;27:1166–71.
[412] Yanagitani T, Suzuki M. Script Mater 2013;69:724–7.
[413] Jang HW, Kang HC, Noh DY, Yi MS. J Appl Phys 2003;94:2957.
[414] Mukhtar S, Asadov A, Gao W. Thin Solid Films 2012;520:3453–7.
[415] Takayanagi S, Yanagitani T, Matsukawa M. Jap J Appl Phys 2012;51(07G):C08.
[416] Yanagitani T, Morisato N, Takayanagi S, Matsukawa M. Watanabe IEEE Trans Ultrason Ferroelect Freq Control 2011;58:1062–8.
[417] Zhang H. Ferroelectrics 2013;445:96–106.
[418] Zhang H, Kosinski J. IEEE Trans Ultrason Ferroelect Freq Control 2012;59:2831–6.
[419] Zhang H, Bao Y. IEEE Trans Ultrason Ferroelect Freq Control 2014;61:525–34.
[420] Mu X, Kropelnicki P, Wang Y, Randles AB, Chai KTC, Cai H, et al. Appl Phys Lett 2014;105:113507.
[421] Fardeheb-Mammeri A, Assouar MB, Elmazria O, Fundenberger JJ, Benyoucef B. Semicond Sci Technol 2008;23:095013.
[422] Flickyngerova S, Netrvalova M, Sutta P, Novotny I, Tvarozek V, Gaspierik P, et al. Thin Solid Films 2011;520:1233–7.
[423] Deniz D, Harper JME, Hoehn JW, Chen F. J Vac Sci Technol A 2007;25:1214.
[424] Yanagitani T, Kiuchi M. J Appl Phys 2007;102:044115.
[425] Yanagitani T, Kiuchi M. Surf Coat Technol 2011;206:816–9.
[426] Deng R, Muralt P, Gall D. J Vac Sci Technol A 2012:30051501.
[427] Wang JS, Lakin KM. Appl Phys Lett 1983;42:352.
[428] Link M, Schreiter M, Weber J, Primig R, Pitzer D, Gabl R. IEEE Trans Ultraon Ferroelect Freq Control 2006;53:492–6.
[429] Rughoobur G, DeMiguel-Ramos M, Mirea T, Clement M, Olivares J, Díaz-Durán B, et al. Appl Phys Lett 2016;108:034103.
[430] Janotti A, Van de Walle CG. Rep Prog Phys 2009;72:126501.
[431] Liu Y, Li Y, Zeng H. J Nanomater 2013;2013:196521.
[432] Vaezi M, Sadrnezhaad S. Mater Sci Eng A 2007;141:23–7.
[433] Xiu FX, Yang Z, Mandalapu LJ, Zhao DT, Liu JL. Appl Phys Lett 2005;87:152101.
[434] Nam SH, Cho SJ, Boo JH. Nanoscale Res Lett 2012;7:25.
[435] Jeong SH, Park BN, Boo JH. Thin Solid Films 2008;516:5586–9.
[436] Lee E, Zhang R, Yoon G. J Appl Phys 2011;110:074101.
[437] Zhou J, He XL, Wang WB, Zhu Q, Xuan WP, Jin H, et al. IEEE Electron Lett 2013;34:1319–21.
[438] Kim EK, Kim YS. Superlatt Microstruct 2007;42:343–7.
[439] Water W, Chu SY, Juang YD, Wu SJ. Mater Lett 2002;57:998–1003.
[440] Chen LX, Liu S, Li CM, Wang YC, Liu JT, Wei JJ. Int J Mineral Metall Mater 2015;22:1108–14.
[441] Wang XB, Li DM, Zeng F, Pan F. J Phys D: Appl Phys 2005;38:4104–8.
[442] Wang XB, Song C, Li DM, Geng KW, Zeng F, Pan F. Appl Surf Sci 2006;253:1639.
[443] Lee JB, Lee HJ, Seo SH, Park JS. Thin Solid Films 2001;398–399:641–6.
[444] Ong WL, Huang H, Xiao J, Zeng K, Ho GW. Nanoscale 2014;6:1680–90.
[445] Matsunami N, Itoh M, Kato M, Okayasu S, Sataka M, Kakiuchida H. Appl Surf Sci 2015;350:31–7.
[446] Luo J, Luo P, Xie M, Du K, Zhao BX, Pan F, et al. Biosens Bioelectron 2013;49:512–8.
[447] Luo JT, Fan P, Pan F, Zeng F, Zhang DP, Zheng ZH, et al. Phys Stat Solidi - R 2012;6:436–8.
[448] Luo JT, Pan F, Fan P, Zeng F, Zhang DP, Zheng ZH, et al. Appl Phys Lett 2012;101:172909.
[449] Luo JT, Zhu XY, Chen G, Zeng F, Pan F. Phys Stat Solidi (R) 2010;4:209–11.
[450] Emanetoglu NE, Muthukumar S, Wu P, Wittstruck R, Chen Y, Lu Y. IEEE Trans Ultrason Ferroelect Freq Control 2003;50:537–43.
[451] Yang YC, Song C, Wang XH, Zeng F, Pan F. Appl Phys Lett 2008;92:012907.
[452] Water W, Yang YS. Sens Actuat A 2006;127:360.
[453] Iqbal A, Mahmood A, Khan Ahmed TM. Prog Nat Sci-Mater 2013;23:64.
[454] Lin SS, Huang JL, Sajgalik P. Surf Coat Technol 2005;191:286.
[455] Akiyama M, Kamohara T, Kano K, Teshigahara A, Takeuchi Y, Kawahara N. Adv Mater 2009;21:593–7.
[456] Akiyama M, Umeda K, Honda A, Nagase T. Appl Phys Lett 2013;102:021911.
[457] Moreira M, Bjurström J, Katardjiev I, Yantchev V. Vacuum 2011;86:23–6.
[458] Akiyama M, Kano K, Teshigahara A. Appl Phys Lett 2009;95:162107.
[459] Yanagitani T, Suzuki M. Appl Phys Lett 2014;105:122907.
[460] Tasnadi F, Alling B, Hoglund C, Wingqvist G, Birch J, Hultman L, et al. Phys Rev Lett 2010;104:137601.
[461] Matloub R, Artieda A, Sandu C, Milyutin E, Muralt P. Appl Phys Lett 2011;99:092903.
[462] Matloub R, Hadad M, Mazzalai A, Chidambaram N, Moulard G, Sandu CS, et al. Appl Phys Lett 2013;102:152903.
[463] Zhang Q, Han T, Chen J, Wang W, Hashimoto K. Diam Relat Mater 2015;58:31–4.
[464] Wang WB, Mayrhofer PM, He XL, Gillinger M, Ye Z, Wang XZ, et al. Appl Phys Lett 2014;105:133502.
[465] Wingqvist G, Tasnadi F, Zukauskaite A, Birch J, Arwin H, Hultman L. Appl Phys Lett 2011;97:112902.
[466] Hashimoto K, Sato S, Teshigahara A, Nakamura T, Kano K. IEEE Trans Ultrason Ferroelect Freq Control 2013;60:637.
[467] Kochhar A, Yamamoto Y, Teshigahara A, Hashimoto K, Tanaka S, Esashi M. IEEE Trans Ultrason Ferroelect Freq Control 2016;63:953–60.
[468] Song JH, Huang JL, Lu HH, Sung JC. Thin Solid Films 2007;516:223–7.
[469] Liljeholm L, Junaid M, Kubart T, Birch J, Hultman L, Katardjiev I. Surf Coat Technol 2011;206:1033–6.
[470] Song JH, Huang JL, Omori T, Sung JC, Wu S, Lu HH, et al. Thin Solid Films 2012;520:2247–50.
[471] Žukauskaitė A, Tholander C, Palisaitis J, Persson POA, Darakchieva V, Sedrine NB, et al. J Phys D: Appl Phys 2012;45:422001.
[472] Mayrhofer PM, Riedl H, Euchner H, Stoger-Pollach M, Mayrhofer PH, Bittner A, et al. Acta Mater 2015;100:81–9.
[473] Luo JT, Fan B, Zeng F, Pan F. J Phys D: Appl Phys 2009;42:235406.
[474] Liu H, Zeng F, Tang G, Pan F. Appl Surf Sci 2013;270:225–30.

[475] Narang V, Korakakis D, Seehra MS. J Appl Phys 2014;116:213911.
[476] Yokoyama T, Iwazaki Y, Onda Y, Nishihara T, Sasajima Y, Ueda M. IEEE Trans Ultrason Ferroelect Freq Control 2014;61:1322–8.
[477] Iwazaki Y, Yokoyama T, Nishihara T, Ueda M. Appl Phys Exp 2015;8:061501.
[478] Yokoyama T, Iwazaki Y, Onda Y, Nishihara T, Sasajima Y, Ueda M. IEEE Trans Ultrason Ferroelect Freq Control 2015;62:1007–15.
[479] Nagakubo A, Arita M, Yokoyama T, Matsuda S, Udea M, Ogi H, et al. Appl Phys 2015;54(07H):D01.
[480] Wang ZG, Li J, Fu YQ. Appl Phys Exp 2014;7:111004.
[481] Auld BA. Acoustic fields and waves in solids, vol. II. New York: John Wiley & Sons; 1973. p. 319.
[482] Kaletta UC, Wenger C. Ultrasonics 2014;54:291–5.
[483] Armstrong GA, Crampm S. Electro Lett 1973;9:322–3.
[484] Takagaki Y, Santos PV, Wiebicke E, Bramdt O, Schonheer HP, Ploog KH. Appl Phys Lett 2000;81:14.
[485] Talbi A, Sarry F, Brizoual LL, Elmazria O, Alnot P. IEEE Trans Ultrason Ferroelect Freq Control 2004;51:1421.
[486] Caliendo C, Imperatori P, Cianci E. Thin Solid Films 2003;441:32–7.
[487] Yan Z, Zhu XY, Pang GKH. Appl Phys Lett 2007;90:143503.
[488] Nakahata H, Hacigo A, Higaki K, Fujii S, Shikata SI, Fujimori N. IEEE Trans Ultrason Ferroelect Freq Control 1995;42:362–75.
[489] El Hakiki M, Elmazria O, Alnot P. IEEE Trans Ultraon Ferroelect Freq Control 2007;54:676–81.
[490] Le Brizoual L, Elmazria O, Zhgoon S, Soussou A, Sarry F, Djouadi MA. IEEE Trans Ultrason Ferroelect Freq Control 2010;57:1818–24.
[491] Zhou C, Yang Y, Jin H, Feng B, Dong S, Luo J, et al. Thin Solid films 2013;548:425–8.
[492] Yan Z, Zhu XY, Pang GKH, Zhang T, Liu WL, Cheng JG, et al. Appl Surf Sci 2007;253:9372–80.
[493] Tay KW, Huang CL, Wu L. Jap J Appl Phys 2004;43:1122–6.
[494] Pham VS, Mai L, Yoon G. Jap J Appl Phys 2008;47:6383–5.
[495] Freund LB, Suresh S. Thin film materials: stress, defect formation and surface evolution. Cambridge, UK: Cambridge University Press; 2004, ISBN 9780521529778.
[496] Takali F, Njeh A, Fuess H, Chozlen MHB. Mech Res Commun 2011;38:186–91.
[497] Singh J, Ranwa S, Akhtar J, Kumar M. AIP Adv 2015;5:067140.
[498] Anton SR, Sodano HA. Smart Mater Struct 2007;16:R1–R21.
[499] Conchon E, Renault PO, Goudaeu P, Le Bourhis E, Sondergard E, Barthel E, et al. Thin Solid Films 2010;518:5237–41.
[500] Vergara L, Olivares J, Iborra E, Clement M, Sanz-Hervás A, Sangrador J. Thin Solid Films 2006;515:1814–8.
[501] Zhang R, Lee E, Yoon G. Electron Lett 2010;46. 605-U17.
[502] Huang B, He G, Yang H. J Optoelectron Adv Mater 2010;12:2369–72.
[503] Yuste M, Escobar GR, Caretti I, Torres R, Sanchez O. J Phys D: Appl Phys 2012;45:025303.
[504] Joshi S, Nayak MM, Rajanna K. Appl Surf Sci 2014;296:169–76.
[505] Prepelita P, Craciun V, Filipescu M, Garoi F. Thin Solid Films 2013;545:564–70.
[506] Wang ZW, Zang H, Ren LY. J Mater Sci-Mater Electron 2014;25:5422–7.
[507] Iborra E, Clement M, Sangrador J, Sanz-Hervás A, Vergara L, Aguilar M. IEEE Trans Ultrason Ferroelect Freq Control 2004;51:352–8.
[508] Sign F, Kulriya PK, Pivin JC. Solid Stat Commun 2010;150:1751–4.
[509] Liu HY, Tang GS, Zeng F, Pan F. J Cryst Growth 2013;363:80–5.
[510] Six S, Rauschenbach B. Thin Solid films 2002;415:285–9.
[511] Kallel T, Dammak M, Wang J, Jadwisienczak WM. Mater Sci Eng B 2014;817:46–52.
[512] Liu L, Liu B, Edger JH, Rajasingam S, Kuball M. J Appl Phys 2002;92:5183–8.
[513] Kaigawa K, Shibata T, Nakamura Y, Asai K, Tanaka M, Sakai H, et al. J Mater Sci 2001;36:4649–59.
[514] Hu WG, Liu XL, Miao CM, Wei HY, Kang TT, Zhang PF, et al. J Phys D: Appl Phys 2007;40:7462–6.
[515] Raghavan S, Redwing JM. J Appl Phys 2004;96:2995.
[516] Chilla E, Osetrov AV, Koch R. Acoustoelastic anomaly in stressed heterostructures. Phys Rev B 2001;63:113308.
[517] Yamagushi H, Kato K, Nakai Y, Chen KJ. Appl Phys Lett 2008;92:253501.
[518] Cimalla V, Foerster C, Will F, Tonisch K, Brueckner K, Stephan R, et al. Appl Phys Lett 2006;88:253501.
[519] Placidi M, Moreno JC, Godignin P, Mestres N, Frayssinet E, Semond F, et al. Sens Actuat 2009;A150:64–8.
[520] Naik RS, Lutsky J, Reif R, Sodini CG, Becker A, Fetter L, et al. IEEE Trans Ultrason Ferroelect Freq Control 2000;47:292–6.
[521] Lappalainen J, Franti J, Lantto V. J Appl Phys 1997;82:3469.
[522] Changji H, Daoyun Z, Zhenhui H, Wenchun F, Qi Z. Appl Surf Sci 2011;257:2801–5.
[523] Stoney GG. Proc R Soc Lond A 1909;82:172–5.
[524] Puchert MK, Timbrell PY, Lamb RN. J Vac Sci Technol 1996;A14:2220.
[525] Hiramatsu T, Furuta M, Furuta H, Matsuda T, Hirao T. J Jap Appl Phys 2007;46:3319–23.
[526] Zheng X, Li J, Zhou Y. Acta Mater 2004;52:3313–22.
[527] Ntagwirumugra E, Gryba T, Zhang VY, Dogheche E, Lefebvre JE. IEEE Trans Ultrason Ferroelect Freq Control 2007;54:2011–5.
[528] Akiyama M, Nagao K, Ueno N, Tateyama H, Yamada T. Vacuum 2004;74:699–703.
[529] Vorobiev A, Gevorgian S. IEEE Trans Ultrason Ferroelect Freq Control 2014;61:840–8.
[530] Soluch W, Brzozowski E. IEEE Trans Electron Dev 2014;61:3395–8.
[531] Clement M, Olivares J, Iborra E, González-Castilla S, Rimmer N, Rastogi A. Thin Solid Films 2009;517:4673–8.
[532] Clement M, Iborra E, Olivares J, Giraud S, Bila S, Rimmer N, et al. IEEE Trans Ultrason Ferroelect Freq Control 2010;57:518–23.
[533] Hirata S, Okamoto K, Inoue S, Kim TW, Ohta J, Fujioka H, et al. J Solid State Chem 2007;180:2335–9.
[534] Akiyama M, Ueno N, Tateyama H, Nagao K, Yamada T. J Mater Sci 2005;40:1159–62.
[535] Huang CL, Tay KW, Wu L. Solid State Electro 2005;49:219–25.
[536] Okamoto K, Inoue S, Nakano T, Kim TW, Oshima M, Fujioka H. Thin Solid Films 2008;516:4809–12.
[537] Lee SH, Yoon KH, Lee JK. J Appl Phys 2002;92:4062–9.
[538] Patru M, Isac L, Cunha L, Matins P, Lanceros-Mendez, Oncioiu G, et al. Appl Surf Sci 2015;354:267–78.
[539] Richter D, Sakharov S, Mayer E, Reindl L, Fritze H. Proc Eng 2011;25:168–71.
[540] Sanz-Hervas A, Vergara L, Olivares J, Iborra E, Morilla Y, Garcia-Lopez J, et al. Diam Relat Mater 2005;14:1198–202.
[541] Tran AT, Pandraud G, Tichelaar FD, Nguyen MD, Schellevis H, Sarro PM. Appl Phys Lett 2013;103:221909.
[542] Akiyama M, Kamohara T, Ueno N, Nonaka K, Kuwano N. Thin Solid Films 2007;515:4565–9.
[543] Doll JC, Petzold BC, Ninan B, Mullapudi R, Pruitt BL. J Micromech Microeng 2010;97:20.
[544] Chou CH, Lin YC, Huang JH, Tai NH, Lin IN. Integrat Ferro 2006;80:407–13.
[545] Park JS, Lee JB, Jung JP, Lee MH. Thin Solid Films 2004;447:610–4.
[546] Lee SH, Lee JK, Yoon KH. J Vac Sci Technol 2003;A21:1–5.
[547] Akiyama M, Kamohara T, Kuwano N. J Cryst Growth 2008;310:345–50.
[548] Li Q, Kim TW, Inoue S, Okamoto K, Fujioka H. Appl Phys Lett 2006;89:241905.
[549] Chen JK, He XL, Wang WB, Xuan WP, Zhou J, Wang XZ, et al. J Mater Chem C 2014;2:9109.
[550] Dragoman M, Muller A, Neculoiu D, Vasilache G, Konstantinidis G, Grenier K, et al. Appl Phys Lett 2006;89:143122.
[551] Garcia-Gancedo L, Pedros J, Iborra E, Clement M, Olivares J, Flewitt AJ, et al. Sens Actuat B 2011;160:1386–93.
[552] Esconjauregui S, Makaryan T, Mirea T, DeMiguel-Ramos M, Olivares J, Guo Y, et al. Appl Phys Lett 2015;107:133106.

[553] Lu F, Gu L, Meziani MJ, Wang X, Luo PG, Veca LM, et al. Adv Mater 2009;21:139–51.
[554] Muller A, Neculoiu D, Vasilache D, Konstantinidis G, Grenier K, Dubuc D, et al. Appl Phys Lett 2006;89:143122.
[555] Novoselov KS, Fal'ko VI, Colombo L, Gellert PR, Schwab MG, Kim K. Nature 2009;490:192–200.
[556] Geim AK, Novoselov KS. Nat Mater 2007;6:183–91.
[557] Yao Y, Xue Y. Sens Actuat 2016;B222:755–62.
[558] Mayorov AS, Hunter N, Muchenje W, Wood CD, Rosamond M, Linfield EH, et al. Appl Phys Lett 2014;104:083509.
[559] Roschchupkin D, Ortega L, Zizak I, Plotitcyna O, Matveev V, Kononenko O, et al. J Appl Phys 2015;118:104901.
[560] Mamishev AV, Sundara-Rajan K, Yang F, Du Y, Zahn M. Interdigital sensors and transducers. Proc IEEE 2004;92:808–45.
[561] Plessky V, Reindl L. Review on SAW RFID tags. IEEE Trans Ultrason Ferroelect Freq Control 2010;57:654–68.
[562] Morgans DP. Surface acoustic wave devices for signal processing. Elsevier; 1991. ISBN 0-444-88845-4.
[563] Feldmann M, Henaff J. Surface acoustic waves for signal processing. Artech House; 1989. ISBN 0-89006-308-7.
[564] Darmawan M, Byun D. Microfluid Nanofluid 2015;18:1107–14.
[565] Kwon JW, Yu H, Zou Q, Kim ES. J Micromech Microeng 2006;16:2697–704.
[566] Lee CY, Pang W, Yu H, Kim ES. Appl Phys Lett 2008;93:034104.
[567] Kwok KW, Hon SF, Lin D. Sens Actuat A 2011;168:168–71.
[568] Hon SF, Kwok KK, Li HL, Ng HY. Rev Sci Instrum 2010;81:065102.
[569] Zhu X, Kim ES. Sens Actuat A 1998;66:355–60.
[570] Yu H, Zu Q, Kwon JW, Huang D, Kim ES. Liquid needle. JMEMS 2007;16:445–53.
[571] Phan DT, Chung GS. Appl Surf Sci 2011;257:8696–701.
[572] Buyukkose S, Vratzov B, Atac D, van der Veen J, Santos PV, Va der Wiel WG. Nanotechnology 2012;23:315303.
[573] Buyukkose S, Vratzov B, Atac D, van der Veen J, Santos PV, Va der Wiel WG. Appl Phys Lett 2013;102:013112.
[574] Luo JK, Fu YQ, Li YF, Du XY, Flewitt AJ, Walton AJ, et al. J Micromech Microeng 2009;19:054001.
[575] Nakamura H, Yamada T, Ishizaki T, Nishimura K. IEEE Trans Ultrason Ferroelect Freq Control 2004;49:761.
[576] Lehtonen S, Plessky VP, Hartmann CS, Salomaa M. IEEE Trans Ultrason Ferroelect Freq Control 2004;51:1697.
[577] Lamothe M, Plessky V, Friedt JM, Ostertag T, Ballandras S. Electron Lett 2013;49:1576–7.
[578] Plessky V, Lamothe M. Electron Lett 2013;49:1503–4.
[579] Wu TT, Chang IH. J Appl Phys 2005;98:024903.
[580] Fu C, Lee K, Yang SS, Wang W. Sens Actuat A 2014;218:80–7.
[581] Wu TT, Tang HT, Chen YY, Lin PL. IEEE Trans Ultrason Ferroelect Freq Control 2005;52:1384–92.
[582] de Lima MM, Hey R, Seidel JW, Santos PV. J Appl Phys 2003;94:7848–55.
[583] Kumar P, Trripathi CC. Radioengng 2013;22:687–93.
[584] Chen YY, Lai YT, Hsu CH. J Jap Appl Phys 2014;53(07K):D01.
[585] Fernandez MJ, Fontecha JL, Sayago I, Aleixandre M, Lozano J, Gutierrez J, et al. Sens Actuat B 2007;127:277–83.
[586] Qiu X, Tang R, Chen SJ, Zhang H, Pang W, Yu H. Elelctrochem Commun 2011;13:488–90.
[587] Guo YJ, Zhang J, Zhao C, Hu PA, Zu XT, Fu YQ. Optik 2014;125:5800–3.
[588] Tang YL, Li ZJ, Ma JY, Guo YJ, Fu YQ, Zu XT. Sens Actuat B 2014;201:114–21.
[589] Guo YJ, Zhang J, Zhao C, Li YF, Placido F, Walton A, et al. Mater Res Bull 2013;48:5058–63.
[590] Pang HF, Fu YQ, Li ZJ, Li YF, Placido F, Walton A, et al. Sens Actuat A 2013;193:87–94.
[591] Wang WB, Gu H, He XL, Xuan WP, Chen JK, Wang XZ, et al. Chin Phys Lett B 2015;5:057701.
[592] Tigli O, Bivona L, Berg P, Zaghloul ME. IEEE Trans Biomed Circuits Syst 2010;4:62–73.
[593] Lee DS, Lee JH, Luo JK, Fu YQ, Milne WI, Maeng S, et al. J Nanosci Nanotechnol 2009;9:7181–5.
[594] Lee DS, Luo JK, Fu YQ, Milne WI, Milne WI, Park NM, et al. J Nanosci Nanotechnol 2008;8:4624.
[595] Chen YC, Chang WT, Cheng CC, Shen JY, Kao KS. Curr Appl Phys 2014;14:608–13.
[596] Yanagitani Y, Nohara T, Matsukawa M, Watanabe Y, Otani T. IEEE Trans Ultrason Ferroelect Freq Control 2005;52:2140–5.
[597] Jin F, Qian ZH, Wang ZK, Kishimoto K. Smart Mater Struct 2005;14:515–23.
[598] Mchale G, Newton MI, Martin F. J Appl Phys 2002;91:9701.
[599] Du J, Harding GL. Sens Actuat A 1998;65:152.
[600] Krishnamoorthy S, Ilias AA, Beic T, et al. Biosens Bioelectron 2008;24:313.
[601] Kim YW, Sardari SE, Meyer MT, Iliadis AA, Wu HC, Bentley WE, et al. Sens Actuat B 2012;163:136–45.
[602] Zhou J, He XL, Wang WB, Zhu Q, Xuan WP, Jin H, et al. IEEE Electron Lett 2013;34:1319.
[603] Wang WB, Gu H, He XL, Xuan WP, Chen JK, Wang XZ, et al. Appl Phys Lett 2014;104:212107.
[604] Wang WB, Gu H, He XL, Xuan WP, Chen JK, Wang XZ, et al. Chin Phys B 2015;24:057701.
[605] Chen JK, Guo HW, He XL, Wang WB, Xuan WP, Jin H, et al. J Microeng Micromech 2015;25:115005.
[606] Kao KS, Cheng CC, Chen YC, et al. Appl Surf Sci 2004;230:334.
[607] Kao KS, Cheng CC, Chen YC, Lee YH. Appl Phys A 2003;76:1125.
[608] Pyun JC, Beutel H, Meyer JU, Ruf HH. Biosens Bioelectron 1998;13:839–45.
[609] Lin CM, Lai YJ, Hsu JC, Chen YY, Senesky DG, Pisano AP. Appl Phys Lett 2011;99:143501.
[610] Pepper J, Noring R, Klepner M, Cunningham B, Petrovich A, Bousquet R, et al. Sens Actuat B 2003;96:565.
[611] Arapan L, Katardjiev I, Yantchev V. J Micromech Microeng 2012;22:085004.
[612] Katardjiev I, Yantchev V. Vacuum 2012;86:520–31.
[613] White RM. Faraday Discuss 1997;107:1–13.
[614] Huang IY, Lee MC. Sens Actuat B 2008;132:340.
[615] Yantchev V, Katardjiev I. J Micromech Microeng 2013;23:043001.
[616] Kropelnicki P, Muckensturm KM, Mu XJ, Randles AB, Cai H, Sng WC, et al. J Micromech Microeng 2013;23:085018.
[617] Bjurstrom J, Katardjiev L, Yantchev V. Appl Phys Lett 2005;86:154103.
[618] Mirea T, Yantchev V. Sens Actuat B 2015;208:212–9.
[619] Mirea T, Yantchev V, Olivares J, Iborra E. Sens Actuat B 2016;229:331–7.
[620] Talbi A, Soltani A, Mortet V, Gerbedoen JC, De Jaeger JC, Pernod P. Diam Relat Mater 2012;22:66–9.
[621] Kone I, Domingue F, Reinhardt A, Jacquinot H, Borel M, Gorisse M, et al. Appl Phys Lett 2010;96:223504.
[622] Pietrantonio FD, Benetti M, Cannata D, Beccherelli R, Verona E. IEEE Trans Ultrason Ferroelect Freq Control 2010;57:1175–82.
[623] Sun C, Soon BW, Zhu Y, Wang N, Loke SPH, Mu X, et al. Appl Phys Lett 2015;106:253502.
[624] He XL, Guo HW, Chen JK, Wang WB, Xuan WP, Xu Y, et al. Appl Phys Lett 2014;104:213504.
[625] He XL, Li DJ, Zhou J, Wang WB, Xuan WP, Dong SR, et al. J Mater Chem C 2013;1:6210–5.
[626] Choi HR, Eswaran SK, Cho YS. ACS Appl Mater Interf 2015;7:14654–9.
[627] Akin N, Cetin SS, Cakmak M. J Mater Sci-Mater El 2013;24:5091–6.
[628] Lim YS, Kim DW, Kang JH, Seo SG, Kim BB, Choi HS, et al. Microsc Microanal 2013;19:131–5.
[629] Sierros KA, Banerjee DA, Morris NJ, Cairns DR, Kortidis I, Kiriakidis G. Thin Solid Films 2010;519:325–30.
[630] Liu YY, Zang YL, Wei GX, Li J, Fan XL, Cheng CF. Mater Lett 2009;63:2597–9.
[631] Min HS, Yang MK, Lee JK. J Vac Sci Technol A 2009;27:352–5.

[632] Chen K, Chiang KS, Chan HP, Chu PL. Opt Mater 2008;30:1244–50.
[633] Choi YJ, Lee C. Trans Elect Electron Mater 2012;13:245–7.
[634] Akiyama M, Morofuji Y, Kamohara T, Nishibubo K, Tsubai M, Fukuda O, et al. J Appl Phys 2006;100:114318.
[635] Laurenti M, Stassi S, Lorenzoni M, Fontana M, Canavese G, Cauda V, et al. Nanotechnology 2015;16:215704.
[636] Zhou J, He XL, Jin H, Wang W, Feng B, Dong S, et al. J Appl Phys 2013;114:044502.
[637] Akiyama M, Morofuji Y, Kamohara T, Nishikubo K, Ooishi Y, Tsubai M, et al. Adv Funct Mater 2007;17:458–62.
[638] Akiyama M, Morofuji Y, Nishikubo K, Kamohara T. Appl Phys Lett 2008;92:043509.
[639] Jin H, Zhou J, Dong SR, Feng B, Luo JK, Milne WI, et al. Thin Solid Film 2012;520:4863–70.
[640] Smecca E, Maita F, Pellegrino G, Vinciguerra V, La Magna L, Mirabella S, et al. Appl Phys Lett 2015;106:232903.
[641] Li Q, Liu H, Li G, Zeng F, Pan F, Luo J, et al. J Electro Mater 2016;45:2702–9.
[642] Jackson N, Keeney L. Smart Mater Struct 2013;22:115033–41.
[643] Chen JK, Guo HW, He XL, Wang WB, Xuan WP, Jin H, et al. J Micromech Microeng 2015;25:115005.
[644] Liu Y, Li Y, El-Hady AM, Zhao C, Du JF, Liu Y, et al. Sens Actuat B 2015;221:230–5.
[645] Liu Y, Luo JT, Zhao C, Zhou J, Hassan S, Li Y, et al. IEEE Trans Electron Dev 2016;63:4535–41.
[646] Satoh Y, Nishihara T, Yokoyama T, Ueda M, Miyashita T. Jap J Appl Phys 2005;44:2883–94.
[647] Qiu X, Tang R, Chen SJ, Zhang H, Pang W, Yu H. Electrochem Commun 2011;13:488–90.
[648] Qiu X, Tang R, Zhu J, Oiler J, Yu C, Wang Z, et al. Sens Actuat B 2011;151:360–4.
[649] Kim E, Choi YK, Song J, Lee J. Mater Res Bull 2013;48:5076–9.
[650] Lin RC, Chen YC, Chang WT, Cheng CC, Kao KS. Sens Actuat A 2008;147:425–9.
[651] Wenzel SW, White RM. Appl Phys Lett 1989;54:1976.
[652] Lanz R, Muralt P. IEEE Trans Utralson Ferroelect Freq Control 2005;52:936.
[653] Clement M, Olivares J, Capilla J, Sangrador J, Iborra E. IEEE Trans Ultrason Ferroelect Freq Control 2012;59:128–34.
[654] Olivares J, Wegmann E, Capilla J, Iborra E, Clement M, Vergara L, et al. IEEE Trans Ultrason Ferroelect Freq Control 2010;57:23–9.
[655] Iborra E, Clement M, Capilla J, Olivares J, Felmetsger V. Thin Solid Films 2012;520:3060–3.
[656] Zhao XB, Ashley G, Garcia-Gancedo L, Jin H, Luo JK, Flewitt AJ, et al. Sens Actuat B 2012;163:242–6.
[657] García-Gancedo L, Al-Naimi F, Flewitt AJ, Milne WI, Ashley GM, Luo JK, et al. IEEE Trans Ultrason Ferroelect Freq Control 2011;58:2438–44.
[658] Wu MJ, Jin H, Dong SR, Jin PC, Luo JK, Milne WI. Electron Lett 2011;47:893–4.
[659] Collado C, Rocas E, Padilla A, Mateu J, O'Callaghan JM, Orloff ND, et al. IEEE Trans Microwave Theory Tech 2011;59:1206–13.
[660] Capilla J, Olivares J, Clement M, Sangrador J, Iborra E. IEEE Trans Ultrason Ferroelect Freq Control 2012;59:366–72.
[661] Ashley G, Kirby P, Butler T, Watermore R, Luo JK. J Electrochem Soc 2010;157:J419–24.
[662] Wingqvist G, Bjurstrom J, Liljeholm L, Yantchev V, Katardjiev I. Sens Actuat B: Chem 2007;123:466–73.
[663] Wingqvist G, Yantchev V, Katardjiev I. Sens Actuat A: Phys 2007;148:88–95.
[664] Gabl R, Feucht HD, Zeininger H, Eckstein G, Wersing W. Biosens Bioelectron 2004;19:615.
[665] Nirschl M, Bluher A, Erler C, Katzchner B, Vikholm-Lundin I, Auer S, et al. Sens Act A: Phys 2009;156:180–4.
[666] Yan Z, Song Z, Liu W, Ren HX, Gu N, Zhou XY, et al. Appl Surf Sci 2007;253:9372.
[667] Dong SR, Bian XL, Jin H, Hu NN, Zhou J, Wong H, et al. Appl Phys Lett 2013;103:062904.
[668] Zheng D, Guo P, Xiong J, Wang S. Nanoscale Res Lett 2016;11:396.
[669] Tadigadapa S, Mateti K. Meas Sci Technol 2009;20:092001.
[670] Lee TY, Song JT. Thin Solid Films 2010;518:6630–3.
[671] Zheng D, Xiong J, Guo P, Li YB, Wang SF, Gu HS. Mater Res Bull 2014;59:411–5.
[672] Wingqvist G. Surf Coat Technol 2010;205:1279–86.
[673] Chen Y, Reyes PI, Duan Z, Saraf G, Wittstruck R, Lu Y, et al. J Electron Mater 2009;38:1605–11.
[674] Milyutin E, Gentil S, Muralt P. J Appl Phys 2008;104:084508.
[675] Martin F, Jan EE, Rey-Mermet S, Belgacem B, Su D, Cantoni M, et al. IEEE Trans Ultrason Ferroelect Freq Control 2006;53:1339–43.
[676] Chung CJ, Chen YC, Cheng CC, Kao KS. IEEE Trans Ultrason Ferroelect Freq Control 2006;53:2095–100.
[677] Qin LF, Chen QM, Cheng HB, Qian C, Li JF, Wang QM. J Appl Phys 2011;110:094511.
[678] Link M, Webber J, Schreiter M, Wersing W, Elmazria O, Alnot P. Sens Actuat 2007;B121:372.
[679] Link M, Schreiter M, Weber J, Gabl R, Pitzer D, Primig R, et al. J Vac Sci Technol A 2006;24:218.
[680] Zheng D, Xiong J, Guo P, Wang SF, Gu HS. RSC Adv 2016;6:4908–13.
[681] Chen YC, Shih WC, Chang WT, Yang CH, Kao KS, Cheng CC. Nanoscale Res Lett 2015;10:69.
[682] Weber J, Albers WM, Tuppurainen J, Link M, Gabl R, Wersing W, et al. Sens Actuat A: Phys 2006;128:84–8.
[683] Chen D, Wang J, Li D, Xu Y, Li Z. Sens Actuat A 2011;165:379–84.
[684] Chung CJ, Chen YC, Cheng CC, Kao KS. IEEE Trans Ultrason Ferroelect Freq Control 2008;55:857–64.
[685] Corso CD, Dickherber A, Hunt WD. J Appl Phys 2007;101:054514.
[686] Chen D, Wang JJ, Xu Y, Li D. Sens Actuat B 2012;171–172:1081–6.
[687] Ho GK, Abdolv R, Sivapurapu A, Humad S, Ayazi F. J Microelectromech Syst 2008;17:512.
[688] Wathen AD, Munir F, Hunt WD. J Appl Phys 2010;108:114503.
[689] Chen D, Wang J, Xu Y, Li DS, Li Z, Song H. Appl Surf Sci 2010;256:7638–42.
[690] Chen D, Wang J, Xu Y, Li D, Zhang L, Liu W. J Micoreng Micromech 2013;23:095032.
[691] Voiculescu I, Nordin AN. Biosens Bioelectron 2012;33:1–9.
[692] Xu W, Appel J, Chae J. J MEMS 2012;21:302–7.
[693] Clement M, Olivares J, Capilla J, Sangrador J, Iborra E. IEEE Trans Ultrason Ferroelect Freq Control 2007;54:2367–75.
[694] Clement M, Iborra E, Olivares J, DeMiguel-Ramos M, Mirea T, Sangrador J. Ultrasonics 2014;54:1504–8.
[695] Xu W, Choi S, Chae J. Appl Phys Lett 2010;96:053703.
[696] Garcia-Gancedo L, Pedros J, Iborra E, Clement M, Zhao XB, Olivares J, et al. Sens Actuat B 2013;183:136–43.
[697] Zhou CJ, Shu Y, Yang Y, Jin H, Dong SR, Chan MS, et al. J Micromech Microeng 2015;25:055003.
[698] Kang YR, Kang SC, Paek KK, Kim YK, Kim SW, Ju BK. Sens Actuat A 2005;117:62–70.
[699] Petroni S, Tegola CL, Caretto G, Campa A, Passaseo A, Vittorio MD, et al. Microelectron Eng 2011;88:2372.
[700] Chen GH, Zhao XR, Wang XZ, Jin H, Li SJ, Dong SR, et al. Sci Rep 2015;5:9510.
[701] Zhou C, Shu Y, Yang Y, Jin H, Dong SR, Chan M, et al. J Micromech Microeng 2015;25:055003.
[702] Yu LY, Jin H, Hu NN, Dong SR, Luo JK. Integrat Ferroelect 2016;168:157–62.
[703] He XL, Garcia-Gancedo L, Jin PC, Zhou J, Wang WB, Dong SR, et al. J Micromech Microeng 2012;22:125005.
[704] Zhoul L, Wu Y, Xuan M, Manceau JF, Bastien F. Sensors 2012;12:10369–80.
[705] Wang T, Mu X, Kropelnicki P, Randles AB, Lee C. J Micromech Microeng 2014;24:075002.
[706] Seidel W, Hesjedal T. Appl Phys Lett 2004;84:1407–9.
[707] Zhang X, Xu W, Chae J. Sens Actuat A 2011;166:264–8.
[708] Wathen AD, Munir F, Hunt WD. Appl Phys Lett 2009;95:123509.
[709] Garcia-Gancedo L, Pedros J, Zhao XB, Ashley GM, Flewitt AJ, Milne WI, et al. Biosens Bioelectron 2012;38:369–74.
[710] Shilton R, Tan MK, Yeo LY, Friend JR. J Appl Phys 2008;104:014910.

[711] Pearton SJ, Norton DP, Ip K, Heo YW, Steiner T. Progr Mater Sci 2005;50:293–340.
[712] Water W, Chu SY. Mater Lett 2002;55:67–72.
[713] Kim HW, Kim NH. Phys Stat Solid A 2004;201:235–8.
[714] Fu YQ, Garcia-Gancedo L, Pang HF, Porro S, Gu YW, Luo JK, et al. Biomicrofluidics 2012;6:024105.
[715] Zhou J, DeMiguel-Ramos M, Garcia-Gancedo L, Iborra E, Olivares J, Jin H, et al. Sens Actuat B 2014;202:984–92.
[716] Zhou J, Pang HF, Garcia-Gancedo L, Iborra E, Clement M, De Miguel-Ramos M, et al. Microfluid Nanofluid 2015;18:537–48.
[717] Zhou J, De Miguel-Ramos M, Garcia-Gancedo L, Iborra E, Olivares J, Jin H, et al. Sens Actuat B 2014;202:984.
[718] Wang WB, Fu YQ, Chen JJ, Xuan WP, Chen JK, Mayrhofer P, et al. J Microeng Micromech 2016;26:075006.
[719] Wang WB, He XL, Zhou J, Gu H, Xuan WP, Chen JK, et al. J Electrochem Soc 2014;161:B230–6.
[720] Guo YJ, Dennison AP, Li Y, Luo JK, Zu XT, Mackay CL, et al. Microfluid Nanofluid 2015;19:273.
[721] Fu YQ, Li Y, Zhao C, Placido F, Walton AJ. Appl Phys Lett 2012;101:194101.
[722] Nguyen NT, White RT. Sens Actuat 1999;77:229.
[723] Meng AH, Nguyen NT, White RM. Biomed Microdev 2002;2:169.
[724] Ogawa J, Kanno I, Kotera H, Wasa K, Suzuki T. Sens Actuat A 2009;52:211.
[725] Luo JK, He XL, Zhou J, Wang WB, Xuan WP, Chen JK, et al. Proc Eng 2015;120:717–20.
[726] Shilton RJ, Mattoli V, Travagliati M, Agostini M, Desii A, Beltram F, et al. Adv Funct Mater 2015;25:5895–901.
[727] Kondoh J, Shimizu N, Matsui Y, Shiokawa S. IEEE Trans Ultrason Ferroelect Freq Control 2005;52:1881.
[728] Kryshta RG, Kundin AP, Medved AV, Shemet VV. Tech Phys Lett 2002;28:50.
[729] Guttenberg Z, Muller H, Habermuller H, Geisbauer A, Pipper J, Felbel J, et al. Lab Chip 2005;5:308.
[730] Singh D, Narasimulu AA, Garcia-Gancedo L, Fu YQ, Hasan T, Lin SS, et al. Nanotechnology 2013;24:275601.
[731] Wang SY, Li ZJ, Zhou XS, Zhao C, Zu XT, Fu YQ. Nanosci Nanotechnol Lett 2015;7:169–92.
[732] Singh D, Narasimulu AA, Garcia-Gancedo L, Fu YQ, Hasan T, Lin SS, et al. Mater Chem C 2013;1:2525–8.
[733] Homola J, Yee SS, Gauglitz G. Sens Actuat B 1999;54:3–15.
[734] Renaudin A, Chabot V, Grondin E, Aimez V, Charette PG. Lab Chip 2010;10:111–5.
[735] Puiu M, Gurban AM, Rotariu L, Brajnicov S, Viespe C, Bala C. Sensors 2015;15:10511–25.
[736] Galopin E, Beaugeois M, Pinchemel B, Camart J, Bouazaoui M, Thomy V. Biosens Bioelectron 2007;23:746.
[737] Xie Y, Zhao Y, Li S, Rufo J, Yang S, Guo F, et al. Lab Chip 2013;13:1772–9.
[738] Wiklund N, Gunther C, Lemor R, Jager M, Fuhr G, Hertz HM. Lab Chip 2006;6:1537–44.
[739] Fatoyinbo HO, Hoettges KF, Reddy SM, Hughes MP. Biosens Bioelectron 2007;23:225–32.
[740] Ravula SK et al. Sens Actuat B 2008;130:645–52.
[741] Liu F, Li F, Nordin AN, Voiculescu I. Sensors 2013;13:3039–55.
[742] Sokolowski SS, Trudell DE, Byrness JE, Okandan M, Bauer JM, Manley RG, et al. Sens J 2006;6:784–95.
[743] Reboud J, Wilson R, Zhang Y, Ismail MH, Bourquin Y, Cooper JM. Lab Chip 2012;12:1268–73.
[744] Li Y, Fu YQ, Flynn BW, Parkes W, Liu Y, Brodie SD, et al. IEEE Trans Semicon Manuf 2012;25:323–30.
[745] Li Y, Fu YQ, Brodie S, Mansuor A, Walton AJ. Biomicrofluidics 2012;6:012812.
[746] Zhang M, Cui W, Chen X, Wang C, Pang W, Duan X, et al. J Micromech Microeng 2015;25:025002.
[747] Nawaz F, Jeoti V. Wireless Network 2014;20:2581–7.
[748] Friedt JM, Droit C, Martin G, Ballandras S. Rev Sci Instrum 2010;81:014701.
[749] Friedt JM, Droit C, Ballandras S, Alzuaga S, Martin GJ, Sandoz P. Rev Sci Instrum 2012;83:055001.
[750] Friedt JM, Rétornaz T, Alzuaga S, Baron T, Martin G, Laroche T, et al. J Appl Phys 2011;109:034905.
[751] Alghane M, Chen BX, Fu YQ, Li Y, Desmulliez MPY, Mohammed MI, et al. Phys Rev E 2012;86:056304.
[752] Alghane M, Fu YQ, Chen BX, Li Y, Desmulliez MPY, Walton AJ. J Appl Phys 2011;109:114901.
[753] Alghane M, Fu YQ, Chen BX, Li Y, Walton AJ. Microfluid Nanofluid 2012;13(6):919–27.
[754] Alghane M, Fu YQ, Chen BX, Li Y, Desmulliez MPY, Walton AJ. J Appl Phys 2012;112(8):084902.
[755] Zhang A, Liu W, Zhang Y. Surf Sci 2015;642:45–50.
[756] Blonsky MN, Zhuang HL, Sigh AK, Hennig RG. ACS Nano 2015;9:9885–91.